INSTITUTO SUPERIOR DE ENGENHARIA DO PORTO

MESTRADO EM ENGENHARIA MECÂNICA




Uma análise de otimização estrutural do sistema de suporte de rodas de um veículo espacial utilizando técnicas avançadas de discretização sem malha

RUI PEDRO NUNES MONTEIRO
outubro de 2025

POLITÉCNICO
DO PORTO

ISEP INSTITUTO SUPERIOR DE ENGENHARIA DO PORTO

A structural optimization analysis of the wheel supporting system of a space Rover using advanced discretization meshless techniques

Rui Pedro Nunes Monteiro

Dissertação de Mestrado em Engenharia Mecânica

Área de Especialização em

Construções Mecânicas

Orientador: Professor Doutor Jorge Américo de Oliveira Pinto Belinha

Coorientador: Professor Doutor Daniel Espírito Santo Rodrigues

Júri:

Presidente: Professora Doutora Elza Maria Morais Fonseca, ISEP

Arguente: Professor Doutor Sérgio Manuel Oliveira Tavares, UA

Orientador: Professor Doutor Jorge Américo de Oliveira Pinto Belinha, ISEP

Porto, outubro 2025

Abstract

Space exploration has consistently been a stimulator for technological advancements, driving innovations in various engineering fields and pushing the boundaries of what is possible in extreme environments. In particular, the optimization of rover components for extraterrestrial missions has become a critical area of focus, as these devices must combine lightweight designs, high durability, and adaptability to harsh and unpredictable conditions found on celestial bodies such as the Moon and Mars. This work explores the potential of advanced numerical methods, specifically the Radial Point Interpolation Method (RPIM) and the Natural Neighbour Radial Point Interpolation Method (NNRPIM), for structural analysis and design optimization when paired with Bio-Inspired Remodelling Algorithm (BIRA). These meshless methods present significant advantages over traditional Finite Element Methods (FEM), including the ability to handle large deformations and complex geometries without mesh distortions. This thesis culminates in the analysis of the Perseverance rover's component that connects the wheel with the suspension. As a result, this work proposes six optimized models that present stiffness values significantly higher than the original model.

Keywords:

Meshless methods; Finite Element Methods; Bio-Inspired Remodelling Algorithm; Structural optimization; Perseverance Rover

Resumo

A exploração espacial tem sido consistentemente um estimulador dos avanços tecnológicos, impulsionando inovações em vários campos da engenharia e expandindo os limites do que é possível em ambientes extremos. Em particular, a otimização de componentes de rovers para missões extraterrestres tornou-se uma área crítica de foco, dado que estes dispositivos devem combinar designs leves, alta durabilidade e adaptabilidade às condições adversas e imprevisíveis encontradas em corpos celestes como a Lua e Marte. Este trabalho explora o potencial dos métodos numéricos avançados, especificamente o Método de Interpolação de Ponto Radial (RPIM) e o Método de Interpolação de Ponto Radial Vizinho Natural (NNRPIM), para análise estrutural e otimização de projeto quando combinados com o Algoritmo de Remodelação Bio-inspirado (BIRA). Estes métodos sem malha apresentam vantagens significativas em relação aos Métodos de Elementos Finitos (MEF) tradicionais, incluindo a capacidade de lidar com grandes deformações e geometrias complexas sem distorções de malha. Esta tese culmina na análise do componente do rover Perseverance que liga a roda à suspensão. O resultado são seis modelos otimizados que apresentam valores de rigidez significativamente superiores ao modelo original.

Palavras-chave:

Métodos Sem Malha; Métodos de Elementos Finitos; Algoritmo de Remodelação Bio-inspirado; Otimização Estrutural; Perseverance Rover

Index

List of Figures

List of Tables

Acronyms and Symbols

Acronyms

ACS	Attitude Control System
AD	*Anno Domini*
ALMA	Atacama Large Millimeter Array
ARTEMIS	Adams-based Rover Terramechanics and Mobility Interaction Simulator
BCE	Before Common Era
C&DH	Command and Data Handling
CAD	Computer Aided Design
CFC	Carbon Fibre Composites
CNES	*Centre National d'Etudes Spatiales*
CSTM	Core Sample Transportation Mechanism
DEM	Diffuse Element Method
DOF	Degrees Of Freedom
EFGM	Free Galerkin Method
EPFL's	*Ecole Polytechnique Federale de Lausanne*
ESA	European Space Agency
FEA	Finite Element Analysis
FEM	Finite Element Methods
FSA	Russian Federal Space Agency
GEO	Geosynchronous Earth Orbit
GN&C	Guidance Navigation and Control
GSLV	Geosynchronous Satellite Launch Vehicle
GTSC	Geotechnical Triaxial Strength Cell
HP^3-Mole	Heat Flow and Physical Properties Package
ICBM	Intercontinental Ballistic Missile
ISA	Iranian Space Agency
ISEP	*Instituto Superior de Engenharia do Porto*
ISRO	Indian Space Research Organization
JAXA	Japan Aerospace eXploration Agency
JPL	Jet Propulsion Laboratory

LEO	Low Earth Orbit
LPS	Laser Power Supply
LRV	Lunar Roving Vehicle
MER	Mars Exploration Rovers
MFEM	Meshless Finite Element Method
MIT	Massachusetts Institute of Technology
MLPG	Meshless Local Petrov–Galerkin
MLS	Moving Least Square
MMRTG	Multi-Mission Radioisotope thermoelectric generator
MPF	Mars Pathfinder
MQ-RBF	Multiquadric Radial Basis Function
MSL	Mars Science Laboratory
NASA	National Aeronautics and Space Administration
NEM	Natural Element Method
NNRPIM	Natural Neighbour Radial Point Interpolation Method
NREM	Natural Radial Element Method
NSAU	National Space Agency of Ukraine
P.Porto	*Instituto Politécnico do Porto*
PIM	Point Interpolation Method
PSLV	Polar Satellite Launch Vehicle
PWA	Printed Wiring Assembly
PWB	Printed Wiring Board
RBF	Radial Basis Function
RCS	Reaction Control System
RKA	Russian Federal Space Agency
RKPM	Reproducing Kernel Particle Method
RPIM	Radial Point Interpolation Method
SHERLOC	Scanning Habitable Environments with Raman & Luminescence for Organics and Chemicals
SPH	Smooth Particle Hydrodynamics
STS	Space Transportation System
TETRA10	Tetrahedral finite elements with 10 nodes
UCZ	Ultra Clean Zone

USA	United States of America
USSR	Union of Soviet Socialist Republics
UT	Universal Time
UTC	Coordinated Universal Time
SED	Strain Energy Density
NNRPIM(V1)	Natural Neighbour Radial Point Interpolation Method 1 degree of neighbourhood
NNRPIM(V2)	Natural Neighbour Radial Point Interpolation Method 2 degrees of neighbourhood

Symbols

φ_i	i^{th} component of the shape function
n	Number of nodes within the influence domain of the integration point
$\boldsymbol{u_s}$	Vector containing the field variable components of each node
d	Dimension applied to the influence domain
h	Average nodal spacing in the surroundings of a node
A	Area
V	Voronoï diagram
V_i	Voronoï cells
$u(x)$	Field function
α	Dimensionless parameter used to scale influence domains
$\boldsymbol{x}_I$	Integration point
$\phi(\boldsymbol{x}_I)$	Interpolation function of $\boldsymbol{x}_I$
$\boldsymbol{x}_i$	Node
ζ	General direction assumed
$\widehat{\omega}_I$	Cartesian integration weight of each integration point
$\boldsymbol{R}$	Radial Basis Function matrix
$\boldsymbol{P}$	Polynomial basis matrix
c	Adjustable constant for Multiquadric Radial Basis Function
p	Adjustable constant for Multiquadric Radial Basis Function
E	Young's modulus of the material
G	Elastic shear modulus
ν	Poisson's ratio
$\boldsymbol{K}$	Global stiffness matrix
t	Thickness

$\mathit{\Omega}$	Problem domain
$\mathit{\Gamma}$	Surface boundary
$\mathit{\Gamma}_t$	Natural boundary where forces are applied
$\mathit{\Gamma}_u$	Essential boundary where displacements are prescribed
d	Vector of nodal parameters
$\boldsymbol{B}(\boldsymbol{x}_I)$	Deformation matrix
$\boldsymbol{D}$	Material constitutive matrix
h	Nodal spacing in the domain
c	Vector representing coefficients in polynomial or RBF functions
k	Parameter defining the influence domain dimension
$\boldsymbol{b}$	Body forces applied on a surface boundary
$\bar{\boldsymbol{t}}$	External forces applied on a surface boundary
$\boldsymbol{f}_{\mathrm{t}}$	External forces vector
$\boldsymbol{f}_b$	Body forces vector
W	Work
$\boldsymbol{\varepsilon}$	Deformation tensor
$\boldsymbol{\sigma}$	Strain tensor
ρ_{app}	Bone tissue apparent density
σ_i^c	Ultimate compression stress
t_j	Fictional time
$\boldsymbol{U}$	Strain energy density field
L	Length
D	Width
P	Load
v	Displacement along y
u	Displacement along x
F	Force
m_i	Initial mass
α	Growth rate
(β)	Decrease ratio
k	Stiffness
A_i	Initial area
σ_{ced}	Yield strength
|u|	Displacement module

1. Introduction

Space exploration has driven technological innovation, achieving significant milestones and advancements in device performance. Optimizing the structural components of space exploration devices is essential for improving efficiency, functionality, and reliability, enabling more ambitious missions. One promising approach lies in the application of advanced numerical methods, such as the Radial Point Interpolation Method (RPIM) and the Natural Neighbour Radial Point Interpolation Method (NNRPIM), to the structural analysis and design of space components. By pairing these numerical methods with Bio-Inspired remodelling algorithm (BIRA) it is possible to obtained optimized models for components.

This chapter introduces the contextualization, motivation, objectives, and structure of the present dissertation, which focuses on using the RPIM, NNRPIM and BIRA in the context of optimizing rover components for space exploration.

1.1. Contextualization

From the launch of the first object into space to the present day, space exploration has seen major milestones achieved as well as technological advances. To be able to carry out new missions, in the quest to better understand space, it is necessary to improve the performance of space exploration devices. One way to do this is by focusing on the structural optimization of the components that make up the devices, seeking to increase efficiency, functionality and reliability. To this end, the remodelling algorithm Bio-Inspired remodelling algorithm (BIRA) is paired with the numerical method Finite Element Methods (FEM) and meshless methods, where the RPIM and the NNRPIM are included. These advanced discretization techniques emerged as an alternative to the commonly used FEM and present the great advantage of being able to simulate large deformations and more complex structures without facing mesh distortions. Although some of these methods need a background mesh, the ones categorized as truly meshless methods, like NNRPIM, do not need a mesh at all.

1.2. Motivation

Currently, even after decades of evolution in the sector, the cost of launching devices into space, as well as the payload and volume limit of launch devices, are still very limiting factors in space exploration. Until 2018, the cheapest way to launch a payload, using a ratio of kg per $, was to resort to the Falcon Heavy rocket, which has a payload capacity of 63800 kg with a cost of 1.41 $k/kg [1]. With all the costs associated with a rover mission, it is expected that the mission will be able to fulfil all previously proposed objectives. For this, it is necessary to have a rover whose components, in addition to fulfilling their function, are reliable, with a reduced mass in order to reduce the energy necessary for their launch to space and locomotion.

The approach to the challenges presented is to study launched rover components using advanced discretization techniques, such as the meshless methods RPIM and NNRPIM, to structurally analyse and optimize those components, pairing the numerical methods with BIRA. In this way, it is possible to develop new designs for components that can maintain their functionality but reduce their mass or dimensions, possibly reducing the operational costs, making room for the incorporation of more devices for the study of the environment or improving the rover’s capabilities.

1.3. Objectives

The main goal of this dissertation is to develop a design with higher stiffness than the original design of the component using FEM, RPIM and NNRPIM. In order to accomplish that, the following objectives are set:

- A review of space technologies culminating in an analysis of some rover’s aspects from structural point of view;
- Writing and understanding the mathematical formulation of the meshless methods RPIM and NNRPIM;
- State of the art regarding analysis of rover components using FEM or meshless methods;
- Solving benchmark topology optimization studies;
- Remodelling analyses on the selected rover’s component and comparison with the original design in terms of structural integrity and mass reduction.

1.4. Structure

This document is divided into eight chapters being them: 1 Introduction, 2 Space Technologies, 3 Meshless Methods, 4 Bio-Inspired Remodelling Algorithm (BIRA), 5 Computational Applications, 6 Numerical , 7 Remodelling and 8 Conclusions and Final Remarks.

In chapter 1, a brief introduction of the work is presented alongside a contextualization of the topics to be covered throughout the dissertation. The motivation for carrying out this work is presented, and the objectives to be accomplished at the end of it are described. Chapter 2 presents a review of the space technologies used since the early steps in space exploration until modern times. Starts with an overview of space exploration, its history and space transportation mechanisms. Then, different types of space exploration devices are presented, mission costs (launch cost and cost of rovers and landers themselves), the advantages of space technologies are presented and, lastly, a more in depth review of rovers is shown, focusing on the history of past rovers, types of rover mobility, methods of sample acquisition, planetary environment, and materials for space applications. The chapter culminates in a review of the Perseverance rover which will be the object of study of the future dissertation. In chapter 3, a bibliographic review on meshless methods is done leading to the description of the mathematical formulation of the RPIM and NNRPIM methods, which will be used to carry out the structural analysis and optimization of Perseverance rover components. Chapter 4 shows an explanation of the Bio-Inspired remodelling algorithm (BIRA) used in this work for the remodelling analyses, presenting a description of its mathematical formulation. Chapter 5 is dedicated to the state of the art, divided into subsections that deal with distinct rover's components as well as the rover's interactions with soil. Studies that analyse some rover's components using the FEM or meshless methods are presented. Critical comparisons between studies are carried out in order to further understand the subject matter. In chapter 6, in order to validate the numerical methods used, some benchmark problems are solved: the 2D and 3D cantilever beam and a problem for the remodelling algorithm only in 2D. All the work culminates in chapter 7 where, using all the methods presented, it is proceeded to the remodelling of the component. In the end, 6 distinct optimized models are presented. Lastly, in chapter 8, the conclusions of the dissertation are drawn up, the limitations during the work are presented and, in the end, it is showcased the adopted workplan.

2. Space Technologies

Throughout this chapter, the use of space by human beings and their exploration will be discussed, as well as the methods and devices that allow this to be achieved.

Since the beginning of time, the curiosity to know what exists beyond Earth has been awakened in human beings and space has been part of our activities for as long as we have known. For the humans in ancient times, space was a means of identifying orientations using sunrise and sunset. Then, when humankind started their first naval explorations, instruments such as astrolabes began to be used as a way to navigate during the night, measuring the altitude of stars and other celestial bodies on the horizon and to determine their position.

All this time of eyes fixed on the sky has raised several questions about what space is and how it works. These questions have been studied by philosophers and astronomers who, over the years, have led us to the definition of space as we know it today.

Space is characterized by modern physics as continuous, isotropic, homogeneous, finite or infinite, ignoring some relativistic theories [2]. In space there are numerous celestial bodies such as planets, natural satellites, asteroids, comets, stars that exert gravitational forces upon each other causing them to orbit each other forming systems such as the solar system.

2.1. Space exploration

Space exploration began from the ambition and curiosity to better understand the Solar System and the Universe, as well as the formation of every celestial body out in space. For that, human beings were forced to try new forms of exploration and study, reaching space exploration.

2.1.1. History of space exploration

Space exploration successfully started in the year 1957 with the launch of the first artificial satellite on Earth, Sputnik 1 on October 4 at 19:28:34 UTC (Coordinated Universal Time), although the development of the satellite began in November 1956 [3]. The success of this mission opened a door to space exploration as we know it today.

The next great achievement was the first manned spaceflight in the mission Vostok 1 where Yuri Alekséyevich Gagarin, selected for the mission, is launched on April 12, 1961, 06:06:59,7 UTC, reaching orbit at 06:17 UTC and starting re-entry process at 07:25 UTC landing at 07:55 UTC in the Saratov region 01:48 after its launch [3].

The following year mission Mariner II, managed by NASA (National Aeronautics and Space Administration) /JPL (Jet Propulsion Laboratory) in the USA (United States of America), became the first successful planetary mission launching the spacecraft on August 27 at 06:53:14 UT with the objective of flyby Venus accomplishing that mission on December 14, 1962 at 19:59:28 UT (Universal Time), passing by Venus at a distance of 34854 km where the spacecraft proceed to scan the planet during 42 minutes gathering information about the atmosphere and terrain of the planet [4].

One of the greatest milestones ever achieved in space exploration was the landing of man on the moon, with the Apollo 11 mission in the Apollo program, conducted by NASA. In this mission, Michael Collins, Edwin Eugene Aldrin Jr, and Neil A. Armstrong landed on the Moon's surface on July 20, 1969 at 20:17 UTC [3].

The mission Luna 17 and Lunokhod 1, executed in USSR (The Union of Soviet Socialist Republics), put a rover on a celestial body for the first time in history. Launched on November 10, 1970 at 14:44:01 UT, the Luna 17 entered lunar orbit and later landed on the lunar surface at 03:46:50 UT on November 17, 1970 at 38° 24′ N / 34° 47′ W (as known at the time). The rover travelled a total of 9.93 km during its 322 days of operation, returned more than 20 000 TV images and 206 panoramas and performed 25 soil analyses until communication was severed on September 14, 1971 at 13:05 UT [4].

2.1.2. Space transportation and launching mechanisms

To accomplish all the space missions, there must be a way to put a spacecraft in space and that spacecraft needs to be able to navigate in outer space. The solution to reaching escape velocity and making it possible to explore beyond Earth are rockets.

The first idea of something similar to a rocket appears in the writings of a Roman author, Aulus Gellius around 400 BCE (Before Common Era). In his work, Aulus states that a character named Archytas used a wooden pigeon suspended by wires and propelled by steam to amaze the locals. This is the earliest mention in the history of a man using Newton's Third Law for propulsion, the main principle behind a rocket operation [5]. Between the years 0 to 100 AD (*Anno Domini),* it is speculated that the Chinese started experimenting with potassium nitrate (KNO_3), sulphur (S), and carbon (C), which are the basic compounds of gunpowder. That began to appear in registers from the year 850 in a book translated as "Classified Essentials of the Mysterious Tao of the True Origin of Things", where Taoist alchemists accidentally obtained gunpowder that started to get used in warfare by the Chinese in the year 904. Only from the year 1132 it began to be used as a propellant, with the first rocket ending up being used against Mongols in 1279 at the battle of Kai-Keng. Later, around the year 1300, it was discovered a way to improve the accuracy of rockets by launching them from a tube, giving birth to the bazooka and launch tube. In the seventeenth and eighteenth centuries, there was a great development in the understanding of the principles of rockets, culminating in the laws of motion of Isaac Newton published in "Principia" in 1687. Konstantin Tsiolkovsky, in the year 1903, published the book "The Exploration of Cosmic Space by Means of Reaction Devices", where he describes most of the aspects of modern rocket science. In 1930 was founded the American Rocket

Society, where some experiments with rockets were led, and later, in 1933, the Soviets experimented with a rocket with solid and liquid engines. The pace of rocket evolution quickened when German scientists concentrated on developing weapons for Hitler, emerging with the famous V1 and V2 rockets. Until these times, rockets were mostly used in warfare but that changed with the space race between the USA and USSR. This competition greatly contributed to the development of rockets and the advancement of space exploration achieving great milestones in the time when rockets began to be used as a launching vehicle instead of weapons. That lasted until the mid-1970s, when the stressed economies of the USA and Russia couldn't maintain the pace of spacecraft evolution, causing a great regression in space exploration. In the same years, USA experimented with partially reusable launch vehicles called space shuttles that stayed operational until July 21, 2011 [5].

Nowadays, there are many space agencies that contribute to the development and production of their own launch vehicles. ESA (European Space Agency) has at the moment the Ariane 5 and the Soyuz launch vehicles being the last bought from the Russians, and, in cooperation with the Italian Space Agency, they are developing the Vega, a new launch vehicle. ESA also has CNES (*Centre National d'Études Spatiales*) as a partner, which has the Ariane 5 as their main launch vehicle. ISRO (Indian Space Research Organization) possesses the PSLV (Polar Satellite Launch Vehicle) that has been used since 1993 and the GSLV (Geosynchronous Satellite Launch Vehicle) since 2001. ISA (Iranian Space Agency) has been developing launch vehicles based on Taepodong 2 from North Korea, possessing the Shahab family of rockets that has the same objective as the ICBM (Intercontinental Ballistic Missile), but ISA is continuing research in launch vehicle technologies. The Israeli Space Agency developed the Shavit launch, which proved to be unreliable, leading the space agency to opt for the ISRO's PSLV for some of their missions. JAXA (Japan Aerospace eXploration Agency) has in their fleet the H-IIA and the H-IIB which were developed by Mitsubishi and ATK Thiolkol. The H-IIA began its missions in 2001 and the H-IIB, still under development, in 2006. JAXA also has at their disposal the M-V line of launch vehicles designed by Nissan, using the LG-118A Peacekeeper ICBM as a model. CNSA (China National Space Administration) has possessed the Long March family of rockets since the 1970s, developed mainly from the Dong Feng ICBM's. This family of rockets has launch vehicles capable of missions ranging from small payloads for LEO (Low Earth Orbit) to heavy payloads for GEO (Geosynchronous Earth Orbit). FSA (Russian Federal Space Agency), also known as RKA in Russian, was a collaboration between Russia and Ukraine, although nowadays NSAU (National Space Agency of Ukraine) and RKA are two separate entities. The FSA has a very developed launch vehicle program, mainly potentiated by the space race. In 2017 the rockets in use were the Rockot, the Kosmos, the Dneper, the Tsyklon, the Soyuz, the Zenit and the Proton. NASA/U.S. Air Force had the manned program known as STS (Space Transportation System) from 1981 to 2011 composed of Space Shuttles, a partially reusable launch mainly used to send humans into LEO. Since the end of this program, there has been no replacement manned launch system to perform the space shuttle's duty. Nowadays, NASA has mainly two families of launch systems, the Atlas family built by Lockheed Martin and the Delta family built by Boeing [5].

In general, rockets from diverse space agencies are similar to each other and the rocket's components can all be grouped into the several categories, taking into account their function.

Falling into the category of structural components are the air frame, section fairings, environmental protection, support structures and mechanisms. In the propulsion category can be found the fuel, oxidizer, pumps, combustion chamber, igniters, nozzles, and flow systems. Power storage, power conditioning and power transfer are all part of the power category. GN&C (Guidance Navigation and Control) is the category where the thrust vectoring, control surfaces, ACS (Attitude Control System), RCS (Reaction Control System), navigation sensors, and computers are. Payload is the reason to launch the rocket and encompasses the mission components, payload fairing, LV interface and deployment systems. The C&DH (Command and Data Handling) category covers the command computers, data processing, data storage and data distribution. In communications are radios and antennas. Re-entry systems, only needed in some missions, are part of the braking system and the thermal protection system. Also required in some missions, the landing systems are a category that has parachutes and impact dampening systems. Finally, the abort systems, fire control and redundant systems all are part of emergency systems [5].

2.1.3. Space exploration in modern times

Nowadays, missions carried out in space fall into 3 categories. The first type of missions are the military missions, and these were the missions that initially led to the development of space technologies. Normally, these types of missions come down to placing spy satellites in a determined orbit or telecommunication satellites. Commercial missions also revolve around the launching of satellites to orbit, mainly for telecommunication use. The objective of any commercial mission is to make profit, this way creating countless possibilities such as space expeditions. At last, there are the science missions. These are the missions that propel the evolution of space technology as well as humankind's understanding of the universe. Ranging between LEO and going beyond the solar system, there are diverse operations since the observation of the universe through telescopes such as the Hubble Space Telescope. This includes the analysis of Mars’s terrain and the search for past or present existence of life from programs like NASA’s Mars Exploration Program.

2.2. Space exploration devices

Space exploration can be done by observation, whether from Earth or in space, or by analysis of the celestial body under study. For all the circumstances, mankind has developed several devices in order to make it possible to practice the intended studies. The different ways to explore space consist of earth-based observations, airborne and orbital telescopes, probes and flyby spacecraft, Orbiters, Landers, and Rovers.

2.2.1. Earth-based observations

To observe the space without exiting Earth, there are devices that detect the electromagnetic radiation. This detection is divided into: optical detection, radio and microwave detection, X-ray and Gamma-ray detection, cosmic ray detection, neutrino detection, gravitational detection and dark matter and dark energy detection. From these forms of detection not all of them can be made from Earth because Earth's atmosphere creates a barrier, as shown in Figure 1, for some electromagnetic radiation making it impossible to detect any of that radiation with devices on ground [6]. Despite that barrier, there are still devices being used to observe space like the South African MeerKAT radio telescope, the Gemini Observatory located in Hawaii and Chile and ALMA (Atacama Large Millimeter Array) located in Chile, shown in Figure 2 a).

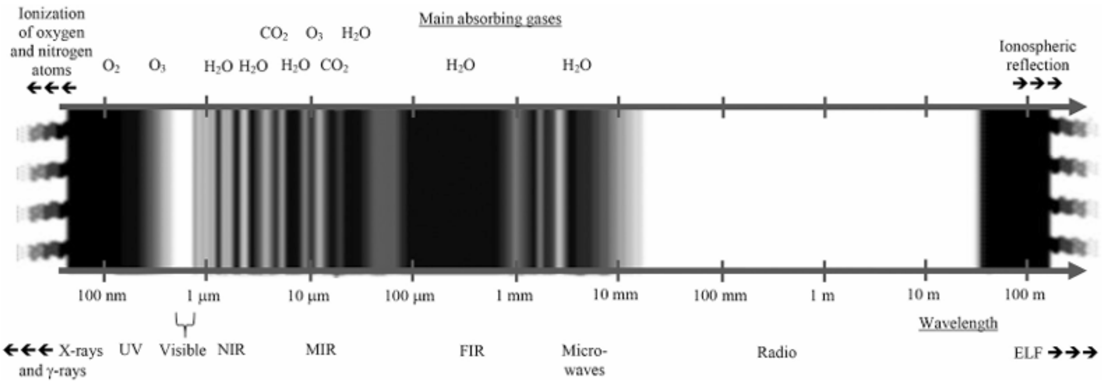

Figure 1 - The transparent and partially transparent spectral regions of the Earth's atmosphere and main causes for the opaque regions [6]

2.2.2. Airborne and orbital telescopes

To surpass the barrier created by Earth's atmosphere, there is the need to "take it out of the way". That can only be made by launching the telescopes to the space. Nowadays, these types of telescopes are most important because of the lack of filtration of electromagnetic radiation. Some well-known Orbital telescopes are the Hubble Space Telescope, shown in Figure 2 b), James Webb Space Telescope and the space observatory Gaia.

2.2.3. Probes and flyby spacecraft

Probes and Flyby spacecrafts were mainly used in the first steps of space exploration. In their missions, the spacecraft passes by celestial bodies in study at a sufficient distance that it is not caught by the gravitational field of that body. A great example of a flyby spacecraft is the Voyager 1, shown in Figure 2 c), still in use since 1977.

2.2.4. Orbiters

Differing from the Flyby spacecraft, Orbiters are built with the aim of orbiting another planet. They are used after the Flyby spacecraft to further continue the exploration of the given planet. There are many examples of Orbiters, some of the most important being the Messenger orbiting Mercury, the Mariner 9 orbiting Mars and Cassini-Huygens orbiting Saturn, shown in Figure 2 d).

2.2.5. Landers

These devices are design to soft land on other planet's surface, being the first type of spacecraft to enter other planet's atmosphere and stay on mission for a long period of time. They require a landing system that can make the mission more expensive and are stuck in a specific location, limiting their exploration capabilities. Some examples of Landers are the Venera Landers used in Venus, the Surveyor used on Moon and the InSight used on Mars, shown in Figure 2 e).

2.2.6. Rovers

Nowadays, this is the last step of planet exploration since humankind last went to the moon. These spacecrafts are capable of exploring several aspects of the surface and atmosphere of planets with components that make it possible to operate in harsh conditions. Provided with locomotion systems, these offer a great improvement over landers. Mainly, rovers are autonomous, but they can be operated either on site or on earth. The prime examples of Rovers are Perseverance and Curiosity, shown in Figure 2 f), on Mars and the first Rover to ever operate, Lunokhod 1 on the Moon.

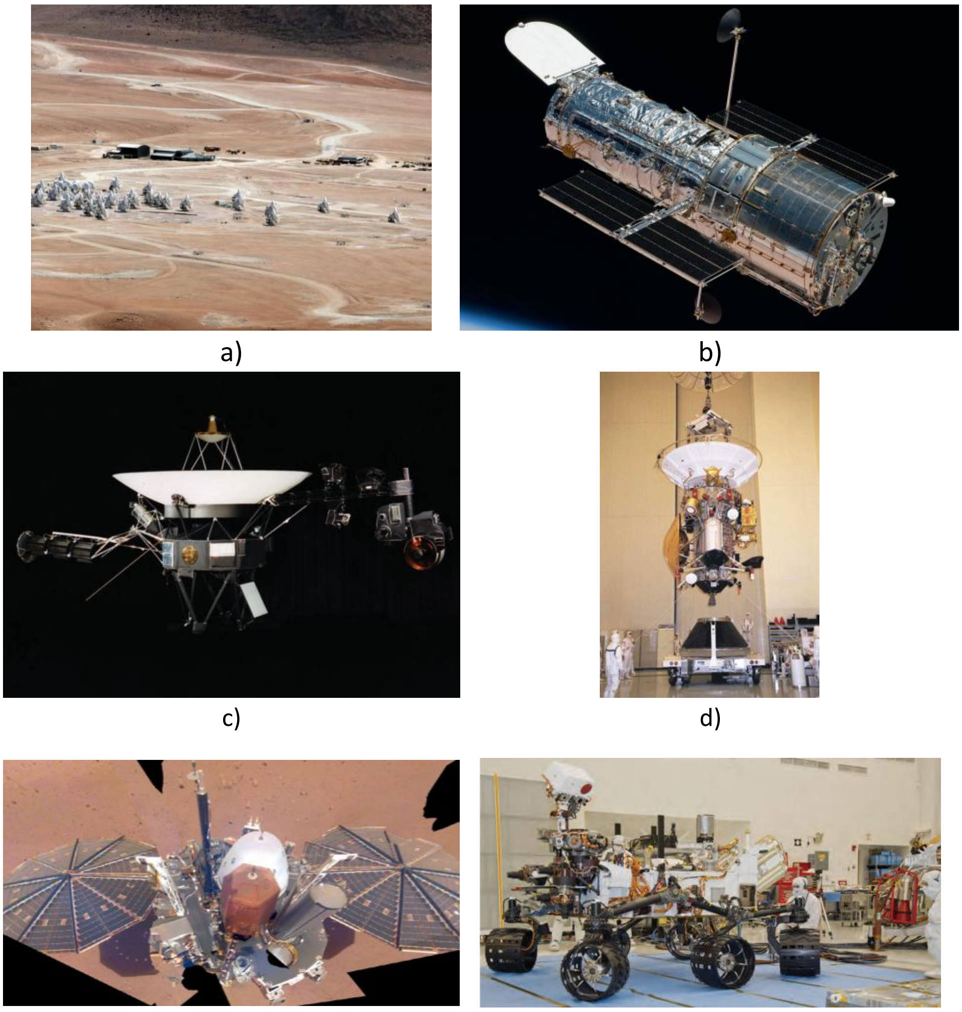

a) b) c) d) e) f)

Figure 2 - a) ALMA [7] b) Hubble Space Telescope [8] c) Voyager 1 [9] d) Cassini [10] e) Insight lander [11] f) Curiosity rover [12]

2.3. Mission costs

Space exploration entails high costs, from the development and construction of space exploration devices to the launch of some of these devices to orbit or other missions in deep space. This has been the main obstacle to the evolution of space exploration, in the absence of economic support, it is not possible to carry out the technological development necessary to achieve new goals or support the costs of all payloads launching operations into space. In this chapter, the costs of space exploration will be divided into payload launch costs and rovers and landers costs.

2.3.1. Payload launch costs

The first step to send a rover to another planet is to launch it into space, and that is accomplished using rockets. One of the reasons to the low number of spacecraft launches is the economic factor, since the price per kg of the payload is relatively high. This problem led to the development of cheaper alternatives, re-investing in reusable techniques in order to save costs. In this way, a launch system can be used several times, thus removing the costs of building new rockets with each launch.

Since the beginning of space exploration until now, the space industry has seen a great improvement in launching costs has it is shown in Figure 3. Although this reduction in costs on Falcon Heavy, Saturn V still has the advantage of being able to transport more payload to LEO as can be seen in Table 1.

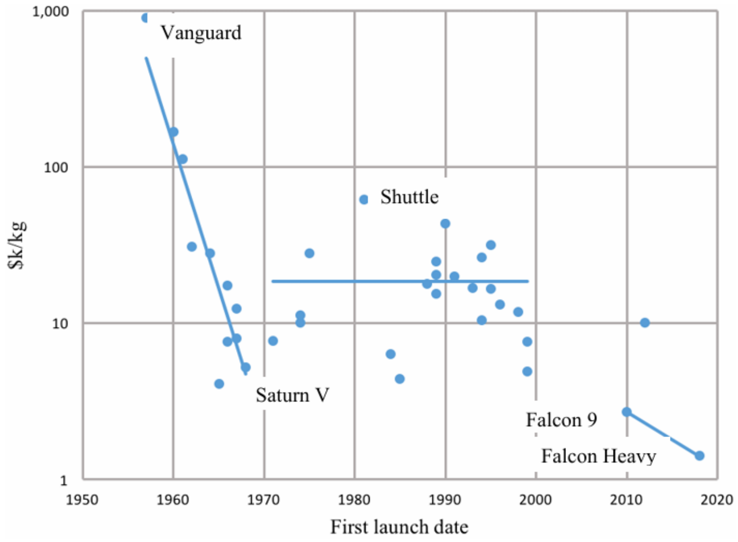

Figure 3 - Launch cost per kilogram to LEO vs first launch date (until 2018) [1]

Table 1 - Launch cost to LEO for Saturn V, space shuttle, Falcon 9, and Falcon Heavy [1]

System	Saturn V	Shuttle	Falcon 9	Falcon Heavy
kg to LEO	140000	27500	22800	63800
Cost per launch 2018 $M	728	1697	62	90
2018 $k/kg	5.20	61.72	2.72	1.41

In relation to launch services costs for missions on Mars, historically, the values ranged from $90M for the Pathfinder mission to $551M for the Viking 1 & 2 mission as can be seen in Table 2. These values vary due to payload mass launched and the launch vehicle used [13].

Table 2 - Launch costs of Mars landed missions [13]

Mission	Viking 1 & 2	Pathfinder	Mars Polar Lander + Mars Climate Orbiter	Mars Exploration Rovers	Phoenix	Mars Science Laboratory Curiosity Rover	InSight	Mars-2020 Perseverance Rover
Year	1975	1996	1999	2003	2007	2011	2018	2020
Launch costs FY22 $M	551	90	151	150	118	256	185	267

2.3.2. Rovers and landers costs

Only accounting for the costs related to the rover development and operation (not including launch services costs), the costs associated with rovers and landers expeditions, presented in Table 3, vary between $397M for the Pathfinder mission and $3.4B for the Mars Science Laboratory mission, excluding mission Viking 1 & 2 that had the development of 2 orbiters associated with the overall costs [13]. It can also be observed that operating costs are not nearly as high as development costs, which leads to the conclusion that for rover and lander missions, the biggest challenge lies in reducing production costs.

Table 3 - Information of Mars landed missions [13], [14]

Mission	Type	Year	Development Costs, FY22 $M	Development Duration, yrs	Mission Operation Costs, FY22 $M	Mission Operation duration, yrs
Viking 1 & 2	2 Landers + 2 Orbiters	1975	6165	7	528	4, 6
Pathfinder	Lander with Rover	1996	371	4	26	0.25
Mars Polar Lander Mars Climate Orbiter	Lander + Orbiter	1999	336	4	27	____
Mars Exploration Rovers	2 Rovers	2003	1001	4	444	6, 15
Phoenix	Lander	2007	441	5	16	1
Mars Science Laboratory Curiosity Rover	Rover	2011	2839	10	596	10
InSight	Lander	2018	683	8	68	4 [14]
Mars-2020 Perseverance Rover	Rover	2020	2395	8	297 (until 2022)	Until today

2.4. Advantages of space technologies

Space technologies are currently very present in the society we live in, significantly contributing to the quality of life on Earth. These technologies are used in various scientific and even economic fields, proving to be useful in many ways. Here, some of the ways that space technologies benefit life on Earth will be described [15].

In climate**,** over 99% of accurate weather forecasts come from space, since over half of the important factors can only be measured by satellites, enabling an analysis of climate change and evolution. Also, at the moment, more than 160 satellites are being used to measure climate change indicators providing a vast database that can be used to predict the effects at regional, territorial and national scales. All this information can be used to raise awareness of the negative climate effects, providing some significant data for the decision-making on the implementation of protective measures in order to mitigate the effects [15].

Over 2000 navigation and communication satellites provide global coverage, enabling the transmission of world events and can help to connect 49% of the world's unconnected people. Also, provide Earth observations on navigation services that are used by some applications and in air travel too, and can supply software and firmware updates for connected devices. After COVID-19, satellite broadband connections had a 70% increase in Latin America, Central, and Western Europe. Satellites are being used to help in disaster response as well [15].

Space technologies help to prevent misunderstandings and encourage international cooperation as is the case with the ISS (International Space Station), which is shared by 14 countries. Satellites have been used to control nuclear arms treaties for over 50 years, contributing to the verification of the CTBT (Comprehensive Test Ban Treaty). Over 600 satellites see over borders promoting transparency along countries and about 55 meteorological satellites contribute to weather sharing, helping to prevent loss of lives and properties in case of natural disasters [15].

There has been an increase in the number of satellites in the last years, accompanied by a reduction in manufacturing costs. For example, since 2013 there was an 80% reduction of satellite Gpbs's manufacturing costs. This comes from the increase in the number of space companies that provide several products and services, increasing competitiveness as a result. Satellites are being used by telecommunication, internet and other industries, thus contributing to the global economy [15].

2.5. Definition of a rover

A rover is a mobile robot designed to operate in extraterrestrial soil and serve the purposes of studying the terrain and atmosphere (if present on the celestial body in study), searching for water in any state and remains of ancient life.

2.5.1. History of past rover missions

Most of the planetary rovers, with a few exceptions, have been designed with a wheeled chassis as this provides mechanical simplicity and high reliability. Some of the most successful rover missions are the Lunokhod, LRV (Lunar Roving Vehicle), MPF (Mars Pathfinder) Sojourner, MER (Mars Exploration Rovers), MSL (Mars Science Laboratory) [16].

In the Lunokhod mission, two rovers were used, Lunokhod 1, shown in Figure 4 a), launched in 1970 which had a mass of 756 kg, and the 840 kg Lunokhod 2 launched in 1973. They were two similar rovers with an 8-wheeled chassis in order to reduce the wheel size without reducing traction. A deployable ninth wheel was used to measure the distance travelled without slip. These rovers had two different gear speeds, one providing a speed of 0.8 km/h and the other 2 km/h, could operate in a maximum slop of around 22 to 27° and steering was made through the skidding direction. They were remotely operated from Earth by five-man teams, with a signal delay of 2.5 s for Lunokhod 1 and 3 s for Lunokhod 2 [16].

The LRV, shown in Figure 4 b), used in Apollo 15, 16 and 17 differed from every other rover to date, since these were operated manually by astronauts on the Moon in 1971 and 1972. With a four wheeled chassis, the rover had a mass of 218 kg with a capacity of 490 kg. Its chassis had a length of 3.1 m, a wheelbase of 2.29 m, was made from aluminium alloy tubing and was developed to complete four 30 km travels at a speed ranging from 0 to 16 km/h. The steering mechanism used was a double Ackerman steering and could operate in slopes with a maximum angle ranging between 19 and 23° [16].

In 1997, the MPF mission started with the launch of the Mars Pathfinder lander that was carrying the Sojourner rover, shown in Figure 4 c), landing in Martian soil. This relatively small rover had a mass of 11.2 kg, length of 63 cm, width of 48 cm and height of 28 cm. Design as a six wheeled rover, it used a rocker-bogie lever as its suspension. Each wheel was powered individually, and the four outer wheels had an extra motor for steering purposes. It could move at a maximum pace of 0.6 cm/s and at a maximum incline of 45°. It never exceeded more than 10 m away from the lander, travelling a total of 106 m [16].

In the MER mission, two similar rovers were used, one of them shown in Figure 4 c), Spirit and Opportunity, launched in 2004 with a plan for a 90-day mission, which proved to be far short of the final operating time. With the same mass and dimensions of 174 kg, length of 1.6 m and wheel baseline width of 1.22 m and length of 1.41 m, they were six wheeled chassis rovers with rocker-bogie springless suspension similar to Sojourner. The suspension was built from titanium alloy, the wheels from aluminium alloy, and the rover structure from composite panels with titanium alloy fittings. All the wheels were cleated to improve traction and the four corner wheels were steerable for on-the-spot turning with a 1.9 turn radius. They were designed to have an average travel speed of 100 m/day, accounting for the needed stops along the course. The rovers could withstand a lateral inclination of 45° although, through software and an inertial measurement unit, any tilt over 30° was notified with an alarm [16].

Curiosity (shown in Figure 4 c)), the rover used in the MSL mission, landed on Mars in 2012. This was a 899 kg rover with a six wheeled chassis and, similar to the previous rovers, a rocker-bogie suspension system [17]. With a wheel baseline with length of 2.20 m and a width of 2.18 m [17], this rover has a top speed of 4 cm/s, although being normally operated at half the speed [16]. The steering is achieved by the action of the azimuthal actuators using Ackerman arcs of a given radius [17].

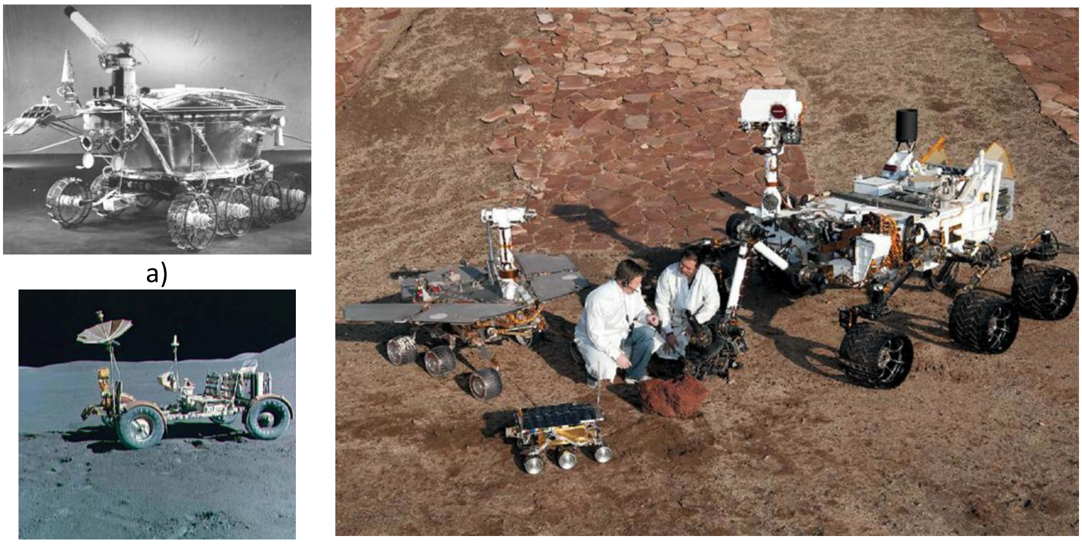

a)

b)

c)

Figure 4 - a) Lunokhod 1 b) LRV c) Sojourner (bottom one), MER (left one) and Curiosity (right one) [16]

2.5.2. Rover mobility

It is necessary to invest in the mobility of the rover because the advantage presented by this type of mission is the fact that these devices can move along the terrain. Nowadays, the rover mobility seems to converge on the use of a six-wheeled chassis with a rocker-bogie suspension system (Figure 5 a)), but there are many more ways a rover can move. Shown in Figure 5 are some options for rover mobility which include: wheeled vehicle, tracked vehicles, legged vehicles, hopping vehicles, and hybrid vehicles.

In the wheeled vehicle's category, there are the four-wheeled, six-wheeled and eight-wheeled vehicles. As stated before, the most common is the six-wheeled type that has more than one variation, like the EPFL's (*Ecole Polytechnique Federale de Lausanne*) Solero rover prototype, with a similar approach to the rocker-bogie suspension but with six independently actuated wheels. These rovers have wheels that vary in designs and dimensions, attached to the chassis, normally with a suspension system. Being used for a long time in vehicles all over the world, this was a safe and logical approach to the mobility problem. Can be included in this category the articulated chassis that still uses wheels but consists in the use of articulated units that connect with the chassis, allowing more freedom of movement to the wheels. These vehicles provide the capacity to explore more robust terrain but at the cost of an increase in mechanical complexity [16].

Tracked vehicles have similar properties to wheeled vehicles but have an advantage in higher tractive missions and offer higher drawbar pull than any wheeled vehicle option. This option provides a high ground contact area, which leads to a high traction on soft ground. In counterpart, they are less efficient mechanically than the wheeled vehicles due to track-ground friction needing higher power requirements. The suspension in this type of vehicle consists of a torsion bar, trailing arm, inclined shock absorber with spring base and stops [16].

In a more experimental design, legged vehicles appear following biological designs and neurobiological controls and looking forward to a robust and sustainable method of motion. Although never used in space exploration, there are some examples of legged vehicle designs from some robots in use on Earth. Examples of these types of robots are the octapod SCORPION by German Research Center for Artificial Intelligence and hexapod DLR Walker developed by Institute of Robotics and Mechatronics of German Aerospace Center [18].

Hopping vehicles are a cost-effective solution proposed for surface exploration, benefiting from the ability to jump to overcome obstacles on the ground. With these vehicles, the value is on the mechanical simplicity of the system and not on is high mobility capacities. They hop with a determined velocity in a certain trajectory without accuracy on landing and if used in swarms they are capable of exploring wide areas [18].

Hybrid vehicles emerge in an attempt to use the advantages of two or more systems and to decrease the downgrades. Therefore, surge examples like the Wheel-leg hybrids like the DLR's hybrid concept and the Hop-roll hybrid like the Microbot presented by Massachussetts Institute of Technology [18].

In order to compare the performance of the diverse types of mobility systems, Table 4 shows several of their characteristics.

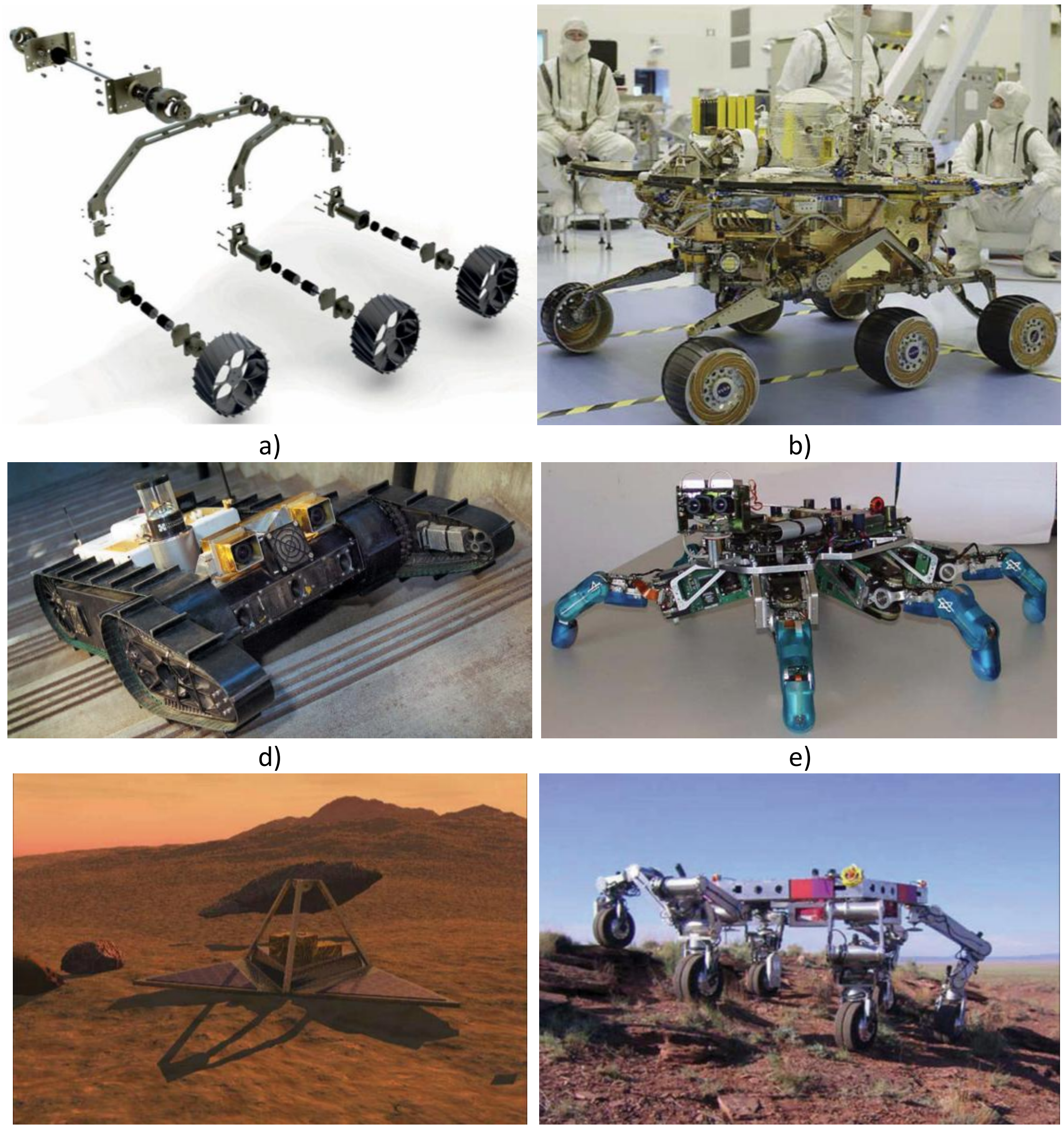

a) b)

d) e)

e) f)

Figure 5 - a) Rocker-bogie suspension system (Kapvik rocker-bogie assembly) [16] b) Wheeled vehicle (Spirit of MER) [18] c) Tracked vehicle (Urban II rescue robot) [16] d) Legged vehicle (DLR Walker robot) [18] e) Hopper vehicle (CSA's Micro-hopper) [18] f) Hybrid vehicle (Wheel-leg Hybrid system ATHLETE) [18]

Table 4 - Qualitative analysis of the mobility systems [18]

Metrics	Wheeled vehicles	Tracked vehicles	Legged vehicles	Hopping vehicles	Wheel-leg hybrids	Hop-roll hybrids
Maximum speed	30 cm/s	30 cm/s	30cm/s	> 45 cm/s	>45 cm/s	> 45 cm/s

Obstacle traverse capability	20-30cm	30 cm	> 30 cm	> 30 cm	> 30 cm	> 30 cm
Slope climb capability	15-25°	30°	30°	> 35°	> 35°	> 35°
Soil sinkage	Medium	Low	High	Very Low	Medium	Very Low
Mechanical simplicity	Medium	Low	Low	High	Very Low	High
Mobile element redundancy	High	No redundancy	High	No redundancy	Very High	No redundancy
Energy consumption	Low	High	Very High	Low	Very High	Very Low
Payload mass fraction capacity	8-12%	8-12%	5-8%	12-15%	> 15%	12-15%ml
Soil interaction	Medium	High	Low	High	Medium	Very High
Technology readiness level	TRL 8 or 9	TRL 5	TRL 3 or 4	TRL 3 or 4	TRL 5	TRL 3 or 4

2.5.3. Sample acquisition

The main objective of a rover mission is to carry the needed tools to perform the necessary studies, mainly soil analysis. Most of the analyses are realized by the rover but, to further analyse the soil with more advanced equipment, one can resort to obtaining samples and subsequently sending them to Earth. For that, the first step is to acquire samples and in order to execute this task diverse mechanisms can be used.

Robotic manipulators, as shown in Figure 6 a), are attached to the rover and can be used to acquire samples. To design it is necessary to take into account aspects such as positional accuracy and repeatability, operating cycle time and speed of response, life expectancy, reliability, contact forces and DOF (Degrees Of Freedom) that need to be at least 3 in a robotic manipulator [18].

In order to conduct analysis in rocks, it is necessary a corer/grinder because they often have encrusted dust on their surfaces that needs to be removed to proceed with the analysis. The corer/grinder can be attached to a robotic manipulator, as shown in Figure 6 b).

Subsurface drills (Figure 6 c)) are used to obtain subsurface samples, and the type of sample is defined according to its depth. Near-surface drilling is all the drilling that penetrate to a depth ranging from 5 to 10 cm, shallow depth drilling goes as further as 200 m in depth and deep drilling all the way to 5 km or more. At the time, with the technology available in rovers, only near-surface drilling is possible.

A mole (Figure 6 d)) is a mechanism that could serve as an alternative to drilling, eliminating the need for external mounting platforms, long drill strings, and the autonomous drill segment assembly if used detached and self-propelled. It provides the capacities of penetrators, but with the advantage of being able to perforate specific locations [16].

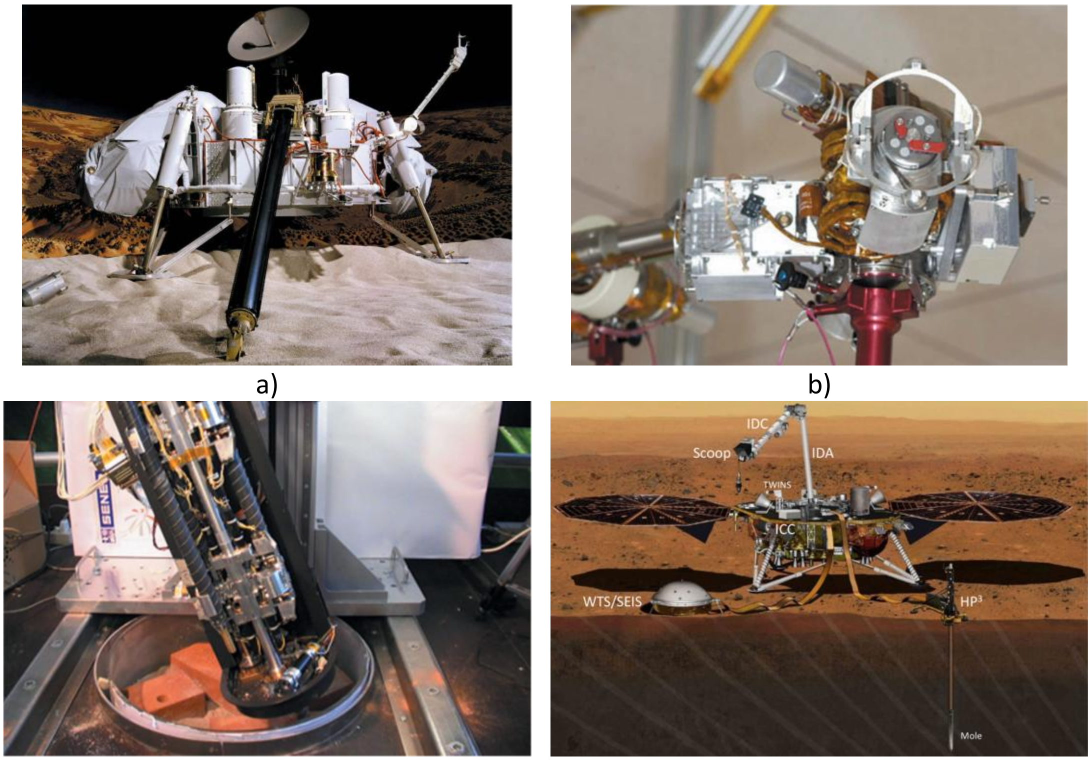

a) b)

c) d)

Figure 6 - a) Soil sampler of Viking lander [16] b) MER rock abrasion tool [16] c) ExoMars rover drill assembly [16] d) InSight lander with mole (bottom right) [11]

2.5.4. Planetary environment

A rover needs to be capable of travelling through an unknown terrain and overcome some obstacles in order to acquire samples and, via other scientific instruments, analyse diverse aspects designated for the mission. For that, the rover needs to overcome the following adversities: adverse terrain with few self-localization features, lack of data about the environment, delay in communications and limited window for communication to Earth, extreme temperatures and dust, limited power and limited mechanical complexity to provide high-reliability. Nowadays, rover missions occur on Mars and the Moon [16].

Earth's only natural satellite, the moon, has no atmosphere and is tectonically dead. It has a surface gravity of 1.62 m^2/s and the temperature at the equator varies between -153 and 107 °C and goes as low as -233 °C at the poles. The moon has a small solid core with roughly a 340 km radius and a crust around 70 km thick and, although some rocks show remains of magnetism, it does not possess a global magnetic field. Moon's terrain is made up of the older rugged highlands of anorthosite (which have high quantities of Ca and Al) and the younger smooth basalt plains (high quantities of Fe and Mg). Lunar rocks present minerals and glass and were formed under almost no oxygen and low pressure and the vast majority of minerals on the Moon are plagioclase feldspar, pyroxene, olivine, and ilmenite. Lunar water has been detected in hydrous mineral apatite, but the analyses concluded that most of this water comes from comets, although it is expected to have ice in permanently shadowed craters at its poles, where the temperature is -174 °C. Lunar dust is present everywhere, being levitated by solar ultraviolet radiation and solar wind flux and due to its properties, and it adheres to everything, which causes a problem for extended lunar operations [16].

With a terrain slightly more complex than Moon's soil, Mars surface can be divided into five groups: highland rock, lowland rock, volcanic regions, channel systems and polar regions. In the Northern Hemisphere, the elevation ranges between -1 to -3 km and is flat, but in counterpart, the south hemisphere is mountainous with elevation of around 4 km. This planet has an average gravity acceleration of 3.72 m^2/s [19]. The daily temperatures range from -58 °C at the equator to -123 °C at its poles, although in the equator the temperature varies between -123 °C at nighttime and 17 °C at noon, but the soil remains at -58 °C. Features like water-cut channels can be observed on Mars's surface. Martian crust thickness varies between 40 km in the Northern Hemisphere and 70 km in the Southern Hemisphere and has the biggest shield volcano in solar system called Olympus Mons with 22 km height. Mars has very indicators of water, such as the water-cut channels and there is evidence of ice below the surface at a depth of around 1 to 2 m at latitudes over 50° that could flood the planet over 500 m. Additionally, the Viking mission conducted an experiment where soil samples were heated to 500 °C to release water, indicating a 0.2 % water in all the regolith. Rocks in Mars are majority basaltic (predominant in the Southern Hemisphere) and andesitic (predominant in the Northern Hemisphere) enriched in oxides and sulphides and the predominant silicate minerals are olivine, plagioclase feldspars, pyroxenes, and quartz. Mars also has dust, but on this planet there are seasonal dust storms which can lead to problems in the Martian expeditions and the atmosphere composition is 2.70 % nitrogen, 0.100 % oxygen, 1.59 % argon, 95.5 % carbon dioxide and 0,1 % carbon monoxide [16], [20].

2.5.5. Materials

For a successful mission, it is essential to select materials in accordance with the conditions under which the rover will be operating. The aspects to have in mind while selecting materials are: thermal properties, physical properties, cost and environmental aspects referred in 2.5.4.

Regarding thermal and physical properties, Carbon fibres have a modulus of 100 GPa for low modulus, over 100 GPa for intermediate, over 300 GPa for high modulus and over 500 GPa for ultra-high modulus. It also has a high strength of over 4 GPa, a density ranging around 1.75 to 2 g/cm^3 and a shear modulus between 10 and 15 GPa. Possesses a low expansion by heat, high chemical resistance and electrical conductivity ranging between 10^4 to 10^5 S/m for PAN-based carbon fibres and between 10^5 to 10^6 S/m for pitch-based carbon fibres [20], [21]. These fibres are usually applied in composites forming CFC (carbon fibre composites) whose properties are determined by the fibres, matrix, and layers as well as fibre orientation. Stainless steel is a metal that presents high corrosion resistance, great conductivity of heat and electricity, durability, easily mouldable and recyclability. It also has one of the lowest weight-to-strength ratio while being a cost-effective option. In spacecraft applications, the stainless-steel grade 316 is the most common option, with a thermal conductivity of 16.3 W/m.K, a melting point between 1370 and 1400 °C, tensile strength of 480 MPa and a Young's modulus of 190 GPa. Aluminium, with a density of 2.7 g/cm^3, is a lightweight metal that is corrosion free due to oxide layers formed on its surface. It is a good conductor of heat and electricity and 100% recyclable. It presents a yield strength of around 35 MPa, shear strength of around 60 MPa, a thermal expansion coefficient of 23.2 and a melting point of around 950 °C, bearing in mind that these properties may vary depending on the type of alloys. In aerospace industry, the aluminium alloy AA6061 is the most representative option, with a melting point of 600 °C and thermal conductivity of 150 W/m.K. Titanium is one of the hardest metals of all and, with a density of 4.54 g/cm^3 , is around 70% heavier than aluminium but with double the strength. This material has a melting point of 1668 °C, a boiling point of 3287 °C, a tensile strength of around 240 MPa and a yield strength of around 240 MPa. It is a poor conductor of electricity and heat and is highly resistant to corrosion. In its purest form, titanium presents a 120 GPa Young’s modulus. The purest grade of titanium is Ti-10V-2Fe-3Al with the greatest yield strength of 1260 MPa compared to all the titanium alloys [20].

Taking to account cost aspects, carbon fibres are used to reinforce structural parts nowadays, but aluminium still being preferably used over carbon fibres. Stainless steel was used in early rovers but has lately been substituted by aluminium, although steel is cheaper. Being the most abundant element and easily extracted, aluminium became a standard option. It began to be utilized in rovers because of a shortage of steel. Titanium is being used on rover legs, although NASA has concerns about titanium’s capabilities of withstanding Martian conditions [20].

2.5.6. Perseverance rover

Perseverance (Figure 7) is the fifth NASA rover sent to Mars, all built by Jet Propulsion Laboratory and was developed from the Curiosity. It was launched from Cape Canaveral, Florida, on July 30, 2020, and still operates today. Perseverance was launched from the Ingenuity Mars Helicopter with the goal of performing a technology demonstration [22].

This rover is the biggest and heaviest ever sent by NASA, weighting 1025 kg, and being about 3 m long, and having a width of 2.7 m and a height of 2.2 m. Compared with its predecessor, Curiosity, Perseverance is 3 cm longer and 126 kg heavier. Similar to Curiosity, this rover has a robotic arm that extends for 2 m equipped with a rotating turret weighing 45 kg and attached to it has a rock drill, science instruments and camera [22].

In relation to the mobility system, NASA opted to maintain the same design as Curiosity, using a six-wheel rocker-bogie design that helps to maintain constant weight in each wheel and reduce the tilt. The wheels are from lightweight aluminium alloy, machined from a rigid block. When compared to Curiosity, its wheels are narrower, but with higher diameter, and the treads differ too because the pointed chevron pattern treads used in Curiosity made it more suitable for wheel damage. So, in order to minimize this problem, an almost straight pattern tread with a small curve was chosen and the number of treads was doubled passing from 24 to 48 [22].

The rover has two main computers, one always active and the other serving as a backup, both being radiation-hardened RAD750 computers. Another RAD750 computer is present in Perseverance, which is equipped with a special card in order to analyse images that, in the process of landing, compare with an onboard map. This determines the position of the rover in relation to the ground, after that being reprogrammed to analyse images of Mars, so the rover can effectively navigate. [22].

The sample caching system of perseverance is made of three components that, working together, will be able to collect samples of rock in sample tubes, leaving them for recovery to Earth in a future mission. The robotic arm equipped with its drill and turret will be placed close to interesting geological features that, after the decision of the Perseverance science team, will obtain a cylindrical sample 13 mm in diameter and 60 mm long. This sample will weigh around 10 to 15 g, and the adaptative caching assembly, consisting of a 0.5 m long sample handling arm, sample tube assemblies, tube seals, and processing stations, will proceed to measure and take images of the sample, leaving it when reaches a location prompted for it [22].

Figure 7 - Perseverance rover

3. Meshless Methods

Meshless methods emerge as an alternative to the commonly used FEM. They employ an unstructured nodal set to discretize the solid domain and establish nodal connectivity through the influence domain concept [23]. Thus, they differ from the FEM in domain discretization, numeric integration, shape functions and equation system [24].

3.1. Bibliographical review

As stated by Belinha [24] and Patel [25], the Smooth Particle Hydrodynamics (SPH) was the first meshless method, presented by Gingold in 1977 [26] and was developed for numerical simulation of astrophysical problems without boundaries. In 1992, Nayroles et al. [27] presented the Diffuse Element Method (DEM) in which moving least square (MLS) approximants are applied, becoming the first method to use MLS [24]. Belytschko added to DEM the incorporation of a background integration mesh based on the Gauss–Legendre quadrature scheme, thus extending DEM applicability to elasticity problems [28]. From the DEM, Belytschko formulated the Element Free Galerkin Method (EFGM) by bringing together DEM and Lagrange multipliers to enforce boundary conditions. Later, SPH originated the Reproducing Kernel Particle Method (RKPM) [29] that, as well as the Meshless Local Petrov–Galerkin (MLPG), use approximation shape functions and higher nodal connectivity in order to give more accurate solutions and smoother variable fields. Regarding the disadvantages of approximation meshless methods, they do not take into account the delta Kronecker property and require a larger system of equations, which results in higher computational cost. Sukumar et al. [30] presented the Natural Element Method (NEM), the first successful interpolating meshless method. Later, other interpolating meshless methods emerged like the Point Interpolation Method (PIM) [31], the Radial Point Interpolation Method (RPIM) [32], the Meshless Finite Element Method (MFEM) [33], and the Natural Radial Element Method (NREM) [34]. By combining NEM with RPIM, Dinis et al. [35] developed the Natural Neighbour Radial Point Interpolation Method (NNRPIM). This method is able to autonomously calculate the position and weight of the background integration points and enforce the nodal connectivity using only the Cartesian coordinates of the nodes, making it a truly meshless method.

3.2. Radial Point Interpolation Method (RPIM)

Although classified as a meshless method, this method is a non-truly meshless method since the set of integration points is independent of the initial nodal distributions. The great advantage presented by this type of method is that it can easily be added to a generic FEM software, using FEM's meshes as background integration cells [23]. The nodal connectivity is established by the influence domain, then shape functions are constructed, making it possible to approximate/interpolate the variable field at an integration point $\boldsymbol{x}_I$ with Equation (1),

$$u(\boldsymbol{x}_I) = \sum_{i=1}^{n} \varphi_i(\boldsymbol{x}_I) \cdot u(\boldsymbol{x}_i) = \boldsymbol{\phi}(\boldsymbol{x}_I)^T \cdot \boldsymbol{u}_s = \{\varphi_1(\boldsymbol{x}_I), \varphi_2(\boldsymbol{x}_I), \dots, \varphi_n(\boldsymbol{x}_I)\} \cdot \begin{Bmatrix} u(\boldsymbol{x}_1) \\ u(\boldsymbol{x}_2) \\ \dots \\ u(\boldsymbol{x}_n) \end{Bmatrix} \quad (\ 1)$$

where $\boldsymbol{x}_I$ is the integration point, n the number of nodes within the influence domain of the integration point $\boldsymbol{x}_I$, $\boldsymbol{u}_s$ is a vector that contains the field variable components of each node $\boldsymbol{x}_i$ inside the influence domain of $\boldsymbol{x}_I$, and $\varphi_i(\boldsymbol{x}_I)$ is the i$^{\text{th}}$ component of the shape function constructed for $\boldsymbol{x}_I$ [23], [36].

3.2.1. Nodal connectivity in RPIM

RPIM uses the overlap of the influence-domain of each node to establish the nodal connectivity, and the influence-domains are found by searching enough nodes inside a fixed area if the problem is 2D or a fixed volume for the 3D problem. This approach benefits from its simplicity, but the size or shape variation of these influence-domains along the problem domain can lead to an inaccurate final solution, and also all the influence-domains must contain approximately the same number of nodes (suggested being between 9 and 16 nodes) in order to have balanced influence-domains. A dimension d is applied to the influence domains following the equation:

$$d = k \times h \quad 2)$$

where h is the average nodal spacing in the surroundings of $\boldsymbol{x}_i$ and k a dimensionless parameter with values between 1.5 and 2.5 [24].

For 2D problems, there are generally two types of fixed size domains (fixed rectangular influence-domain and fixed circular influence-domain) and a variable size domain (flexible circular influence-domain) that as the advantage of having the same number of nodes in every influence-domain as shown in Figure 8.

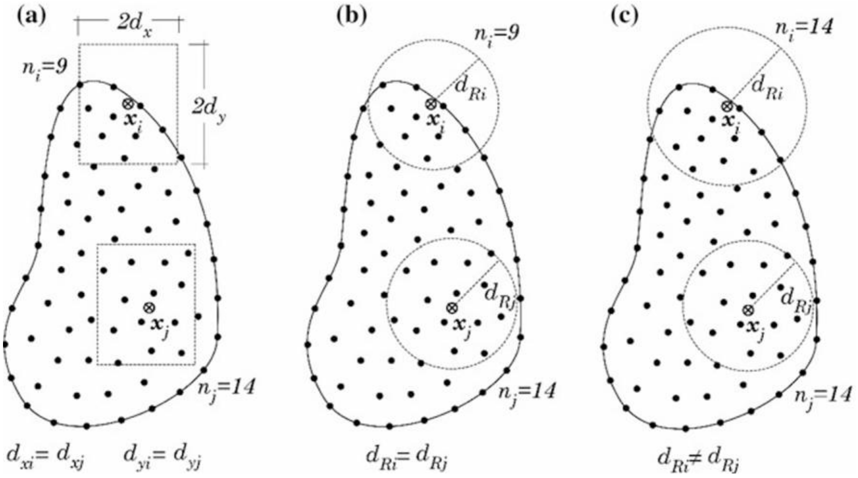

Figure 8 - a) Fixed rectangular influence-domain b) Fixed circular influence-domain c) Flexible circular influence-domain [24]

3.2.2. Numerical Integration in RPIM

To create the background integration points this method relies on a background mesh that divides the problem domain in regular integration cells that will be transformed into an isoparametric square in which the integration points are included following the Gauss–Legendre integration scheme, as shown in Figure 9 [36].

After completed this process, it becomes possible to integrate a function $f(x,y)$, defined inside a quadrilateral domain Ω_h,using a Gauss–Legendre integration scheme with 2×2=4 integration points:

$$F = \int_{\Omega_h} f(x,y)\, d\Omega_h = \sum_{I=1}^{4} f(x_I, y_I) \cdot \widehat{\omega}_I \qquad (3)$$

where $\widehat{\omega}_I$ is the Cartesian integration weight of each integration point. Repeating this process for each integration cell it is obtained a background integration mesh of n_Q integration points and since the background integration cell is coincident with the problem's domain, it is possible to calculate the area of the problem domain with [36]:

$$A_\Omega = \sum_{I=1}^{n_Q} \widehat{\omega}_I \qquad (4)$$

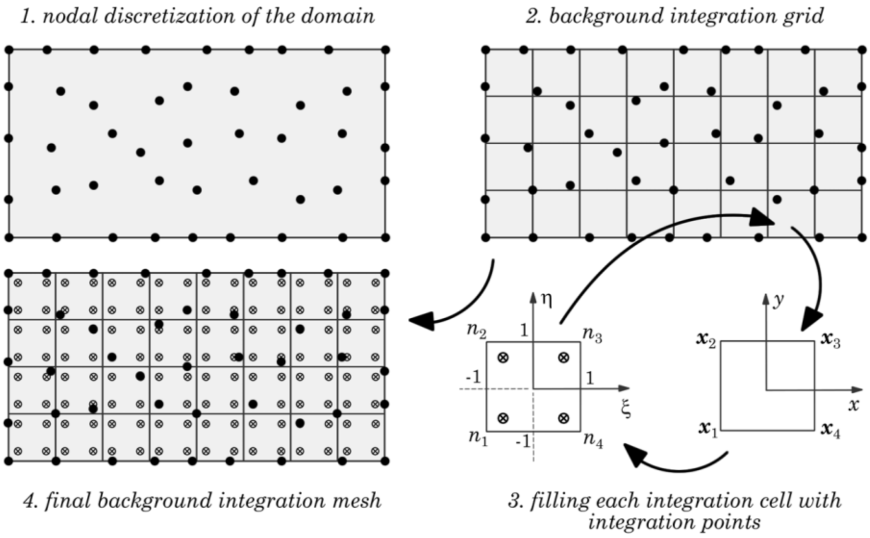

1. nodal discretization of the domain

2. background integration grid

3. filling each integration cell with integration points

4. final background integration mesh

Figure 9 - Integration scheme for RPIM using a rectangular domain and a regular background [36]

3.3. Natural Neighbour Radial Point Interpolation Method (NNRPIM)

This method is a truly meshless method, which means that, using only the nodal distribution information, it can autonomously construct all the requirements to solve the problem. NNRPIM establish the nodal connectivity via the influence cell concept and, using the shape functions, it is possible to approximate/interpolate the variable field at an integration point x_1 with equation (1).

3.3.1. Nodal connectivity in NNRPIM

This method uses a natural neighbour concept that requires the construction of the Voronoï diagram as in Figure 10 of the problem's nodal discretisation. Assuming a 2D domain, $\Omega \in \mathbb{R}^2$ discretised with N nodes, $\boldsymbol{X} = \{x_1, x_2, \dots, x_N\} \in \mathbb{R}^2$, the Voronoï diagram, V, of $\boldsymbol{X}$ is formed by subsections V_i closed and convex, defined in (and defining) the same sub-space $\Omega \in \mathbb{R}^2$ and each node $\boldsymbol{x}_i$ possesses its own cell V_i where all points in the cell are closer to $\boldsymbol{x}_i$ than any other given node $\boldsymbol{x}_j \in X$. The Voronoï diagram of $\boldsymbol{X}$, $\boldsymbol{V} = \{V_1, V_2, \dots, V_N\}$ and the Voronoï cells V_i do not overlap neither leave gaps between each other so they verify: $\Omega = \sum_{i=1}^{N} V_i \therefore \boldsymbol{V} = \Omega$ [23].

3.3.2. Numerical Integration in NNRPIM

In order to create the integration points, each quadrilateral of a given Voronoï cell V_i is transformed into a unit isoparametric square where the distribution of integration points respect the Gauss–Legendre integration scheme exemplified in Figure 10 [23].

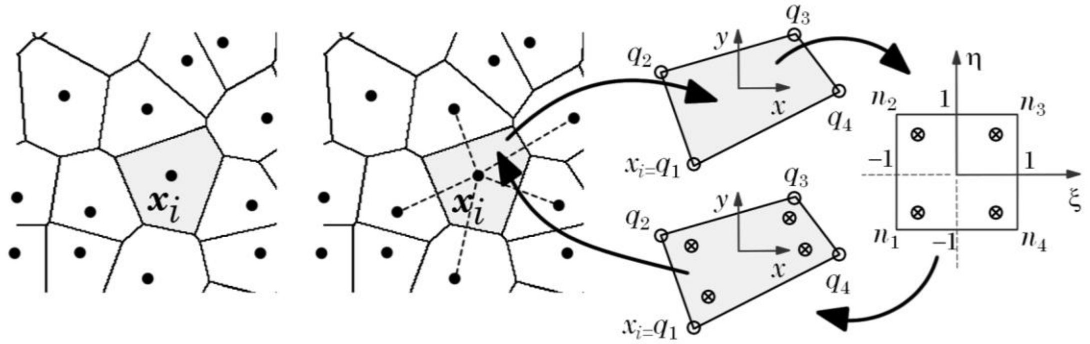

Figure 10 - Construction of the background set of integration points based on the Voronoï diagram [23]

To integrate an assumed function $f(x,y)$, located inside a quadrilateral sub-area domain, Ω_s, a Gauss–Legendre integration scheme with 2×2=4 integration points is used

$$F = \int_{\Omega_s} f(x,y)\, d\Omega_s = \sum_{I=1}^{4} f(x_I, y_I) \cdot \hat{\omega}_I \tag{5}$$

Where $\hat{\omega}_I$ is the cartesian integration weight of each integration point. Repeating this process for each quadrilateral sub-area and then to each Voronoï cell it is obtained in the end a background set of n_Q integration points that allow to integrate any function in the domain Ω [23].

3.4. Shape functions

The construction of the shape functions for RPIM and NNRPIM follows the same process using the radial point interpolating technique. In this technique is assumed a 2D domain, $\Omega \in \mathbb{R}^2$, where a field function $u(\boldsymbol{x})$ is discretised with N nodes, $\boldsymbol{X} = \{x_1, x_2, \dots, x_N\} \in \mathbb{R}^2$, the interpolation value $u(\boldsymbol{x}_I)$ of an given integration point, $\boldsymbol{x}_I \in \mathbb{R}^2 \wedge \boldsymbol{x}_I \in \boldsymbol{X}$, can be calculated by the following equation .

$$u(\boldsymbol{x}_I) = \{\boldsymbol{r}(\boldsymbol{x}_I)^T, \boldsymbol{p}(\boldsymbol{x}_I)^T\} \begin{Bmatrix} \boldsymbol{a} \\ \boldsymbol{b} \end{Bmatrix} \tag{6}$$

$\boldsymbol{r}(\boldsymbol{x}_I) = \{r_1(\boldsymbol{x}_I), r_2(\boldsymbol{x}_I), \dots, r_n(\boldsymbol{x}_I)\}^T$ is a Radial Basis Function (RBF), $\boldsymbol{p}(\boldsymbol{x}_I) = \{p_1(\boldsymbol{x}_I), p_2(\boldsymbol{x}_I), \dots, p_m(\boldsymbol{x}_I)\}^T$ is a polynomial basis function and the vectors of the non-constant coefficients of $\boldsymbol{r}(\boldsymbol{x}_I)$ and $\boldsymbol{p}(\boldsymbol{x}_I)$ defined as, $\boldsymbol{a}(\boldsymbol{x}_I) = \{a_1(\boldsymbol{x}_I), a_2(\boldsymbol{x}_I), \dots, a_n(\boldsymbol{x}_I)\}^T$ and $\boldsymbol{b}(\boldsymbol{x}_I) = \{b_1(\boldsymbol{x}_I), b_2(\boldsymbol{x}_I), \dots, b_m(\boldsymbol{x}_I)\}^T$ [23].

Following a Multiquadric Radial Basis Function (MQ-RBF) of Hardy,

$$r_j(\boldsymbol{x}_i) = r_{ij} = (d_{ij}^2 + (\hat{\omega}_I \cdot c)^2)^p = \left(\left(\sqrt{(x_j - x_i)^2 + \left(y_j - y_i\right)^2}\right)^2 + (\hat{\omega}_I \cdot c)^2\right)^p \tag{7}$$

With c and p being two constants of the MQ-RBF with recommended values close but different from zero for c and close but different from one for p (generally $c = 10^{-4}$ and $p = 1 - 10^{-4}$) [23]. In order to ensure a unique solution, there is the need to add the following equation:

$$\sum_{i=1}^{n} p_j(\boldsymbol{x}_i)a_i(\boldsymbol{x}_i) = 0 \tag{8}$$

Where $j = \{1,2,\dots,m\}$. Joining together the Equations (6) and (8)a new equation matrix is obtained:

$$\begin{bmatrix} \boldsymbol{R} & \boldsymbol{P} \\ \boldsymbol{P}^T & 0 \end{bmatrix} \begin{Bmatrix} \boldsymbol{a} \\ \boldsymbol{b} \end{Bmatrix} = \boldsymbol{G} \begin{Bmatrix} \boldsymbol{a} \\ \boldsymbol{b} \end{Bmatrix} = \begin{Bmatrix} \boldsymbol{u}_s \\ 0 \end{Bmatrix} \tag{9}$$

Where $\boldsymbol{u}_s$ is the vector of nodal parameters:

$$\boldsymbol{u}_s = \{u_1, u_2, \dots, u_n\}^T \tag{10}$$

$\boldsymbol{R}$ is the RBF matrix:

$$\boldsymbol{R} = \begin{bmatrix} r_{11} & r_{12} & \cdots & r_{1n} \\ r_{21} & r_{22} & \cdots & r_{2n} \\ \vdots & \vdots & \ddots & \vdots \\ r_{n1} & r_{n2} & \cdots & r_{nn} \end{bmatrix} \tag{11}$$

$\boldsymbol{P}$ is the polynomial basis matrix:

$$\boldsymbol{P} = \begin{bmatrix} p_1(\boldsymbol{x}_1) & p_2(\boldsymbol{x}_1) & \cdots & p_n(\boldsymbol{x}_1) \\ p_1(\boldsymbol{x}_2) & p_2(\boldsymbol{x}_2) & \cdots & p_n(\boldsymbol{x}_2) \\ \vdots & \vdots & \ddots & \vdots \\ p_1(\boldsymbol{x}_n) & p_2(\boldsymbol{x}_n) & \cdots & p_n(\boldsymbol{x}_n) \end{bmatrix} \tag{12}$$

From equation (9) it is obtained:

$$\begin{Bmatrix} \boldsymbol{a} \\ \boldsymbol{b} \end{Bmatrix} = \boldsymbol{G}^{-1} \cdot \begin{Bmatrix} \boldsymbol{u}_s \\ 0 \end{Bmatrix} \tag{13}$$

That when inserted in equation (6) the interpolation at $\boldsymbol{x}_I$ can be defined as:

$$u(\boldsymbol{x}_I) = \{\boldsymbol{r}(\boldsymbol{x}_I)^T, \boldsymbol{p}(\boldsymbol{x}_I)^T\}\boldsymbol{G}^{-1} \cdot \begin{Bmatrix} \boldsymbol{u}_s \\ 0 \end{Bmatrix} = \{\boldsymbol{\phi}(\boldsymbol{x}_I), \boldsymbol{\Psi}(\boldsymbol{x}_I)\} \cdot \begin{Bmatrix} \boldsymbol{u}_s \\ 0 \end{Bmatrix} \tag{14}$$

Where $\phi(\boldsymbol{x}_I)$ is the interpolation function of $\boldsymbol{x}_I$:

$$\{\boldsymbol{\phi}(\boldsymbol{x}_I), \boldsymbol{\Psi}(\boldsymbol{x}_I)\} = \{\boldsymbol{r}(\boldsymbol{x}_I)^T, \boldsymbol{p}(\boldsymbol{x}_I)^T\}\boldsymbol{G}^{-1} = \{\phi_1(\boldsymbol{x}_I), \dots, \phi_n(\boldsymbol{x}_I), \Psi_1(\boldsymbol{x}_I), \dots,, \Psi_m(\boldsymbol{x}_I)\} \tag{15}$$

The integro-differential equations ruling elasticity require the calculation of the partial derivatives of $\boldsymbol{\phi}(\boldsymbol{x}_I)$, so if a general direction ζ is assumed:

$$\boldsymbol{\phi}_\zeta(\boldsymbol{x}_I) = \left\{\boldsymbol{r}(\boldsymbol{x}_I)_\zeta^T, \boldsymbol{p}(\boldsymbol{x}_I)_\zeta^T\right\}\boldsymbol{G}^{-1} \tag{16}$$

3.5. System of equations

Like the shape functions, the system of equations is defined in the same way for the RPIM and the NNRPIM. So, considering a solid domain Ω, bounded by a surface boundary Γ that contain natural boundaries Γ_t and essential boundaries Γ_u, the solid domain is constricted at Γ_u and suffer a body force $\boldsymbol{b}$ and forces $\bar{\boldsymbol{t}}$ on Γ_t. Defining that work of external forces equals work of internal forces $W_{int} = W_{ext}$, it is obtained [36]:

$$\int_{\Omega} \delta\boldsymbol{\varepsilon}^T \cdot \boldsymbol{\sigma}\, d\Omega = \int_{\Omega} \delta\boldsymbol{u}(\boldsymbol{x}_I)^T \cdot \boldsymbol{b}\ d\Omega + \int_{\Gamma_t} \delta\boldsymbol{u}(\boldsymbol{x}_I)^T \cdot \bar{\boldsymbol{t}}\ d\Gamma \tag{17}$$

Where $\boldsymbol{\varepsilon}$ is the deformation tensor and $\boldsymbol{\sigma}$ is the strain tensor

The 2D problems, Equation (17) requires two displacement components $\{u, v\}$, that can be defined as:

$$\boldsymbol{u}(\boldsymbol{x}_I) = \begin{Bmatrix} u(\boldsymbol{x}_I) \\ v(\boldsymbol{x}_I) \end{Bmatrix} = \boldsymbol{H}(\boldsymbol{x}_I) \cdot \boldsymbol{u} = \begin{bmatrix} \phi_1(\boldsymbol{x}_I) & 0 & \cdots & \phi_n(\boldsymbol{x}_I) & 0 \\ 0 & \phi_1(\boldsymbol{x}_I) & \cdots & 0 & \phi_n(\boldsymbol{x}_I) \end{bmatrix} \cdot \begin{Bmatrix} u_1 \\ v_1 \\ \vdots \\ u_n \\ v_n \end{Bmatrix} \tag{18}$$

Which leads to the representation of the deformation vector:

$$\boldsymbol{\varepsilon}(x_I) = \boldsymbol{L} \cdot \boldsymbol{u}(\boldsymbol{x}_I) = \begin{bmatrix} \frac{\partial}{\partial x} & 0 \\ 0 & \frac{\partial}{\partial y} \\ \frac{\partial}{\partial y} & \frac{\partial}{\partial x} \end{bmatrix} \cdot \boldsymbol{\phi}(\boldsymbol{x}_I) \cdot \boldsymbol{u} = \boldsymbol{B}(\boldsymbol{x}_I) \cdot \begin{Bmatrix} u_1 \\ v_1 \\ \vdots \\ u_n \\ v_n \end{Bmatrix} \tag{19}$$

Being deformation matrix $\boldsymbol{B}(\boldsymbol{x}_I)$ defined as:

$$\boldsymbol{B}(\boldsymbol{x}_I) = \begin{bmatrix} \frac{\partial\phi_1(\boldsymbol{x}_I)}{\partial x} & 0 & \cdots & \frac{\partial\phi_n(\boldsymbol{x}_I)}{\partial x} & 0 \\ 0 & \frac{\partial\phi_1(\boldsymbol{x}_I)}{\partial y} & \cdots & 0 & \frac{\partial\phi_n(\boldsymbol{x}_I)}{\partial y} \\ \frac{\partial\phi_1(\boldsymbol{x}_I)}{\partial y} & \frac{\partial\phi_1(\boldsymbol{x}_I)}{\partial x} & \cdots & \frac{\partial\phi_n(\boldsymbol{x}_I)}{\partial y} & \frac{\partial\phi_n(\boldsymbol{x}_I)}{\partial x} \end{bmatrix} \tag{20}$$

Assuming Hooke's law, the stress can be calculated at the integration point $\boldsymbol{x}_I$:

$$\boldsymbol{\sigma}(\boldsymbol{x}_I) = \boldsymbol{c}(\boldsymbol{x}_I) \cdot \boldsymbol{\varepsilon}(x_I) = \boldsymbol{c}(\boldsymbol{x}_I) \cdot \boldsymbol{B}(\boldsymbol{x}_I) \cdot \boldsymbol{u} \tag{21}$$

In a 2D problems, if plane stress is considered, material constitutive matrix $\boldsymbol{c}(\boldsymbol{x}_I)$ is defined as:

$$\boldsymbol{c} = \frac{E_2}{1 - \alpha_1 \cdot v_{21}^2} \begin{bmatrix} \alpha_1 & \alpha_1 \cdot v_{21} & 0 \\ \alpha_1 \cdot v_{21} & 1 & 0 \\ 0 & 0 & \alpha_2 \cdot (1 - \alpha_1 \cdot v_{21}^2) \end{bmatrix} \tag{22}$$

If plane strain is considered, then:

$$\boldsymbol{c} = \frac{E_2}{\alpha_3 \cdot \alpha_4} \begin{bmatrix} \alpha_1 \cdot (1 - \alpha_1 \cdot \upsilon_{21}^2) & \alpha_1 \cdot \upsilon_{21} \cdot \alpha_3 & 0 \\ \alpha_1 \cdot \upsilon_{21} \cdot \alpha_3 & 1 - \upsilon_{12}^2 & 0 \\ 0 & 0 & \alpha_2 \cdot \alpha_3 \cdot \alpha_4 \end{bmatrix} \tag{23}$$

With $\alpha_1 = E_1/E_2$, $\alpha_2 = G_{12}/E_2$, $\alpha_3 = 1 + \upsilon_{12}$ and $\alpha_4 = 1 - \upsilon_{12} - 2 \cdot \alpha_1 \cdot \upsilon_{21}^2$ where E_i is the Young's modulus in material direction i, G_{ij} the elastic shear modulus in the plane O_{ij} and υ_{ij} the Poisson's coefficient in the plane O_{ij}.

With the manipulation of the equation (17) replacing the stress and strain vectors it is obtained:

$$\begin{aligned} &\int_{\Omega} \delta(\boldsymbol{B}(\boldsymbol{x}_I) \cdot \boldsymbol{u})^T \cdot (\boldsymbol{c}(\boldsymbol{x}_I) \cdot \boldsymbol{B}(\boldsymbol{x}_I) \cdot \boldsymbol{u})\, d\Omega \\ &\qquad = \int_{\Omega} \delta(\boldsymbol{H}(\boldsymbol{x}_I) \cdot \boldsymbol{u})^T \cdot \boldsymbol{b}\, d\Omega + \int_{\Gamma_t} \delta(\boldsymbol{H}(\boldsymbol{x}_I) \cdot \boldsymbol{u})^T \cdot \bar{\boldsymbol{t}}\, d\,\Gamma \end{aligned} \tag{24}$$

That, considering the small strains $\delta\mathbf{B}(\boldsymbol{x}_I) = 0$ and $\delta\boldsymbol{H}(\boldsymbol{x}_I) = 0$, can be simplified to:

$$\begin{aligned} &\int_{\Omega} \delta\boldsymbol{u}^T \cdot \boldsymbol{B}(\boldsymbol{x}_I)^T \cdot \boldsymbol{c}(\boldsymbol{x}_I) \cdot \boldsymbol{B}(\boldsymbol{x}_I) \cdot \boldsymbol{u}\, d\Omega \\ &\qquad = \int_{\Omega} \delta\boldsymbol{u}^{\boldsymbol{T}} \cdot \boldsymbol{H}(\boldsymbol{x}_I)^T \cdot \boldsymbol{b}\, d\Omega + \int_{\Gamma_t} \delta\boldsymbol{u}^{\boldsymbol{T}} \cdot \boldsymbol{H}(\boldsymbol{x}_I)^T \cdot \bar{\boldsymbol{t}}\, d\Gamma \end{aligned} \tag{25}$$

$$\begin{aligned} &\delta\boldsymbol{u}^{\boldsymbol{T}} \int_{\Omega} \boldsymbol{B}(\boldsymbol{x}_I)^T \cdot \boldsymbol{c}(\boldsymbol{x}_I) \cdot \boldsymbol{B}(\boldsymbol{x}_I) \cdot d\Omega \cdot \boldsymbol{u} \\ &\qquad = \delta\boldsymbol{u}^{\boldsymbol{T}} \int_{\Omega} \boldsymbol{H}(\boldsymbol{x}_I)^T \cdot \boldsymbol{b} \cdot d\Omega + \delta\boldsymbol{u}^{\boldsymbol{T}} \int_{\Gamma_t} \boldsymbol{H}(\boldsymbol{x}_I)^T \cdot \bar{\boldsymbol{t}} \cdot d\Gamma \end{aligned} \tag{26}$$

Making it possible to define the final system of equations of elasticity:

$$\boldsymbol{K} \cdot \boldsymbol{u} = \boldsymbol{f}_b + \boldsymbol{f}_t \tag{27}$$

That is further manipulated to the global displacement field of the problem:

$$\boldsymbol{u} = \boldsymbol{K}^{-\boldsymbol{1}} \cdot (\boldsymbol{f}_b + \boldsymbol{f}_t) \tag{28}$$

Where global stiffness matrix $\boldsymbol{K}$ in its discretised form is defined as:

$$\boldsymbol{K} = \int_{\Omega} \boldsymbol{B}(\boldsymbol{x}_I)^T \cdot \boldsymbol{c}(\boldsymbol{x}_I) \cdot \boldsymbol{B}(\boldsymbol{x}_I)\, d\Omega = \sum_{I=1}^{N_Q} \boldsymbol{B}(\boldsymbol{x}_I)^T \cdot \boldsymbol{c}(\boldsymbol{x}_I) \cdot \boldsymbol{B}(\boldsymbol{x}_I) \cdot \widehat{\omega}_I \cdot h(\boldsymbol{x}_I) \tag{29}$$

And the external force vector $\boldsymbol{f}_{\mathrm{t}}$ and the global body vector $\boldsymbol{f}_{\mathrm{b}}$:

$$\boldsymbol{f}_{\mathrm{t}} = \int_{\Gamma_t} \mathbf{H}(\boldsymbol{x}_I)^T \cdot \bar{\mathbf{t}} \cdot d\Gamma = \sum_{J=1}^{N_Q} \mathbf{H}(\boldsymbol{x}_J)^T \cdot \bar{\mathbf{t}} \cdot \widehat{\omega}_J \tag{30}$$

$$\boldsymbol{f}_{\mathrm{b}} = \int_{\Omega} \mathbf{H}(\boldsymbol{x}_I)^T \cdot \mathbf{b} \cdot d\Omega = \sum_{I=1}^{N_Q} \mathbf{H}(\boldsymbol{x}_I)^T \cdot \mathbf{b} \cdot \widehat{\omega}_I \cdot h(\boldsymbol{x}_I) \tag{31}$$

where $h(\boldsymbol{x}_I)$ is the thickness of the 2D solid at the location of the integration point $\boldsymbol{x}_I$.

Since NNRPIM and RPIM are interpolating techniques, the imposition of essential and natural boundary conditions can be implemented using the direct imposition method or penalty methods [23], [36].

4. Bio-Inspired Remodelling Algorithm (BIRA)

The topology optimization algorithm used in this work is inspired by the bone tissue remodelling. Bone tissue is usually composed of two different structures: the cortical bone, more compact, presenting a higher density than the other structure, and the trabecular bone. In the remodelling procedure, a mechanical stimulus will trigger the bone tissue remodelling process. Belinha et. al. [37] uses the following function defining the Young's modulus in the bone's axial direction:

$$E_{axial} = 10^3 \times \begin{cases} 0.7216 \cdot \rho_{app} + 0.8059 \cdot \rho_{app}^2 \Leftarrow \rho_{app} \leq 1.3 \text{ g/cm}^3 \\ -177 + 386.1\rho_{app} - 279.8\rho_{app}^2 + 68.36\rho_{app}^3 \Leftarrow \rho_{app} > 1.3 \text{ g/cm}^3 \end{cases} \quad (32)$$

where ρ_{app} is the bone tissue apparent density.

For the Young's modulus in the transversal direction, the function takes the following form:

$$E_{trans} = 10^3 \times \left(2.004 \cdot \rho_{app}^2 - 0.144 \cdot \rho_{app}^3\right) \quad (33)$$

Also, the ultimate compression stress σ_i^c in both axial and transversal directions can be expressed as:

$$\sigma_{axial}^c = 26.80 \cdot \rho_{app}^2 + 20.35 \cdot \rho_{app}^3 \quad (34)$$

$$\sigma_{trans}^c = 25.010 \cdot \rho_{app}^2 + 1.247 \cdot \rho_{app}^3 \quad (35)$$

Equations (32), (33), (34) and (35) are expressed in MPa with ρ_{app} expressed in g/cm^3.

4.1. Remodelling criteria

The non-linear function $\rho_{app}\ (\boldsymbol{x}, t) : \mathbb{R}^{d+1} \longmapsto \mathbb{R}$ is used in this work to describe the evolution of the bone tissue apparent density and this temporal–spatial functional can be minimized with respect to fictious time,

$$\frac{\partial \rho_{app}\ (\boldsymbol{x}, t)}{\partial t} \cong \frac{\Delta \rho_{app}\ (\boldsymbol{x}, t)}{\Delta t} = \frac{\left(\rho_{app}^{model}\right)_{j+1} - \left(\rho_{app}^{model}\right)_j}{t_{j+1} - t_j} = 0 \quad (36)$$

For a fictional time $t_j \in \mathbb{R}$ with $j \in \mathbb{N}$, the medium apparent density for the complete model domain can be expressed as,

$$\left(\rho_{app}^{model}\right)_{t_j} = Q^{-1}\sum_{i=1}^{Q}\left(\rho_{app}\right)_i \tag{37}$$

Where the problem domain is domain is discretized in *N* nodes: $\boldsymbol{X} = \{\boldsymbol{x}_1, \boldsymbol{x}_2, \dots, \boldsymbol{x}_N\} \in \Omega$, the Q interest points $\boldsymbol{Q} = \{\boldsymbol{x}_1, \boldsymbol{x}_2, \dots, \boldsymbol{x}_Q\} \in \Omega$,being $\boldsymbol{x}_i \in \mathbb{R}^d$ and $\boldsymbol{Q} \cap \boldsymbol{X} = \emptyset$. Also, $\left(\rho_{app}\right)_I$ is the infinitesimal apparent density on interest point $\boldsymbol{x}_i$ which is defined by the function $\rho_1 = g(\sigma_1)$,

$$g(\sigma_1) = \min\left(\{\sigma_1^{-1}(\rho_1), \sigma_2^{-1}(\rho_1), \sigma_3^{-1}(\rho_1)\}\right) \tag{38}$$

were σ_k with $k = \{1,2,3\}$, are the three principal stresses obtained at the interest point $\boldsymbol{x}_i$, and $\sigma_k^{-1}(\rho_1)$ are the inverse functions of $\sigma_k(\rho_1)$, described in the equations (34) and (35). This makes it possible to obtain the following expressions for the principal stress σ_k,

$$\sigma_1^{-1}(\rho_1) = \sigma_{axial}^{-1}(\rho_1) = \rho_{axial} = 8.14 \times 10^{-4} f_1(\sigma_1) + \frac{253.3}{f_1(\sigma_1)} - 0.439 \tag{39}$$

$$\sigma_k^{-1}(\rho_1) = \sigma_{trans}^{-1}(\rho_1) = \rho_{trans} = 1.34 \times 10^{-3} f_2(\sigma_k) + \frac{3.34\times10^4}{f_2(\sigma_k)} - 0.669 \text{ for } k = \{2,3\} \tag{40}$$

With functions $f_1(\sigma_1)\colon \mathbb{C} \longmapsto \mathbb{R}$ and $f_2(\sigma_k)\colon \mathbb{C} \longmapsto \mathbb{R}$,

$$\begin{aligned} f_1(\sigma_1) = Re\Big(&-1.54 \times 10^8 + 4.47 \times 10^7 \sigma_1 \\ &+ 2.44 \times 10^3 \sqrt{-2.31 \times 10^9 \sigma_1 + 3.35 \times 10^9 \sigma_1^2}\Big) \end{aligned} \tag{41}$$

$$\begin{aligned} f_2(\sigma_k) = Re\Big(&-1.25 \times 10^{11} + 1.68 \times 10^8 \sigma_k \\ &+ 1.49 \times 10^4 \sqrt{-1.88 \times 10^{11} \sigma_k + 1.26 \times 10^8 \sigma_k^2}\Big) \end{aligned} \tag{42}$$

The expressions described in equations (39) and (40) can only be applied to the interest point $\boldsymbol{x}_I$ with the strain energy density value following the expression,

$$U(\boldsymbol{x}_I) \in [U_m, U_m + \alpha \cdot \Delta U[\, \cup \,]U_M - \beta \cdot \Delta U, U_M], \qquad \forall U(\boldsymbol{x}_I) \in \mathbb{R} \tag{43}$$

where the strain energy density (SED) field of the problem domain is defined by $\boldsymbol{U} = \{U(\boldsymbol{x}_1), U(\boldsymbol{x}_2), \dots, U(\boldsymbol{x}_Q)\}$, $U_m = \min(\boldsymbol{U})$, $U_M = \max(\boldsymbol{U})$ and $\Delta U = U_M - U_m$. The growth rate of the apparent density is defined by parameter α and the decrease rate by parameter β.

The local remodelling process ends when is achieved a remodelling equilibrium,

$$\frac{\Delta\rho}{\Delta t} = 0 \vee \left(\rho_{app}^{model}\right)_{t_j} \leq \rho_{app}^{control} \tag{44}$$

4.2. Remodelling algorithm

The remodelling algorithm starts with step zero (*j*=0) where a first trial linear isotropic analysis of the problem is performed in order to obtain the principal directions of the stress field in each integration point. In this step does not happen remodelling of the object but it is determined the local stiffness matrices for each integration point and assembled into global stiffness matrix $\boldsymbol{K}_j$ allowing the iterative remodelling algorithm to initiate.

In order to analyse numerous load cases, $\boldsymbol{f}_j^k$, it is necessary to determinate the displacement field separately from each case k, $\boldsymbol{u}_j^k = \boldsymbol{K}_j^{-1}\boldsymbol{f}_j^k$, obtaining after the strain field, $\boldsymbol{\varepsilon}_j^k$, and the stress field, $\boldsymbol{\sigma}_j^k$ where can be determined the principal stresses, $\boldsymbol{\sigma}(\boldsymbol{n})_j^k$, and principal directions, $\boldsymbol{n}_j^k$. Combined with strain field $\boldsymbol{\varepsilon}_j^k$, the SED field $\boldsymbol{U}_j^k$ can be determined,

$$U(\boldsymbol{x}_1) = \frac{1}{2}\int_{\Omega_1} \boldsymbol{\sigma}(\boldsymbol{x}_1)^T \boldsymbol{\varepsilon}(\boldsymbol{x}_1)\, d\Omega_1 \tag{ 45}$$

The variable fields obtained for each load case are weighted as follows,

$$\{\boldsymbol{u}_j, \boldsymbol{\varepsilon}_j, \boldsymbol{\sigma}_j, \boldsymbol{\sigma}(\boldsymbol{n})_j, \boldsymbol{n}_j, \boldsymbol{U}_j\} = \sum_{k=1}^{1} \frac{m^{(k)}\{\boldsymbol{u}_j, \boldsymbol{\varepsilon}_j, \boldsymbol{\sigma}_j, \boldsymbol{\sigma}(\boldsymbol{n})_j, \boldsymbol{n}_j, \boldsymbol{U}_j\}}{\sum_{s=1}^{l} m^{(s)}} \tag{ 46}$$

Following the conditions on Equation (43) and the weighted SED field $\boldsymbol{U}_j$ it is selected the interest points for the density remodelling process with the other interest points with SED values outside the defined intervals on Equation (43), maintaining their previous density. After selected the interest points, the weighted principal stress of those interest points is used to estimate their individual new apparent density following Equation (38).

The process will continue through iterations until it is achieved a remodelling equilibrium shown in Equation (44).

5. Computational Applications

In this chapter, a review of the research studies regarding the analysis of rover components using either FEM or meshless methods is presented. These studies are grouped according to the component under study in order to make comparisons between them easier.

5.1. Wheel

The wheel is the rover component that is currently undergoing the most study, which indicates its extreme importance in the success of a rover mission, thus its designs are constantly evolving. Some authors propose a self-designed rover wheel architecture consisting of a honeycomb-bullet wheel design - Figure 11 a) [38]. Others suggest the incorporation of a leaf spring so that the wheel can absorb impact - Figure 11 c) [39] and even variable-diameter wheels are proposed - Figure 11 b) [40]. Also, innovative flexible metal for application in wheels are studied for applications in extraterrestrial rovers - Figure 11 e) [41] as well as comparative analyses of different materials for the same wheel design [38]. In this category, all the articles presented range from the year 2020 to the year 2024 and, in their analyses, the authors resort to finite element analyses for the numerical simulations.

Vishnoi et al. [38] show a self-designed wheel architecture with a honeycomb-bullet design and proceed to make a comparative analysis between Aluminium alloy, Structural Steel and Shape Memory alloy (Nitinol) wheels for both conventional and self-designed wheel architectures. In this work the analyses were performed in the ANSYS software using Solid186 element for Solid FEM and the analyses focused on total deformation, shear stress and equivalent stress. The tests were made in order to simulate loading in the normal direction, applying a load of 700 MPa on the upper surface of the model, applying fixed support on the lower part and constraining the translational degrees of freedom. In the end, honeycomb-bullet design showcased the lowest values of maximum total displacement for aluminium alloy (0.011154 mm), structural steel (0.0041129 mm) and nitinol (0.010968 mm) due to a more efficient load distribution in comparison with conventional design. It was also observed a reduction in von Mises equivalent stress in honeycomb-bullet wheel design for all three materials, with aluminium showcasing the lowest value of highest equivalent (0.060006 MPa) stress induced. The honeycomb-bullet wheel design also presents a reduction in shear stress in comparison with the conventional design, being the aluminium self-design wheels the ones with the lowest shear stress-induced (0.26472 MPa).

Zeng et al. [40] presented the design of a variable-diameter wheel in order to solve the contradiction between tractive performance and the limited spacecraft volume. A novel compliant variable-diameter mechanism configuration with helical torsion springs is proposed, which allows the wheel to transform its structure using expansion-retraction motion. The authors developed a pseudo-rigid-body model for the mechanism in order to obtain the load-deflection behaviour and then compared the obtained values with the results of finite element analysis (FEA) simulations, performed using ABAQUS software. The two results showed good agreement, which confirmed the reliability of the design method and the analysis approach for the variable-diameter mechanism. It was concluded that this new compliant variable-diameter mechanism prevents wear, backlash, and lubrication, simplifying assembly and making the mechanism more compact and lightweight when compared with conventional expandable rigid-body mechanisms, thus being useful for variable-diameter wheel designs for the lunar environment. In this way, the authors claim that this mechanism solves the contradiction between tractive performance, and the limited spacecraft volume as was initially requested.

Dalmeida et al. [39] investigated the design and analysis of rover wheels with part of the suspension system included in the wheel (leaf spring). To analyse the leaf spring, and later the wheel, the authors resort to analytical analysis and simulations using for that ANSYS software. For the maximum load applied on the leaf spring (made of Magnesium RZ5 Alloy) of 30 N it is analytically obtained a stress of 126 MPa and a deflection of 1,403 mm, and through simulation a stress of 129.27 N/mm^2 and a deflection of 1.1518 mm. The authors concluded that the maximum load for a structurally safe design is 25 N, from where analytically was obtained a stress of 105 N/mm^2 and a deflection of 1.169 mm, and through ANSYS simulation a stress of 127.73 N/mm^2 and a deflection of 0.9598 mm. After that, the wheel, which is constituted by 12 leaf springs and other components made of Al Alloy and Ti-6Al-4V, is analysed for an external force of 180 N obtained a minimum safety factor of 1.1487, a maximum deflection of 10.225 mm and a maximum equivalent von Mises stress of 171.21 MPa.

Qi et al. [41] proposed an innovative flexible metal wheel consisting of a single rim and twin carcasses. The authors presented the design method and structural details of the wheel and further analysed it resorting to FEM simulations under different loads considering the lunar environment. First, two different vertical loads were simulated, for sheet thickness of 1.3 mm, 1.5 mm, and 1.7 mm, ending up selecting a sheet thickness of 1.5 mm the suitable one. Next, a tangential force and side force were simulated, obtaining maximum stresses of 715.5 MPa and 433.2 MPa, respectively, ensuring that no plastic deformation would occur. The authors also performed impact simulations. From the results, they concluded that plastic deformation occurs on rigid ground but not on soft ground. Following the FEM simulations, testing on the fabricated wheel presented lower deformations than expected through simulation. This type of wheel presents a better option at absorbing impact than the model presented by Dalmeida [39] due to the mechanical simplicity offered by the flexible metal wheel.

Agrahari et. Al [42] presented a micro-rover designed to explore the dormant Martian lava caves, with some components analysed with ANSYS software. Looking only for the wheel - Figure 11 e), the authors presented the process that takes to the final design of the wheel and justified the selection of materials, Aluminium Alloy 7075T7351 for wheel treads and shaft and Titanium (Ti-55) for spokes. For the analyses, two cases were proposed: in the first one, the authors assumed a fixed support at the hub and shaft of the wheel and applied load of 50 N to the wheel thread and Spokes, in the second one, a simulation was performed of the landing, taking into account the gravity of Mars and considering a 1 m drop. The results showcased for the first case a maximum total displacement of 0.11603 mm and a maximum equivalent von Mises stress of 46.759 MPa. In the second case, the maximum total displacement was 1.4995 mm and the maximum equivalent von Mises stress was 183.66 MPa, also obtaining a minimum safety factor of 1.52445 and a maximum number of 2000 cycles.

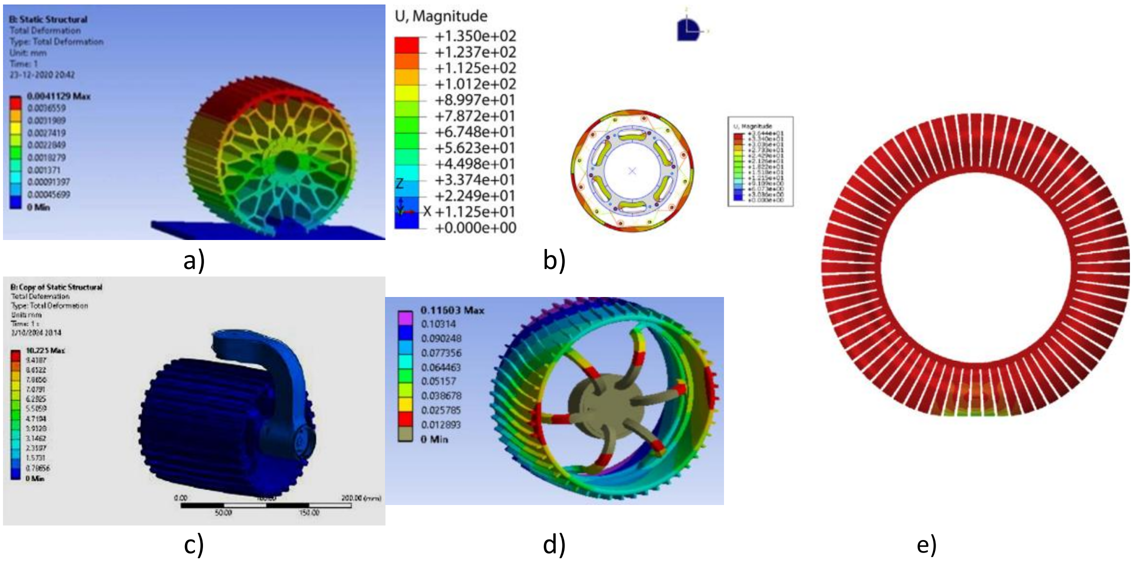

Figure 11 - a) Honeycomb-bullet wheel design total deformation simulation in structural steel [38] b) variable-diameter wheel design deformation simulation when the wheel is at its smallest diameter c) wheel with leaf springs deformation simulation [40] d) deformation simulation of the first study case presented by Agrahari [42] e) flexible metal wheel deformation simulation in the vertical load simulation [41]

5.2. Suspension system

In this section, three different suspension systems will be presented: one developed for the SCORPIO 7 rover, presented by Bernat [43], a rocker-bogie suspension system studied by Agrahari [42], and a parallelogram suspension presented by Pastor [44]. Components showed previously such as the wheel with leaf springs and the flexible metal wheel can be also considered as part of the suspension system, however, they will not be covered in this section. The suspension system analyses presented here all resort to finite element analyses, and the studies range from the year 2018 to 2024.

In the study produced by Bernat [43], the suspension system of the Scorpio 7 rover is introduced, which is a four wheeled vehicle, and then the authors proceed to the optimization and analyses of some of the suspension system's components. The optimization of the triangular beam shape evolved from the FEM analysis, performed in SolidWorks, with a mesh built using tetrahedral finite elements with 10 nodes (TETRA10) and a maximum edge length of

1 mm and loads assigned based on the results from the multibody dynamics simulation (MDS) performed in MSC Adams for the full range of suspension motion. The boundary conditions applied were: fixed displacement at the pivot (bearing) location, force (with a magnitude of 6 N along the X axis, 23.5 N along the Y axis and 1.5 N along the Z axis) was applied to the pushrod mounting location and force (with a magnitude of 78.5 N along the X axis, -26.5 N along the Y axis and -1 N along the Z axis) was applied to the differential beam mounting location. The results of this simulation showed that the largest deformation of the beam occurs close to the attachment point of the pushrod, with a value of 0.37 mm. The rover's frame is also analysed, taking into account the new loads acting on the frame due to the applied changes. The analysis is also performed in SolidWorks with a mesh built using the TETRA10 finite element and a maximum edge length of 1 mm, with the boundary conditions being fixed displacement at the locations in which the frame attaches to the rockers, triaxial stress acting on the differential mechanism's mounts, and the applied forces (500 N in the X axis, 30 N in the Y axis and 15 N in the Z axis). The maximum deflection was observed at the triangular beam's attachment points with a value of 0.22 mm, presenting a reduction compared to the 0.9 mm deflection reached in Scorpio X.

In the study made by Agrahari [42], already introduced earlier, where a micro-rover is designed to explore the dormant Martian lava caves, the authors performed structural studies on the rover's suspension system resorting to ANSYS software. The analysis, conducted on the shock absorbers – which able to absorb shock due to their curved design – resulted in a maximum total displacement of 0.14432 mm, a maximum equivalent von Mises stress of 372 MPa, and a maximum number of 3000 cycles. The analysis was performed with a force of 112 N and a fixed support at the shaft. The analysis conducted on the rocker boogie, made from aluminium alloy, with the boundary conditions being a fixed support at the end of rocker and bogie and load 60 N applied on the rocker-bogie assembly. The results of the analysis showed a maximum total displacement of 0.263 mm, a maximum equivalent von Mises stress was 148.08 MPa and a minimum safety factor of 1.6882.

With the main goal of comparing the applicability of simulations on PTC Creo software and V-REP software in connection with MATLAB, Pastor et al. [44] presented a four wheeled rover with a parallelogram suspension and its simplified version, the lever suspension. The simulations performed in this study were the obstacle crossing simulation and the acceleration and braking simulation. In the obstacle crossing simulation, where only the parallelogram suspension is analyzed, one wheel of the vehicle passes through an obstacle 100 mm high (equal to the wheel radius). In the balanced position, the weight of the rover is equally distributed, and the reaction force on each wheel is 77.5 N in V-REP and 78.8 N in PTC Creo. When the right front wheel is lifted, its reaction force rises to 90 N in V-REP and 88.3 N in PTC Creo, while the rear wheels reach similar values of approximately 83.5 N in V-REP and 84.3 N in PTC Creo. The reaction force on the left front wheel drops to 53 N in V-REP and 56.5 N in PTC Creo. In the acceleration and braking simulation, where the two different suspension systems are analysed, it is showcased that the parallelogram suspension is experiencing more oscillations, despite having the same spring rate and damping parameters as the lever suspension. The deformation analysis, made on the PTC Creo and with the suspension made of aluminium profiles, where the parallelogram suspension is loaded with 250 N simulating the weight of the rover body showcased a maximum displacement in the lower leg, which is 400 mm long, of 0.06 mm. Looking into this work, the lever suspension should be analysed in the obstacle crossing simulation as well as in the deformation analysis, because since the lever suspension showed better results in the acceleration and braking simulation, it could be relevant to study this type of suspension in the other conditions, in order to verify if it can offer any advantages in the different cases.

5.3. Robotic arm

In the literature, analyses have been made on three different robotic manipulators, two of them having 6 DOFs and the other having as many DOFs as necessary for a certain request. The papers introduced in this section resort to FEM in order to simulate some components. The articles' publication year range from 2017 to 2022 providing relatively recent studies.

Starting with the robotic manipulator with 6 DOFs proposed by Sreekanth [45], this arm is made with aluminium alloys and advanced composite materials and its application in interplanetary rovers proves to have a greater advantage over conventional manipulators. The arm is divided into 3 units (Unit 1, Unit 2 and Unit 3) with different functions. Unit 1 is the mount for the arm, made of an aluminium alloy, and holds the carbon fibre rods (OD-50, ID-46). Unit 2 is a prismatic joint whose motion is provided by a linear actuator that is attached to the end of the carbon fibre rod. Unit 3 consists of a carbon fibre rod of diameter 20 mm and is driven by a motor of torque 300 Nm and at the tip of the Unit 3 it has a 150 Nm torque motor coupled. Using the Torque Calculator Software, the torque required at each joint in the worst-case scenario is obtained. The analysis of the manipulator was done by a kinematic study and a structural analysis where the authors used ANSYS and SolidWorks simulation, presenting the simulations for the linear actuator holder and the motor.

Another option for a 6 DOFs robotic manipulator is presented by Pierzgalski [46] with the request to be able to lift loads up to 5 kg. The system is composed of a gripper, four arms, three linear engines and shock absorbers, which are all connected via screws. Three materials were presented for the arm being them constructional steel S185, aluminium alloy 2017 and ABS (Acrylonitrile Butadiene Styrene) which makes the arm’s mass 5.979 kg, 2.146 kg and 0.782 kg, respectively. In order to proceed with the strength analysis, three different computational models were performed, being the FEM adopted in all three. The system has been fixed at the base of the manipulator, and a gravitational force acts on the system. Between the cylinder and a piston rod of a shock absorber, a virtual spring has been used with stiffness 29000 N/m. Virtual pins have been used in the connections of a shock absorber, linear engines and arms, as well as in the connection of arm and gripper. The first and third computational models refer to the object transportation applying a force of 50 N at the lower gripper part, and the second computational model simulates the pulling of a 20 kg mass. The results focus on the maximum von Mises stress, maximum resultant displacement and maximum equivalent strain for the three materials in the three models. The first and third model do not present results for ABS because incorrect results were computed due to significantly exceeded allowable stress, strain, and displacements of the system. It is also verified that the maximum stress slightly exceeds the limit for the aluminium and steel. Through the analysis, the authors concluded that constructional steel (the best when the lowest displacements are the priority factor) and aluminium alloy 2017 can be used as construction materials for the manipulator. Moreover, the manipulator can operate at any configuration with the objects up to 5 kg but in the point of a gripper installation should be used the additional stiffening element in order to reduce the excessive stress. Finally, a manipulator made of ABS can only be used when object transfer is not required. Compared with the work presented by Sreekanth [45], this one showcase a more in-depth analysis which provides more data that can be used in future works, making it a more relevant study.

Lastly Zeis et. al [47] presents a different approach to the robotic arm, suggesting an arm composed of several rotational joints , which rotate under an angle of 45° to the normal axis, eliminating the need for different types of joints, thus reducing the complexity of the modular system. For the dimensioning of the arm, the requirements were a payload mass capability of at least 5 kg, a module length of 600 mm, and a tubular cross-section. It is defined that the total displacement of the end-effector due to bending of the structure must not exceed 2 mm, in the position where bending loads are at their maximum (and, therefore, higher displacements occur); it is also added a safety coefficient of 1.5 to the static loads. In order to determine the loads, the authors used a simplified model of the manipulator in a multibody simulation using Simscape Multibody where the mass of the tubular primary structure is distributed continuously. Additionally, a 5 kg load is added to the end of the manipulator. The simulation, where the first joint rotates by 180° within 10 s from its initial position, yields torque that vary from -400 Nm to 200 Nm. A FEA is conducted on one of the links based on the multibody simulation in order to verify its integrity when exposed to the working loads. This model benefits from the others in the DOF aspect because this, being a modular system, can be added as many rotational joints as possible to achieve the number of DOF needed for the mission. In counterpart, this robotic arm presents greater complexity when in comparison to the others presented and needs as many actuators as rotational joints applied.

5.4. Mechanical components

In this section, four analyses of mechanical components will be addressed, where the authors resort to FEM to further complete the analysis. The articles presented here have publication dates ranging from the year 2012 to the year 2018.

Wang et al. [48] presented a prototype model of a wheel-legged rover with a double-half-revolution mechanism, building it in COSMOS Motion software, where the mechanical data of each gear was obtained by dynamic simulation under the typical working conditions. Next is carried out a FEA of the planetary gear using ANSYS, obtaining values for the tensile side and compressed side of the tooth of maximum deformation, first principal stress, second principal stress, third principal stress and equivalent von Mises stress. Using a discrete optimization method based on ANSYS Parametric Design Language (APDL), the authors optimized the gear, which resulted in an optimized version that met the strength requirement and also presented a 58% weight reduction.

The study presented by Cepeda-Rizo [49] analyses the Laser Power Supply (LPS) of the SHERLOC instrument (Scanning Habitable Environments with Raman & Luminescence for Organics and Chemicals) for NASA's Mars 2020 rover, now known as the Perseverance rover. The authors carried out a fatigue analysis of the LPS for random vibration spectrum for the Atlas V launch vehicle applying in the worst-case direction a spectrum with damping of 2% which the Printed Wiring Assembly (PWA) shown a vibration fatigue life of 20 million cycles which is equivalent to 8 hours of vibration. The maximum chassis stress was 46 MPa at the base of one of the PWA supports, and the maximum deflection of 0.0017" (0.04318 mm) for the main Printed Wiring Board (PWB) and 0.0007" (0.01778 mm) for the Bank PWB. Also, in the analysis of the chassis fasteners, it can be observed that the maximum stress obtained is 9.56 MPa at bottom cover of one of the M2 screws. It was concluded that the Main PWA, as well as the capacitor bank PWAs had no issues when subjected to the random vibration environment.

Melzer et. Al [50] presented an overview of the Core Sample Transportation Mechanism (CSTM), whose function is to receive a drill sample and transfer it to sample preparation units and to the analysing instruments. This mechanism needs to be able to retain the Ultra Clean Zone (UCZ) free from contamination over the non-operational lifetime of the Sample Powder Distribution System and to ensure successful sample delivery during its operations. A detailed design solution is presented where the Sample Carrier is analysed to obtain the deformations and the von Mises stress, leading to a result of deformation of the sample carrier until a small gap of approximately 200 µm is closed and a maximum von Mises stress of 342.65 MPa. Two tests were then carried out, the first being a leakage test campaign and the second a functional testing. The first one showcased that, in one of the cases for this study, the results were slightly higher for some seconds than the threshold value of 2.04×10^{-7} mbar.l/s, although this test is for conditions of -60 °C and 200 mbar, which will not be achieved during the component's lifetime. In the second test, the main objective was to verify the function of the Sample Carrier lever mechanism under various conditions, where no influences of the actuation speed or the inclination of the system on the Sample Carrier functionality was observed and proved the good operation of the Sample Carrier under temperatures up to -80 °C. The failure cases on this last test were due to extreme contamination or intentional blockage.

The last work in this category is the one made by Cao [51], which conducted a structural analysis on flanges for steering racks of a Mars rover prototype, presenting a static analysis resorting to SolidWorks 2012 structural analysis program. Initially, the authors present the six-wheeled rover with a rocker-bogie suspension system and propose the three basic movement patterns (go forward and back, situ rotation, large radius rotation). Next, a case study is suggested, where the load from the vehicle is transmitted through the two screws and then presses on the wall of the screwed holes, making the stress analysis with the following characteristics: weight of 40 kg, the flange material is 2024 aluminium alloy, screw type is M4. Calculating the screw preloading torque was obtained a torque of 18.7115 Nm. Next, the bottom surface of the flange was fixed, were added screw connections to six M4 screwed holes, with the torque previously obtained, and, lastly, a 150 N load was added to the two screwed holes. Results showed a maximum total displacement value of 2.371×10^{-3} mm at the top part of the flange towards the main body of the vehicle and a maximum von Mises stress of 8.403 MPa located at three screwed holes which is further than the other three according to the distance from the main body of vehicle. The authors concluded that the maximum deformation value is under safety range, because the nearest distance between servo motor and flange in wall is ≥ 4 mm and the design of flange would not cause permanent deformation and fracture since the maximum stress obtained was far below the 2024 aluminium alloy yield limit of 96 MPa.

5.5. Soil interaction

In this section, seven articles referring to soil interaction analysis will be addressed, focusing mainly on the interaction between the wheel and the soil, although other interactions are still presented. Unlike the review made for other rover components, in this section the analyses resort to meshless methods, being the DEM predominant but the RKPM and SPH are also used. The publication dates of the papers presented here range from the year 2011 to the year 2024.

In an article presented by Li [52], an analysis of the lunar dust distribution caused by a lunar rover wheel rotation and, for that, a DEM analysis is performed. For the wheel, steel was selected as the material with a density of 7.8 kg/m^3, and the wheel design had a diameter of 300 mm and a width of 10 mm. Lugs with a length of 15 mm and 2 mm thick were added, and a vertical load of 20 kg and a gravitational acceleration of 1.635 m/s^2 were applied to the wheel. For the dust particles, the density selected was 1870 kg/m^3, a centre element radius of 0.5 mm, cohesion of 4.0 kPa, shear modulus of 50 MPa, internal friction angle of 52.7°, and Poisson's ratio of 0.28. A total of 188908 particles were used with the same gravitational acceleration applied on the wheel. The simulation showcased a maximum height of raised lunar dust of 0.015m, 0.024m, 0.32m, 1.20m, 3.20m for the travelling speed of, respectively, 0.5m/s, 1 m/s, 3 m/s, 5 m/s, 7 m/s.

Lichtenheldt et. Al [53] analysed, in their work, the HP^3-Mole (Heat Flow and Physical Properties Package), which is part of the InSight lander and is a self-impelling nail design with the goal of measuring the heat flux and thermal gradient of Mars's soil down to a final depth of 5 m. For the simulations, two models based on enhanced multi-body dynamics and discrete element techniques were used. Coupling the two methods provided a better understanding of the interaction between the mole and the soil. For the validation of the results, measurements of prototypes were made and then compared with the results of the simulations. It was showcased that in the first 0.1 m depth, the simulated tip stress is above the measurement values and outside the confidence bounds, and between 0.1 m and 0.8 m, the tip resistance rises again with some deviations. Also, the full stroke simulation in a depth of 1 m resulted in a penetration of 2.2 mm, which is in concordance with the mean penetration of 1.8 mm and in the same depth range as the real deep penetration measurement. The operation of the HP^3-Mole causes a shockwave, and the animation is made possible by this type of simulation, as shown in Figure 12 a).

In order to investigate rover wheel interactions with Martian regolith and regolith deformation in a geotechnical triaxial strength cell (GTSC), Knuth et al. [54] applied a three-dimensional DEM simulation. This simulation was created of a laboratory experiment that involved a MER wheel digging into lunar regolith simulant, improving interpretations of laboratory and in situ rover data, and simulating complicated regolith conditions. The results for the sinkage and torque measured in the experiment were compared with the ones predicted numerically, where simulated particles with shapes such as spheres, ellipsoids, and poly-ellipsoids were used. GTSC simulations indicated a peak friction angle of approximately 37 to 38°, compared to internal friction angles of 36.5 to 37.7° determined from the experiments. The density of the DEM regolith was 1820 kg/m^3, superior to the 1660 kg/m^3 used in the experiment, which indicated that the bulk strength is determined by the number of grain contacts and grain contact resistance and not the density.

In the paper presented by Johnson [55], three-dimensional Discrete Element Method simulations of MER wheel mobility tests for wheel slip ratios of 0, 0.1, 0.3, 0.5, 0.7, 0.9, and 0.99 were conducted. This was done in order to study high wheel slip mobility and improve the Adams-based rover terramechanics and mobility interaction simulator (ARTEMIS) MER traverse planning tool. In order to determine the Discrete Element Method particle packing density of 0.62 and the contact friction of 0.8, which represented the simulant used in mobility tests, wheel drawbar pull simulations and sinkage were used, as well as Massachusetts Institute of Technology (MIT) data for a slip ratio ≤ 0.5. The Discrete Element Method simulations were in good agreement with MIT data for slip ratio $= 0.5$ and 0.7, with agreement being less at lower wheel slip and equilibrium sinkage occurred for slip ratio < 0.9, but continuously increased for slip ratio $= 0.99$. The authors concluded that improved DEM simulation accuracy of low-slip mobility (slip ratio < 0.3) can be achieved using polyhedral particles, rather than tri-sphere particles, to represent soil.

In the AIAA Modeling and Simulation Technologies Conference [56], a wheel-soil interaction is developed and analysed using the meshfree method RKPM. This analysis is further compared with an analysis made with a finite element with Lagrangian meshing and to empirical relationships proposed by Bekker [57] as a standard for comparison. The simulation model consists of a rigid wheel and a mesh-free soil domain, where the rotating wheel is compressed vertically into the soil with prescribed angular rotation. The wheel is assumed to be rigid, while is considered the frictional contact between the wheel and soil. In this simulation, the wheel diameter equals 10 in (254 mm), the vertical compression is 0.6 in/s (15.24 mm/s), the angular velocity equals 10 rad/sec and the simulation has a duration of 8 s. Now related to the soil, the elastic modulus equals 2880.8 psi (19.86 MPa), the Poisson’s ratio is 0.28, the cohesion is 6.6 psi, the friction angle is 31.68°, the density is 129.86 lb/ft^3 (2080.16 kg/m^3), the initiating damage strain is 2.5%; the coefficient of friction between wheel and soil is 0.4. The simulation with Lagrangian meshing is implemented using LS Dyna software using similar parameters with the ones on the RKPM simulation. The results shown in Figure 12 b) verify the proximity between empirical relationships proposed by Bekker [57] and the simulation made with RKPM, unlike the simulation with Lagrangian meshing, which proves that RKPM is better for this analysis when using empirical relationships proposed by Bekker [57] as standard.

In a study presented at the Structures, Structural Dynamics, and Materials and Co-located Conferences [58], the JPL wheel-soil benchmark problem is implemented in the commercial code environment utilizing the large deformation modelling capability of SPH meshfree methods. In the benchmark problem, the density equals 2350 kg/m^3, the shear modulus is 34.5 MPa, and the bulk modulus for unloading is 15.0 MPa. One of the simulations made in this work consists of a wheel traverse case over a soil sandbox, which is made using LS-DYNA ensuring a proper definition of the contact interface and friction parameters. The friction coefficient between wheel and soil is 0.4, obtaining the results shown in Figure 12 c). For the study of the sinkage and slippage of the wheel, an eight-second simulation was performed, resorting to a hybrid approach. In this approach, the outer portion of the sandbox is discretized using a Lagrangian soil mesh and the inner portion near the wheel-soil contact interface uses a SPH soil domain. The wheel was compressed into the soil at 0.6 in/s (15.24 mm/s), and the spinning rate was 1 rad/s, leading to the results presented in Figure 12 d). In the end, the authors concluded that the model was shown to produce realistic results for both a wheel traverse case and a wheel sinkage case.

In the study presented by Yang [59], experiments and DEM simulations of single-wheel tests under fixed sinkage conditions were used to further analyse wheel-terrain interaction from a granular perspective. In the experimental test, it was carried out a controlled sinkage test having as a variable the load on the wheel, with a smooth wheel with a radius of 135 mm and a width of 165 mm. For the soil, a simulated Martian soil labelled as HIT-MSS1 was used with cohesive modulus of $13.6\ \mathrm{kPa/m^{n-1}}$, frictional modulus of $2259.1\ \mathrm{kPa/m^{n}}$, sinkage exponent of 0.92, cohesion of 0.462 kPa, internal friction angle of 35.0° and soil deformation modulus of 15.0 mm. For the DEM simulation, a wheel with the same radius and width as the experimental one was selected. The parameters for the soil were chosen to be as similar as the soil used in the experimental test. The comparative analyses of both the experimental tests and the DEM simulations showed good agreement for the pull coefficient and the tractive coefficient, except in the slip state when the sinkage was 15 mm where those parameters increased significantly in the experiment when compared with the simulation. Both parameters increased almost linearly with the slip ratio < 0.3 and, excluding the discordance between the two methods for the sinkage of 15 mm, the parameters showed a slow increase with the slip ratio for slip ratio > 0.3 The analysis of the soil through the simulations showed that when the rotational speed reached the lowest value at a slip ratio of -0.6 occurred soil accumulation in front of the wheel. As the wheel started to rotate the slip ratio increased and when it reaches a value of -0.3 the movement of the wheel causes particles in front of the wheel to gradually shift downward. Reaching a positive slip ratio, the accumulation of soil particles in front of the wheel becomes negligible. Lastly, at a slip ratio of 0.3, the planetary soil beneath the wheel is moved backward. The distribution of the pressure field in the planetary soil showed that the stress is concentrated in the central part of the contact area between the wheel and planetary soil.

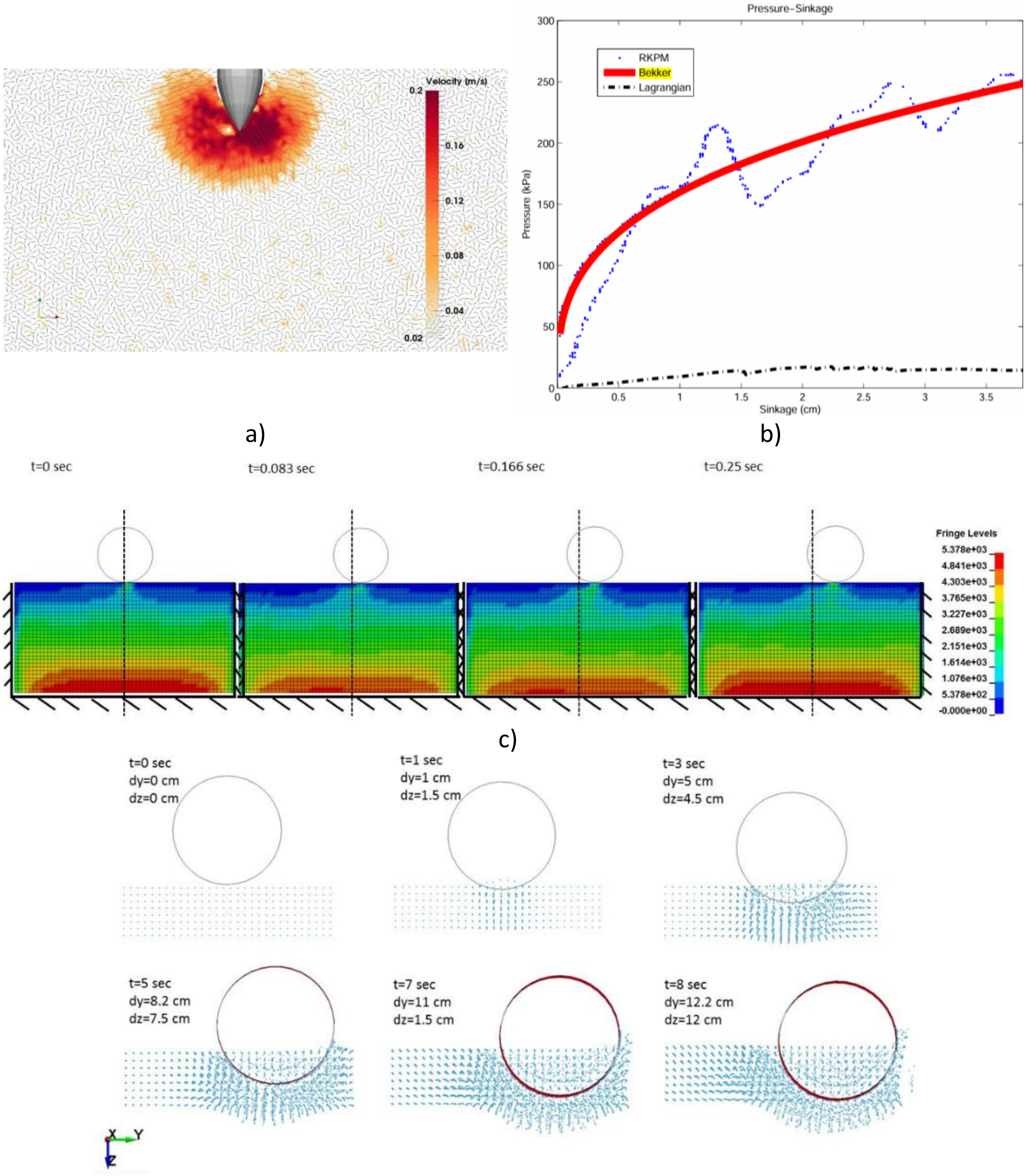

a) b)

c)

d)

Figure 12 – a) Frame of the shockwave analyses result of the HP^3-Mole taken 2.5 ms after the impact [53]; b) Comparison of the results obtained by RKPM, Bekker and Lagrangian meshing [56]; c) Wheel traverse simulation results showing pressure in the soil (Pa) [58]; d) Soil elements displacement [58]

5.6. Thermal analysis

This section will address two documents where thermal analyses of distinct rover components are carried out, both of them resorting to FEM and with publication dates in 2018 and 2023.

In the article presented by Cepeda-Rizo [49], a thermal analysis of the LPS is conducted. The thermal model of the LPS chassis assembly, which includes the Main PWA, was created using SolidWorks Simulation finite element code. The main PWB was attached to the chassis, and thermal planes were estimated across the entire main board, with focus placed on careful spreading estimation underneath the high-power MOSFET devices M3 and M4. Next was conducted a transient thermal analysis showing a steady state maximum temperature of 112.36 °C for a boundary temperature of 70 °C.

Xiang et. Al [60] developed in their work a comprehensive finite element model of the Multi-Mission Radioisotope Thermoelectric Generator (MMRTG), using the software COMSOL Multiphysics. This included a full-size three-dimensional geometry model, temperature dependent materials and the thermoelectric and radiation heat transfer multiphysics fields involved. To simplify the analysis, the authors made the following assumptions: the complex structure of the housing cover is simplified, which features a negligible effect on heat dissipation; the positioning components, such as springs and locating pins inside the module bar, are ignored, and replaced by the contact thermal resistance in the calculation; the wires connecting the thermoelectric modules are ignored, and their effects are represented by the equivalent potential in the calculation and the thermal; electrical contact resistance between the thermoelectric legs and electrodes are ignored as well. The performance analysis focuses on the thermal profile and power profile and then the parametric analysis focuses on the impact of load and thermal inventory, ambient temperature, thermal conductivity of thermal insulation material and fin emissivity and size. From the performance analysis, the authors obtained the total efficiency (η_{sys}) of 6.26%, thermal efficiency (η_{th}) of 90.48% and thermoelectric conversion efficiency (η_{TE}) of 6.92% of the MMRTG system. The parametric analysis results clarify the system properties, working mechanisms and design parameters of the MMRTG, which can be used to design more optimal models.

6. Numerical Benchmark Problems

To verify the numerical method to be used in analysing the rover component, a convergence test will be performed on a benchmark problem: the Cantilever Beam. In total, eight different analyses will be performed, namely: the FEM, the RPIM, and the NNRPIM (with 1 and 2 degrees of neighbourhood), which will be executed for both a mesh with 3-node triangular elements and a mesh with 4-node quadrangular elements.

Afterwards, to verify the remodelling algorithm that will be further used in the present dissertation, remodelling analyses were performed on the same Cantilever Beam. The analysis will be compared with results presented in the work developed by M.P. Bendsøe [61].

All the analyses were performed with the software FEMAS (cmechrlab.wordpress.com), which allows the linear and non-linear analysis of 2D and 3D problems using FEM formulations and RPIM and NNRPIM meshless methods. The 2D and 3D computational models were constructed with FEMAP student edition software (https://plm.sw.siemens.com/en-US/simcenter/mechanical-simulation/femap/).

6.1. 2D cantilever beam

In this study, it is performed a 2D analysis over a beam with a length (L) of 2 m, a width (D) of 1 m, and a thickness of 1 m is constrained on the left side, and a distributed load (P) of 1 N/m is applied along the right side, as shown in Figure 13. The material used for this study has a Young's modulus (E) of 1 kPa and a Poisson's ratio (υ) of 0.3. The study will focus on three points (A,B and C) of the beam, analysing the displacement along y (v) in point A, shear stress (τ_{xy}) in point B and stress (σ_{xx}) in point C. The results of the simulations will then be compared with the analytical solution presented in the equations (47) and (48) [24].

$$\begin{gathered}\sigma_{xx} = -\frac{P \cdot (L-x) \cdot y}{I} \\ \sigma_{yy} = 0 \\ \sigma_{xy} = \frac{P \cdot D^2}{8 \cdot I} \cdot \left(1 - \frac{4y^2}{D^2}\right)\end{gathered} \tag{47}$$

with $I = D^3/12$ since the beam's cross-section is square.

$$u(x) = -\frac{2P}{E \cdot D^3}\left[3x \cdot (2L-x) \cdot y + (2+\upsilon) \cdot \left(y^2 - \frac{D^2}{4}\right) \cdot y\right] \tag{48}$$

$$v(x) = \frac{2P}{E \cdot D^3}\left[x^2 \cdot (3L - x) + 3\upsilon \cdot (L - x) \cdot y^2 + x \cdot (4 + 5\upsilon) \cdot \frac{D^2}{4}\right]$$

For the RPIM analysis, 16 nodes per influence domain are considered, and a Gaussian integration employing quadrilateral integration cells consisting of 2×2 integration points is used. As for shape parameters used in the MQ-RBFs, they are c = 1.42 and p = 1.03. Regarding the NNRPIM analysis, the integration will be a full integration and the parameters to be used in the MQ-RBF are c = 0.0001 and p = 0.9999.

The meshes used in the study started with 4 divisions along the Ox axis and 2 divisions along the Oy axis. By doubling each division, 128 divisions were reached along the Ox axis and 64 divisions along the Oy axis, as shown in Table 5. This was done for both 3-node triangular elements and 4-node quadrangular elements meshes, as shown in Figure 14.

Table 5 – Divisions and number of nodes of each mesh

x-axis divisions	y-axis divisions	number of nodes
4	2	15
8	4	45
16	8	153
32	16	561
64	32	2145
128	64	8385

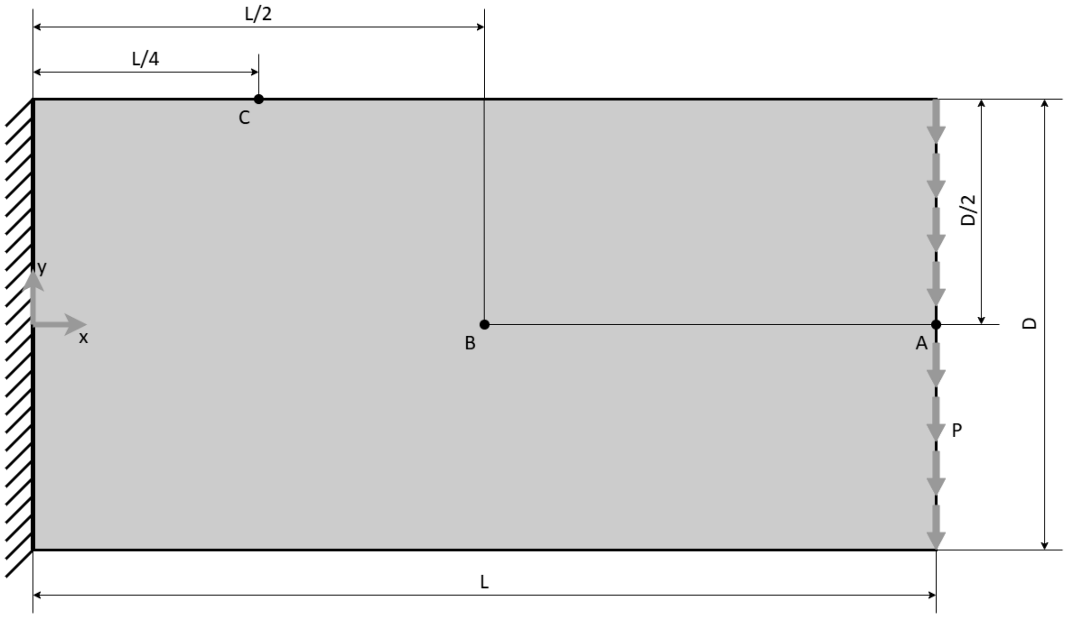

Figure 13 - Illustration of the Cantilever Beam 2D

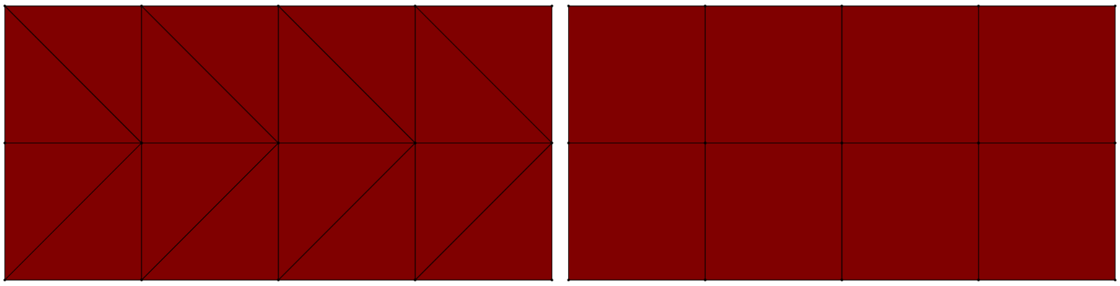

a) b)

Figure 14 - a) 3 nodes triangular elements mesh; b) 4 nodes quadrangular elements mesh

The numerical results are shown in Figure 15, Figure 16 and Figure 17 where all the charts include the analytical solution in order to prove the convergence of each method. Figure 15 shows the displacement on the y-axis of point A with coordinates (2,0). It can be observed that, for the 3-node triangular element mesh, the FEM analysis needs a higher discretization to obtain a result closer to the analytical, when comparing it with the FEM analysis with a 4-node quadrangular elements mesh or any of the other methods. The RPIM analyses show some small differences in the values obtained from each mesh. Looking to the NNRPIM(V1) (1 degree of neighbourhood) and NNRPIM(V2) (2 degrees of neighbourhood) analyses, there is no difference between using 3-node triangular element meshes or 4-node quadrangular elements meshes since the method does not depend on a mesh to obtain those results. All analysis presented show convergence and, excluding the FEM analysis with the 3-node triangular element mesh, all the analysis showcases similar curves.

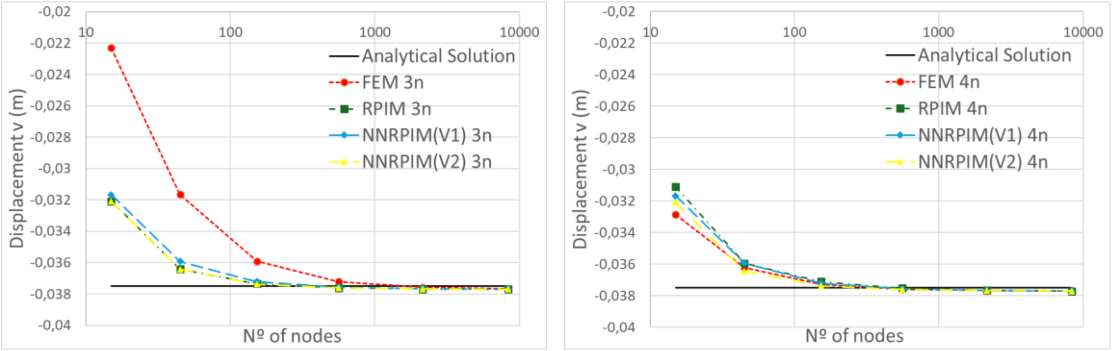

a) b)

Figure 15 - a) Displacement (v) analysis results with 3-node triangular elements mesh; b) Displacement (v) analysis results with 4-node quadrangular elements mesh

In Figure 16, it is displayed the shear stress obtained from the analysis focusing on point B with coordinates (1;0). In this case, the RPIM, NNRPIM(V1) and NNRPIM(V2) analyses show similar curves differing from the FEM analyses. Using the 3-node triangular elements mesh, the FEM analysis did not obtain a result close to the analytical when comparing with the other methods, even with the mesh with 8385 nodes. This problem does not occur when using a mesh with 4-node quadrangular elements. Despite that, all the methods showcased convergence for both meshes.

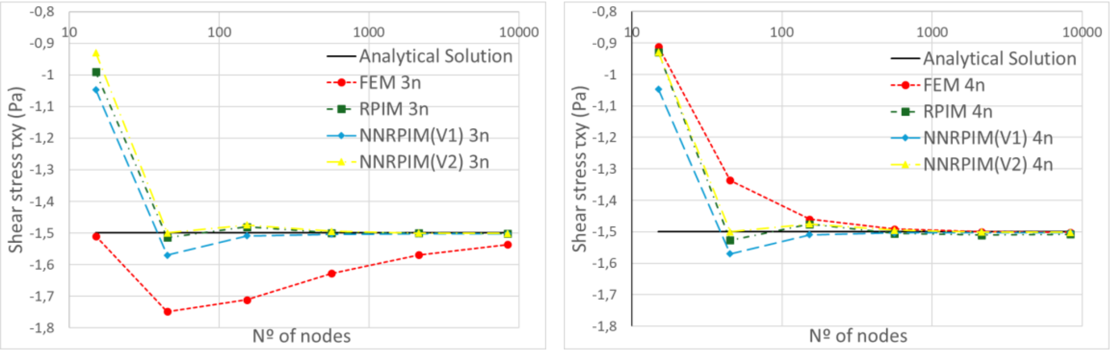

a) b)

Figure 16 - a) Shear stress (τ_{xy}) analysis results with 3 nodes triangular elements mesh; b) Shear stress (τ_{xy}) analysis results with 4 nodes quadrangular elements mesh

In Figure 17 is showcased the stress on point C with coordinates (0.5;0.5) obtained from the analysis. Differing from the previous analysis showed in Figure 15 and Figure 16, in this case, the method that shows more proximity to the analytical solution is the FEM with 3-node triangular elements mesh. Nevertheless, all the other methods demonstrate convergence for both meshes.

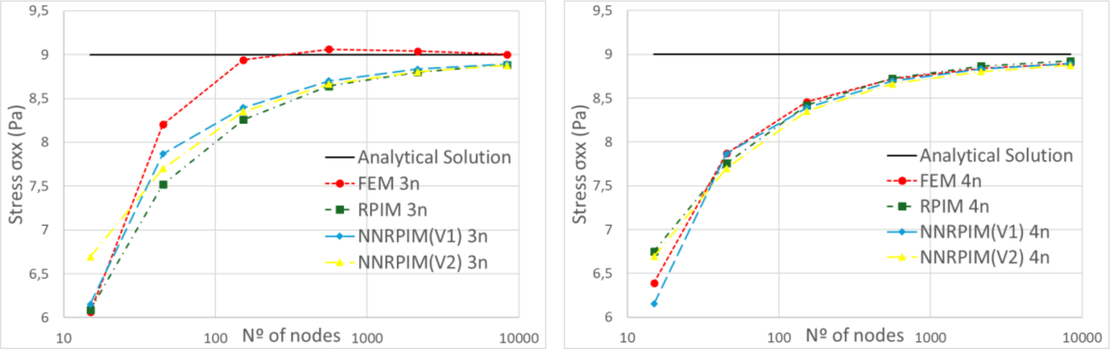

a) b)

Figure 17 - Stress (σ_{xx}) analysis results with 3 nodes triangular mesh; b) Stress (σ_{xx}) analysis results with 4 nodes quadrangular mesh

In Figure 18 to Figure 21 are presented the displacement (u), displacement (v), stress (σ_{xx}) and shear stress (τ_{xy}) colour maps, respectively, of all the methods for both meshes. Excluding the shear stress colour maps, all the others presented similar results that can hardly be noticed visually. For the shear stress, the colour maps are distinct from each other with the most different being the FEM analysis with 3-node triangular mesh.

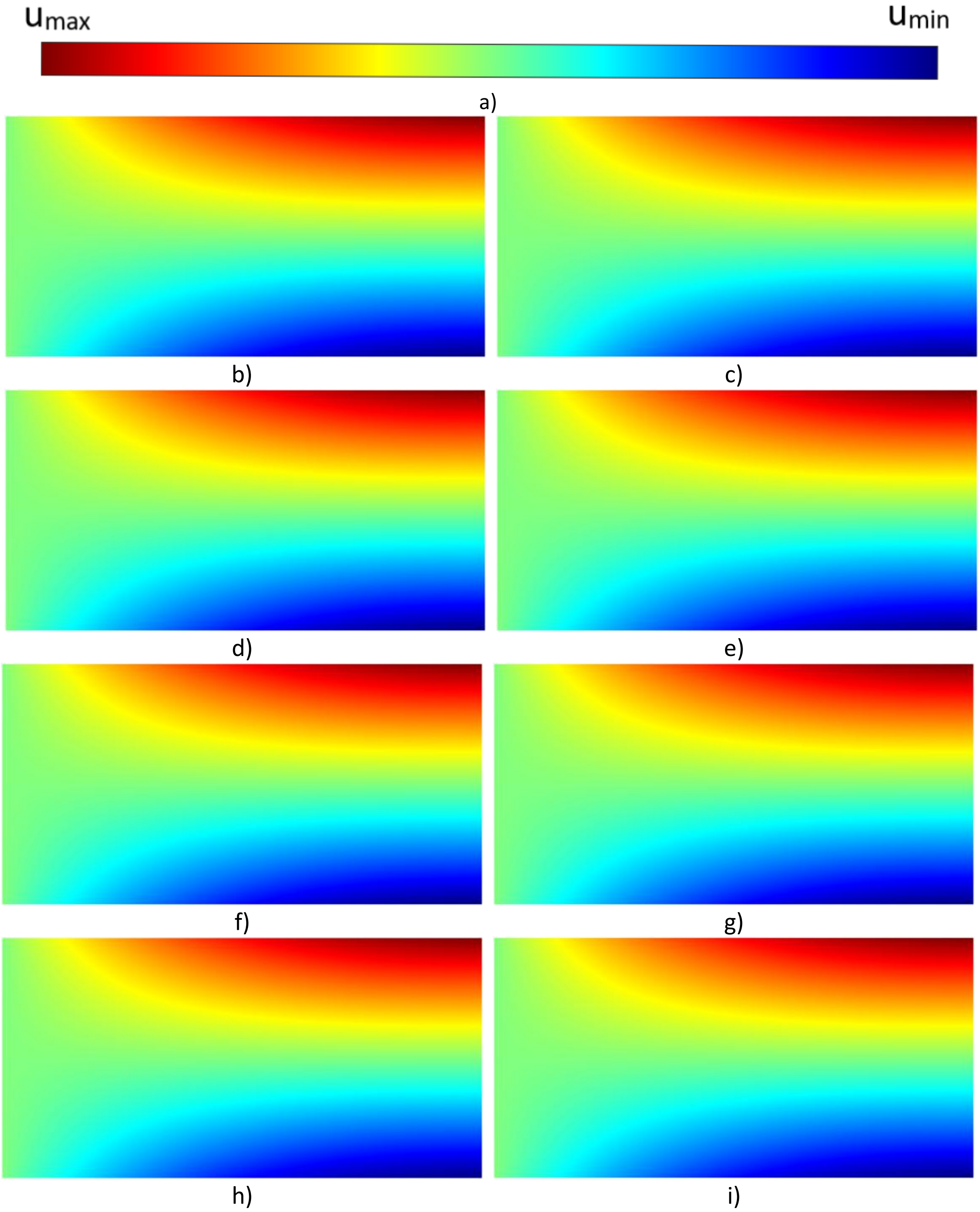

a) b) c) d) e) f) g) h) i)

Figure 18 – a) Colour bar for u results b) FEM 3n (u_{max}= 0.0124 m u_{min}= -0,0124 m); c) FEM 4n (u_{max}= 0,0124 m u_{min}= -0,0124 m); d) RPIM 3n (u_{max}= 0,0124 m u_{min}= -0,0124 m); e) RPIM 4n (u_{max}= 0,0124m u_{min}= -0,0124 m); f) NNRPIM(V1) 3n (u_{max}= 0,0124 m u_{min}= -0,0124 m); g) NNRPIM(V1) 4n (u_{max}= 0,0124 m u_{min}= -0,0124 m); h) NNRPIM(V2) 3n (u_{max}= 0,0124 m u_{min}= -0,0124 m); i) NNRPIM(V2) 4n (u_{max}= 0,0124 m u_{min}= -0,0124 m)

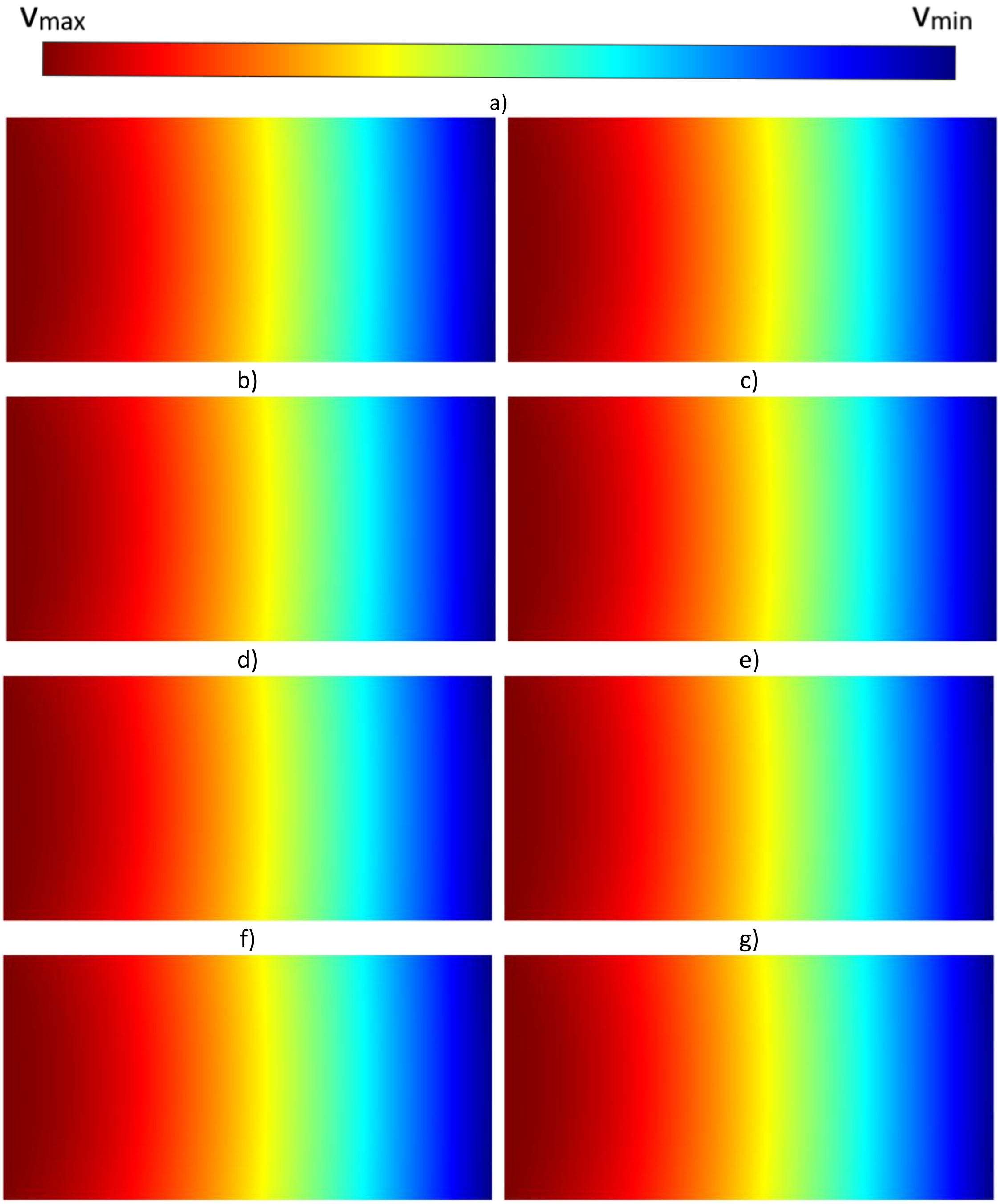

a)

b) c)

d) e)

f) g)

h) i)

Figure 19 – a) Colour bar for v results b) FEM 3n (v_{max}= 0 m v_{min}= -0.0382 m); c) FEM 4n (v_{max}= 0 m v_{min}= -0.0382 m); d) RPIM 3n (v_{max}= 0 m v_{min}= -0.0382 m); e) RPIM 4n (v_{max}= 0 m v_{min}= -0.0382 m); f) NNRPIM(V1) 3n (v_{max}= 0 m u_{min}= -0.0382 m); g) NNRPIM(V1) 4n (v_{max}= 0 m v_{min}= -0.0382 m); h) NNRPIM(V2) 3n (v_{max}= 0 m v_{min}= -0.0382 m); i) NNRPIM(V2) 4n (v_{max}= 0 m v_{min}= -0.0382m)

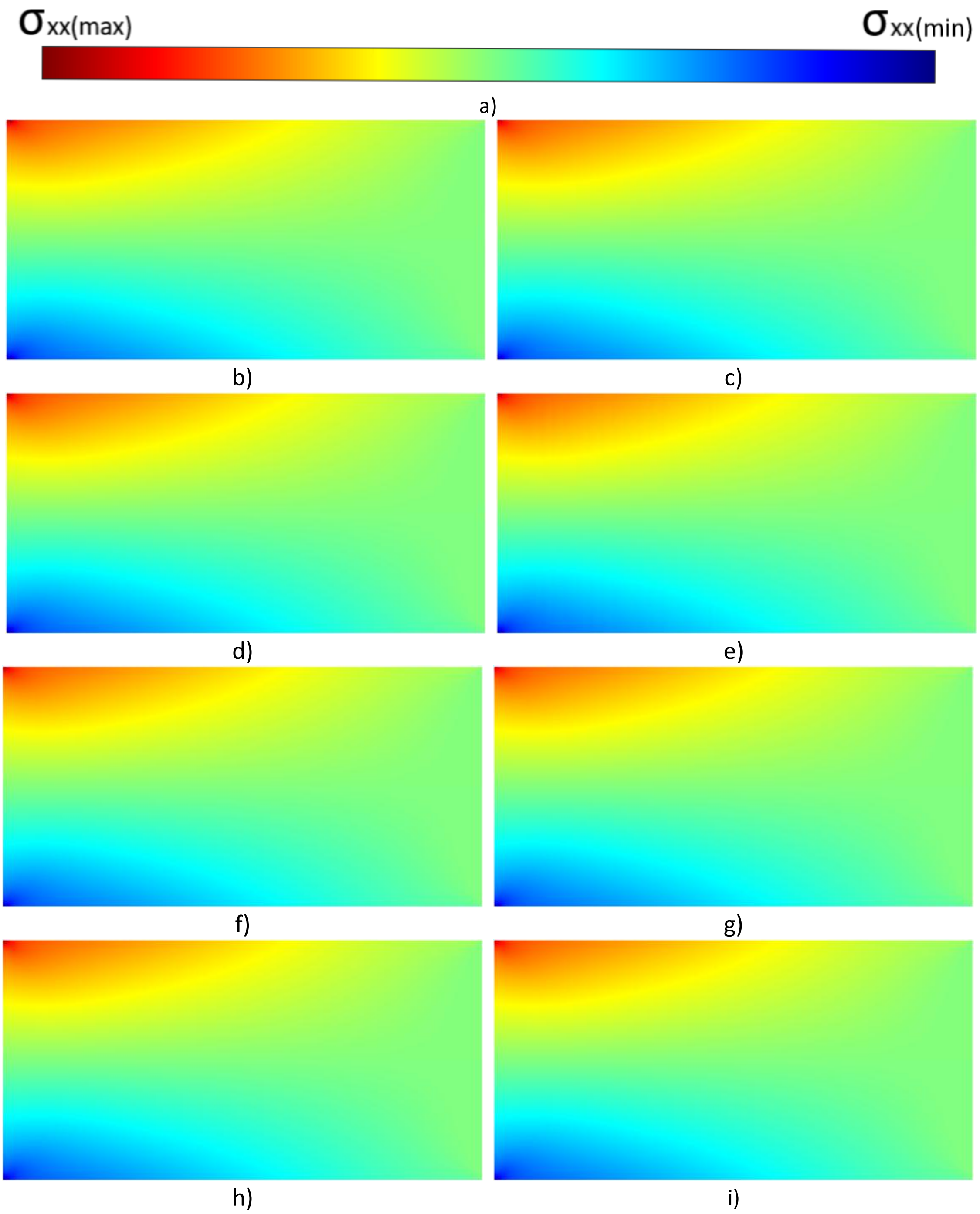

a)

b) c)

d) e)

f) g)

h) i)

Figure 20 – a) Colour bar for σ_{xx} results b) FEM 3n ($\sigma_{xx\,max}$= 19.2411 Pa $\sigma_{xx\,min}$= -19.2411 Pa); c) FEM 4n ($\sigma_{xx\,max}$= 19.4273 Pa $\sigma_{xx\,min}$= -19.4273 Pa); d) RPIM 3n ($\sigma_{xx\,max}$= 19.0700 Pa $\sigma_{xx\,min}$= -19.0700 Pa); e) RPIM 4n ($\sigma_{xx\,max}$= 19.3670 Pa $\sigma_{xx\,min}$= -19.3670 Pa); f) NNRPIM(V1) 3n ($\sigma_{xx\,max}$= 19.5938 Pa $\sigma_{xx\,min}$= -19,5938 Pa); g) NNRPIM(V1) 4n ($\sigma_{xx\,max}$= 19.5938 Pa $\sigma_{xx\,min}$= -19.5938 Pa); h) NNRPIM(V2) 3n ($\sigma_{xx\,max}$= 19.3898 Pa $\sigma_{xx\,min}$= -19.3898 Pa); i) NNRPIM(V2) 4n ($\sigma_{xx\,max}$= 19.3898 Pa $\sigma_{xx\,min}$= -19.3898 Pa)

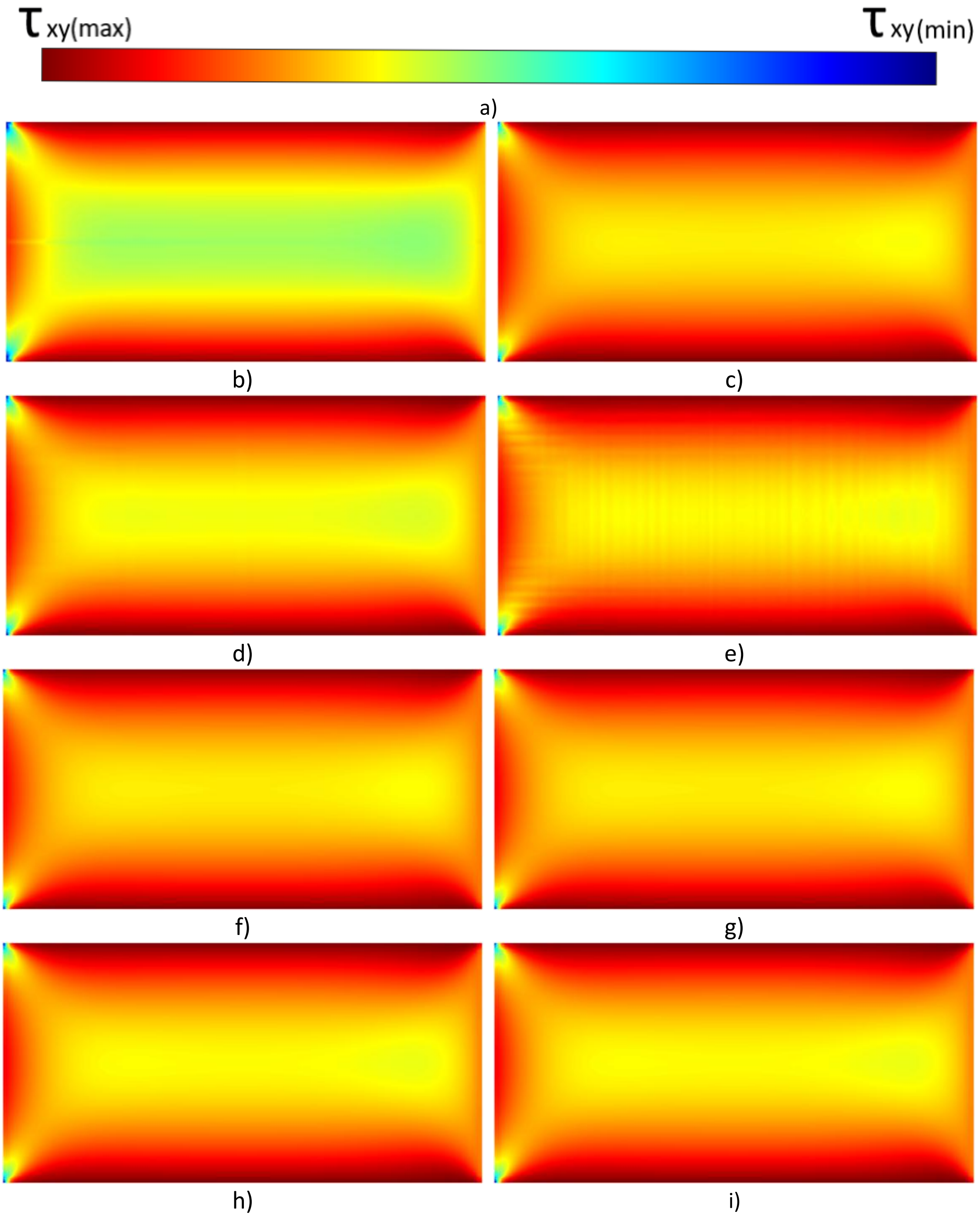

a)

b)

c)

d)

e)

f)

g)

h)

i)

Figure 21 – a) Colour bar for τ_{xy} results b) FEM 3n ($\tau_{xy\ max}$= 0.0705 Pa $\tau_{xy\ min}$= -3.3212 Pa); c) FEM 4n ($\tau_{xy\ max}$= -0.0133 Pa $\tau_{xy\ min}$= -4.1263 Pa); d) RPIM 3n ($\tau_{xy\ max}$= -0.0078 Pa $\tau_{xy\ min}$= -3.8501 Pa); e) RPIM 4n ($\tau_{xy\ max}$= -0.0102 Pa $\tau_{xy\ min}$= -4.0110 Pa); f) NNRPIM(V1) 3n ($\tau_{xy\ max}$= 0.0238 Pa $\tau_{xy\ min}$= -4.2248 Pa); g) NNRPIM(V1) 4n ($\tau_{xy\ max}$= 0.0238 Pa $\tau_{xy\ min}$= -4.2248 Pa); h) NNRPIM(V2) 3n (u_{max}= -0.0111 Pa u_{min}= -3.9994 Pa); i) NNRPIM(V2) 4n ($\tau_{xy\ max}$= -0.0111 Pa $\tau_{xy\ min}$= -3.9994 Pa).

6.2. 3D cantilever beam

This analysis was performed in a similar way to the 2D analysis, only including the thickness (t) and analysing it with a 3D approach. The beam has a length (L) of 2 m, a width (D) of 1 m and a thickness that varies according to the dimension of the mesh division, being equal to twice a division as shown in Table 6. The beam is constrained in the left side and a distributed load (P) equal to one time the thickness is applied in the right side along the Oxy plane, as show in Figure 23 and Table 6. The material of the beam is the same as for the 2D analysis. Points A, B and C are again used to obtain the displacement along y (v), shear stress (τ_{xy}) and stress (σ_{xx}) respectively. The results will then be compared with the analytical solution obtained from equations (47) and (48) [24].

In the RPIM analysis, 27 nodes will be within each influence domain and c = 1.42 and p = 1.03 will be used in the MQ-RBF. The Gaussian integration will be performed by employing hexahedral integration cells consisting of 2×2×2 integration points. For the NNRPIM analysis, the integration will be a full integration and the parameters to be used in the MQ-RBF are c = 0.0001 and p = 0.9999.

The meshes used in the study started with 4 divisions along the Ox axis, 2 divisions along the Oy axis and 2 divisions along Oz axis and, by doubling each divisions, except for the z-axis divisions, were reached 64 divisions along the x-axis, 32 divisions along the y-axis and 2 divisions along the z-axis, as shown in Table 6 for both the 4-node tetrahedral elements and a 8-node hexahedral elements meshes, as shown in Figure 23.

Table 6 - Divisions, number of nodes, thickness and load in each mesh

x-axis divisions	y-axis divisions	z-axis divisions	number of nodes	thickness (t)	load (P)
4	2	2	45	1 m	1 N/m
8	4	2	135	0.5 m	0.5 N/m
16	8	2	459	0.25 m	0.25 N/m
32	16	2	1683	0.125 m	0.125 N/m
64	32	2	6435	0.0625 m	0.0625 N/m

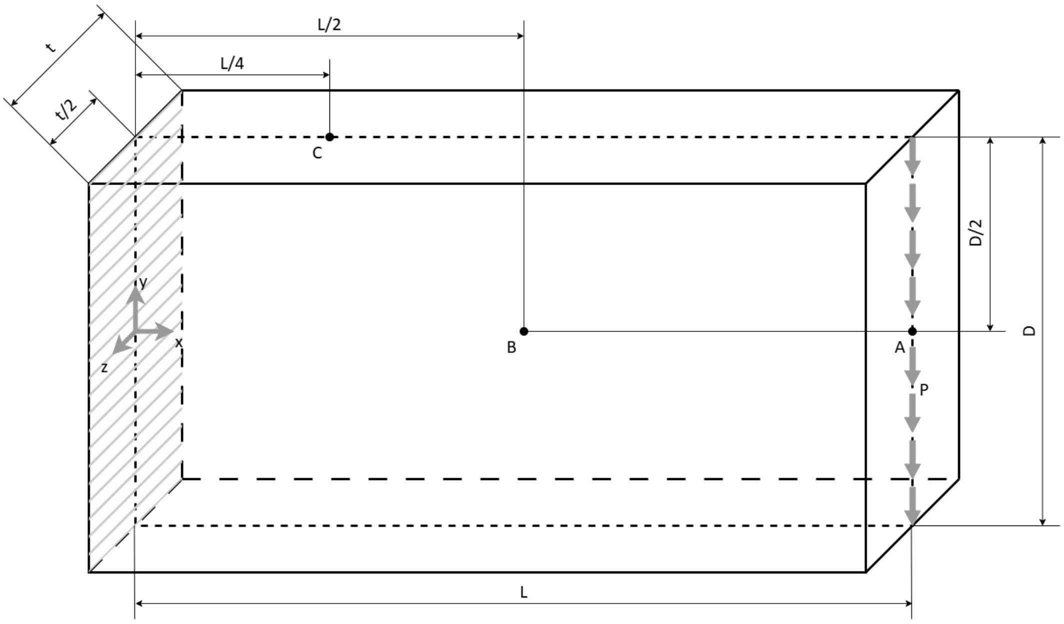

Figure 22 - Illustration of the Cantilever Beam 3D

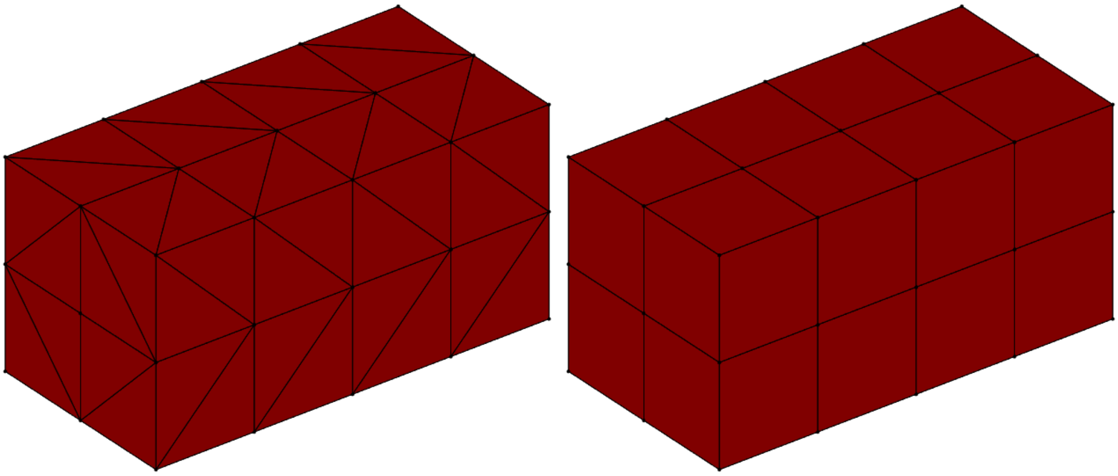
a)
b)

Figure 23 - a) 4 nodes tetrahedral elements mesh; b) 8 nodes hexahedral elements mesh.

Similar to the 2D study, are presented in Figure 24, Figure 25 and Figure 26 the results of the simulations for each method in order to compare them with the analytical results and verify the convergence of the methods. In Figure 24 the results of the displacement along the Oy axis are obtained in point A with coordinates (0;2;0). All methods show a similar curve apart from the FEM with 4-node tetrahedral elements mesh, which only obtained results close to the analytical solution using meshes with more nodes when comparing it with the remaining methods. Nevertheless, the graphs clearly demonstrate that all methods are convergent.

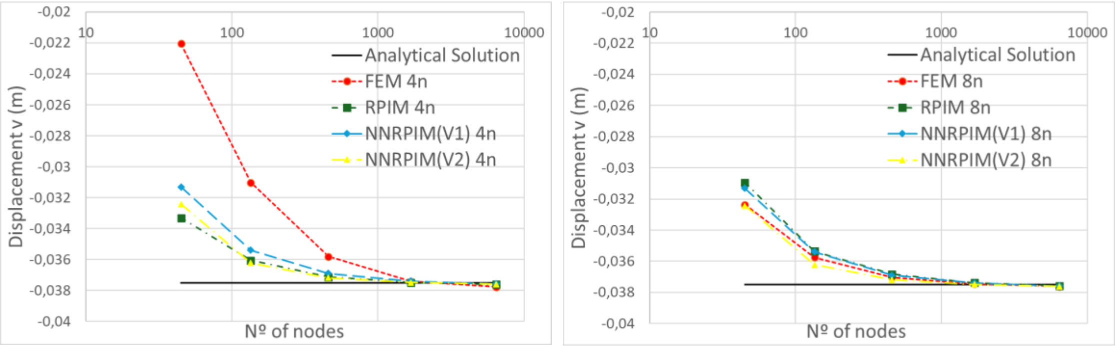

a) b)

Figure 24 - a) Displacement (v) analysis results with 4-node tetrahedral elements mesh; b) Displacement (v) analysis results with 8-node hexahedral elements mesh

Figure 25 shows the results for the shear stress obtained at point B, with coordinates (0;1;0). In this case, it can be observed that the meshless methods converged faster than the FEM. For the meshes composed of 8-node hexahedral elements, the convergence is achieved for all methods, despite the FEM being slower. As for the mesh with 4-node tetrahedral elements, the FEM curve is dispar from the others and shows that the method does not converge to the analytical solution.

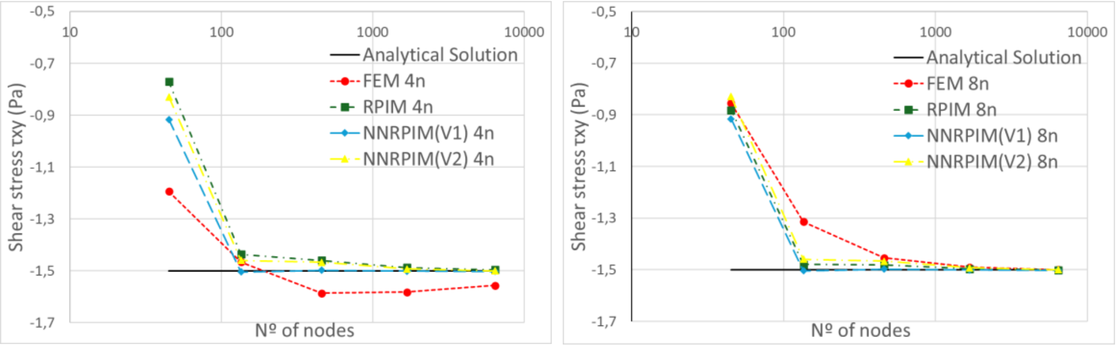

a) b)

Figure 25 - a) Shear stress (τ_{xy}) analysis results with 4-node tetrahedral elements mesh; b) Shear stress (τ_{xy}) analysis results with 8-node hexahedral elements mesh

Figure 26 showcases the analysis of the stress results, which were obtained in point C with coordinates (0.5;0.5;0). Again, in this analysis, all the methods show convergence for both meshes. However, the FEM with the 4-node tetrahedral elements mesh obtained values further away from the analytical solution when comparing it with the remaining methods.

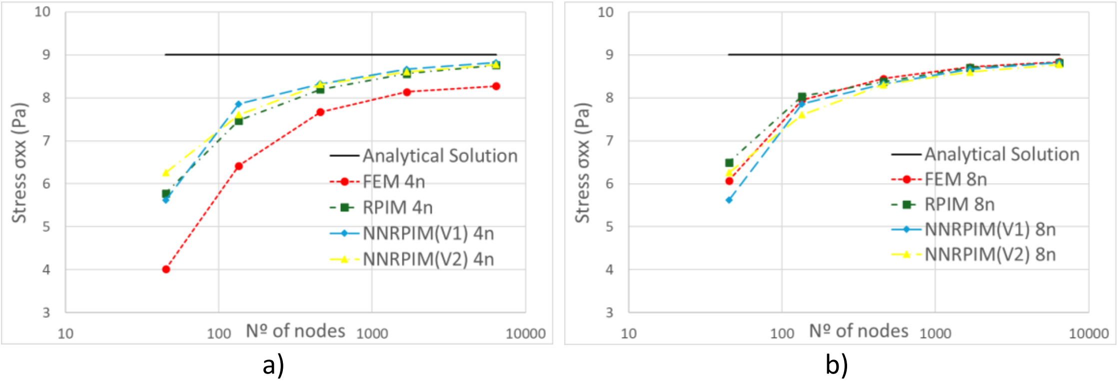

Figure 26 - a) Stress (σ_{xx}) analysis results with 4-node tetrahedral elements mesh; b) Stress (σ_{xx}) analysis results with 8-node hexahedral elements mesh

In Figure 27 to Figure 30 are presented the displacement (u), displacement (v), stress (σ_{xx}) and shear stress (τ_{xy}) colour maps, respectively, of all the methods for both meshes. Excluding the shear stress colour maps, all the others presented similar results that can hardly be noticed visually. For the shear stress, the colour maps are distinct from each other with the most different being the FEM analysis with 4-node tetrahedral elements mesh.

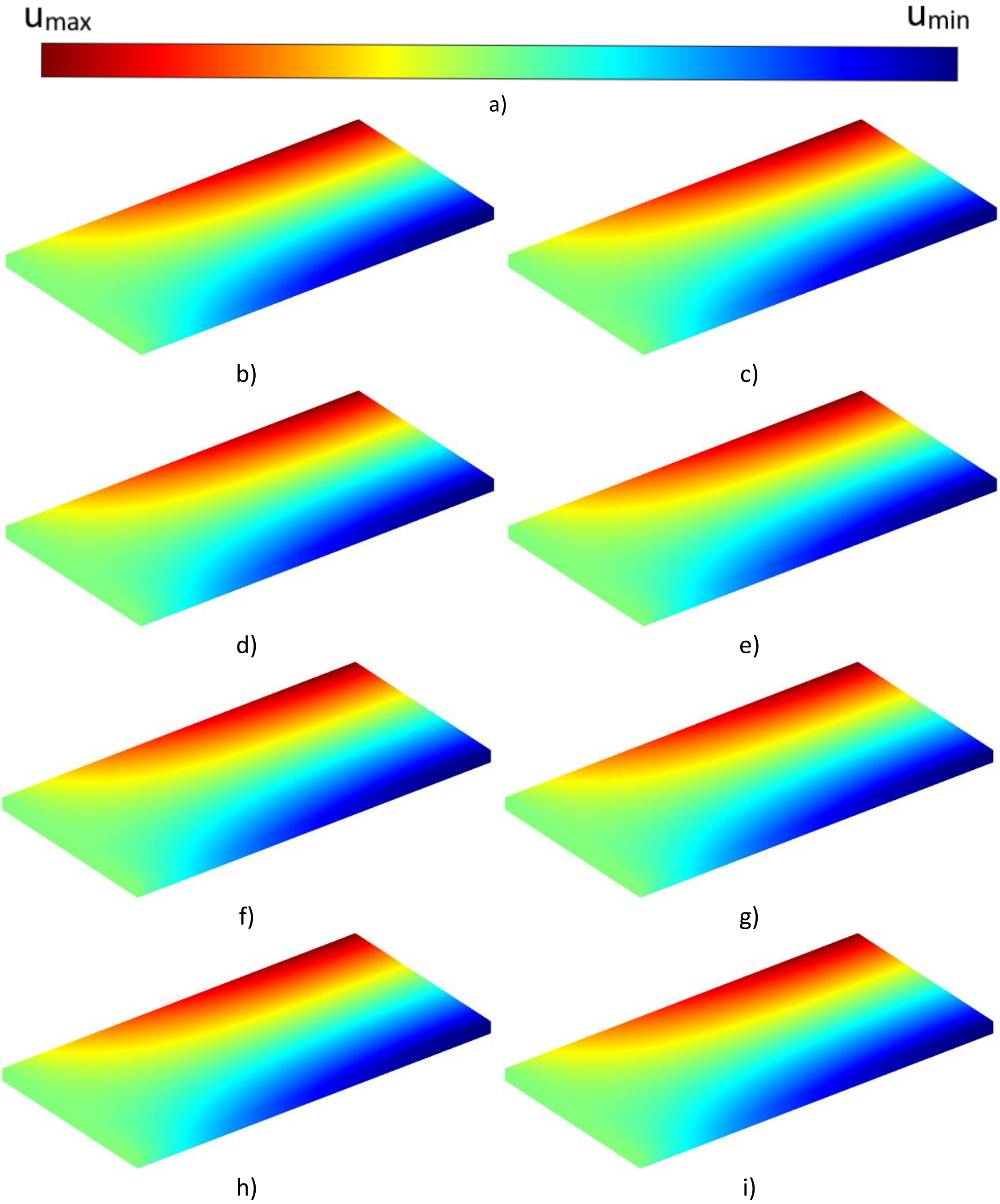

Figure 27 – a) Colour bar for u results b) FEM 4n (u_{max}= 0.0124 m u_{min}= -0.0124 m); c) FEM 8n (u_{max}= 0.0124 m u_{min}= -0.0124 m); d) RPIM 4n (u_{max}= 0.0124 m u_{min}= -0.0124 m); e) RPIM 8n (u_{max}= 0.0124 m u_{min}= -0.0124 m); f) NNRPIM(V1) 4n (u_{max}= 0.0124 m u_{min}= -0.0124 m); g) NNRPIM(V1) 8n (u_{max}= 0.0124 m u_{min}= -0,0124 m); h) NNRPIM(V2) 4n (u_{max}= 0.0124 m u_{min}= -0.0124 m); i) NNRPIM(V2) 8n (u_{max}= 0.0124 m u_{min}= -0.014 m)

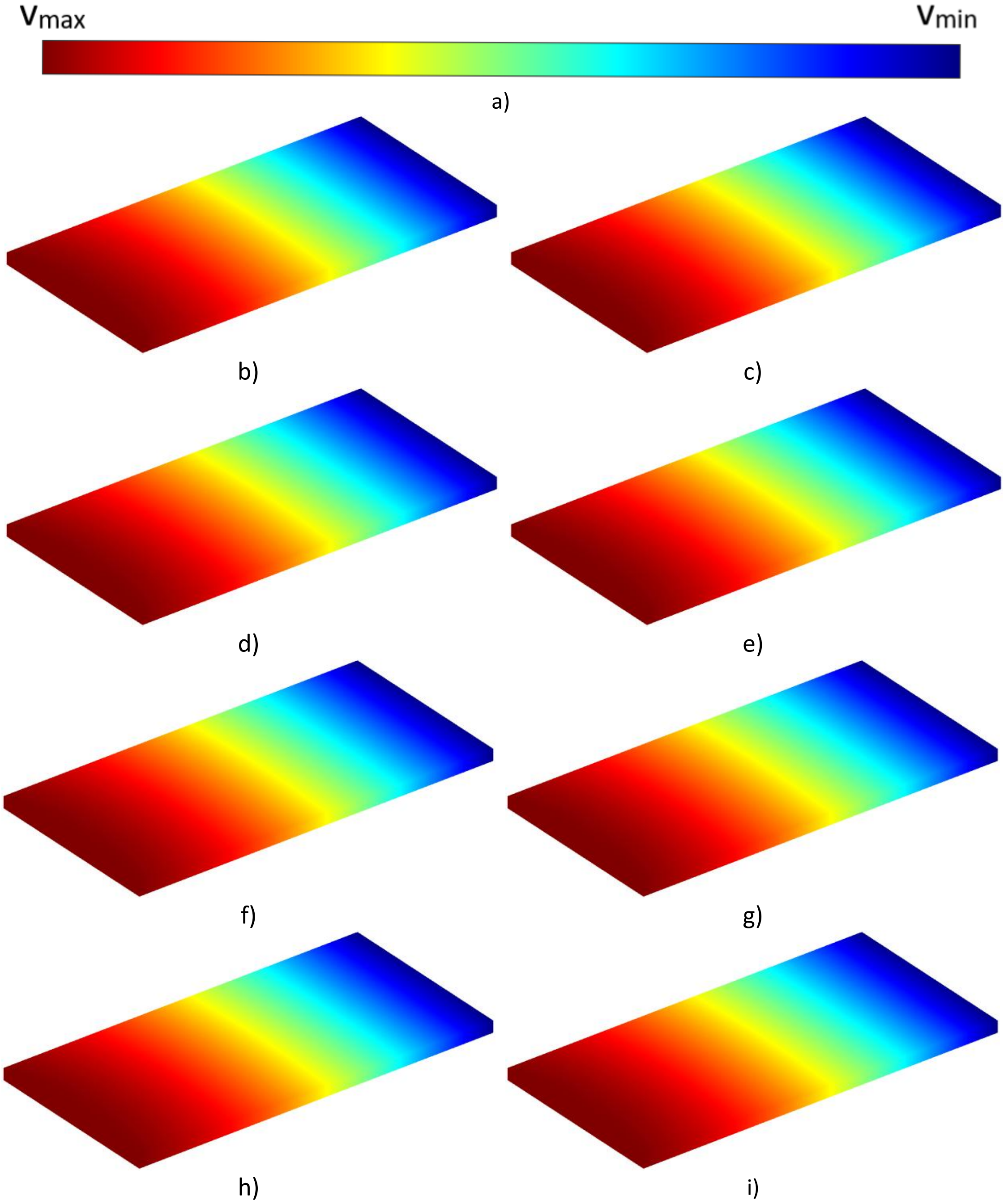

Figure 28 – a) Colour bar for v results b) FEM 4n (v_{max}= 0 m v_{min}= -0.0383 m); c) FEM 8n (v_{max}= 0 m v_{min}= -0.0381 m); d) RPIM 4n (v_{max}= 0 m v_{min}= -0.0381 m); e) RPIM 8n (v_{max}= 0 m v_{min}= -0.0381 m); f) NNRPIM(V1) 4n (v_{max}= 0 m u_{min}= -0.0381 m); g) NNRPIM(V1) 8n (v_{max}= 0 m v_{min}= -0.0381 m); h) NNRPIM(V2) 4n (v_{max}= 0 m v_{min}= -0.0381 m); i) NNRPIM(V2) 8n (v_{max}= 0 m v_{min}= -0.0381 m)

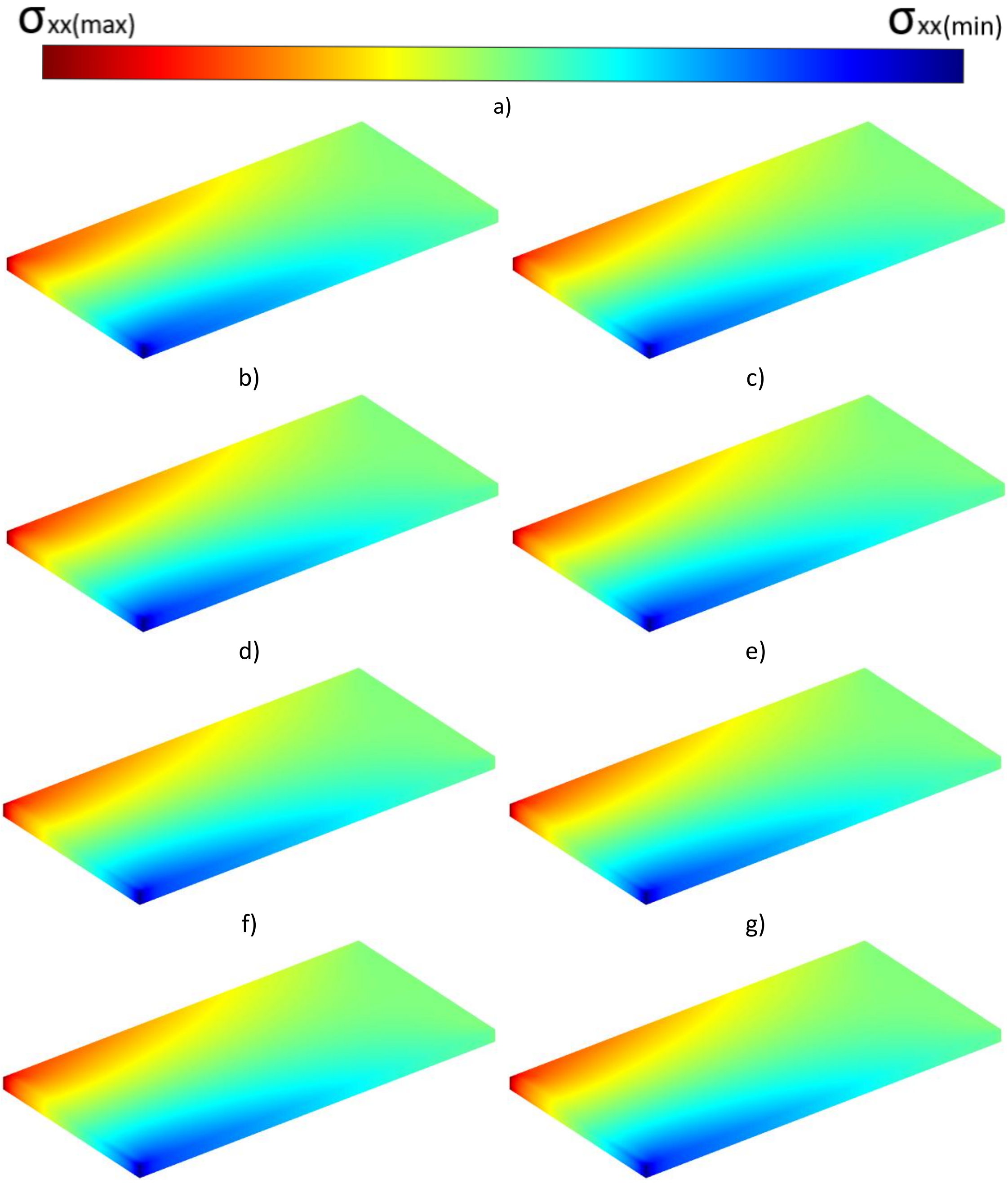

a)

b)

c)

d)

e)

f)

g)

h)

i)

Figure 29 – a) Colour bar for σ_{xx} results b) FEM 4n ($\sigma_{xx\,max}$= 16.5245 Pa $\sigma_{xx\,min}$= -16.5245 Pa); c) FEM 8n ($\sigma_{xx\,max}$= 18.1344 Pa $\sigma_{xx\,min}$= -18.1344 Pa); d) RPIM 4n ($\sigma_{xx\,max}$= 16.9997 Pa $\sigma_{xx\,min}$= -16.9989 Pa); e) RPIM 8n ($\sigma_{xx\,max}$= 17.5195 Pa $\sigma_{xx\,min}$= -17.5274 Pa); f) NNRPIM(V1) 4n ($\sigma_{xx\,max}$= 17.7289 Pa $\sigma_{xx\,min}$= -17.7289 Pa); g) NNRPIM(V1) 8n ($\sigma_{xx\,max}$= 17.7289 Pa $\sigma_{xx\,min}$= -17.7289 Pa); h) NNRPIM(V2) 4n ($\sigma_{xx\,max}$= 17.6914 Pa $\sigma_{xx\,min}$= -17.6914 Pa); i) NNRPIM(V2) 8n ($\sigma_{xx\,max}$= 17.6913 Pa $\sigma_{xx\,min}$= -17.6913 Pa)

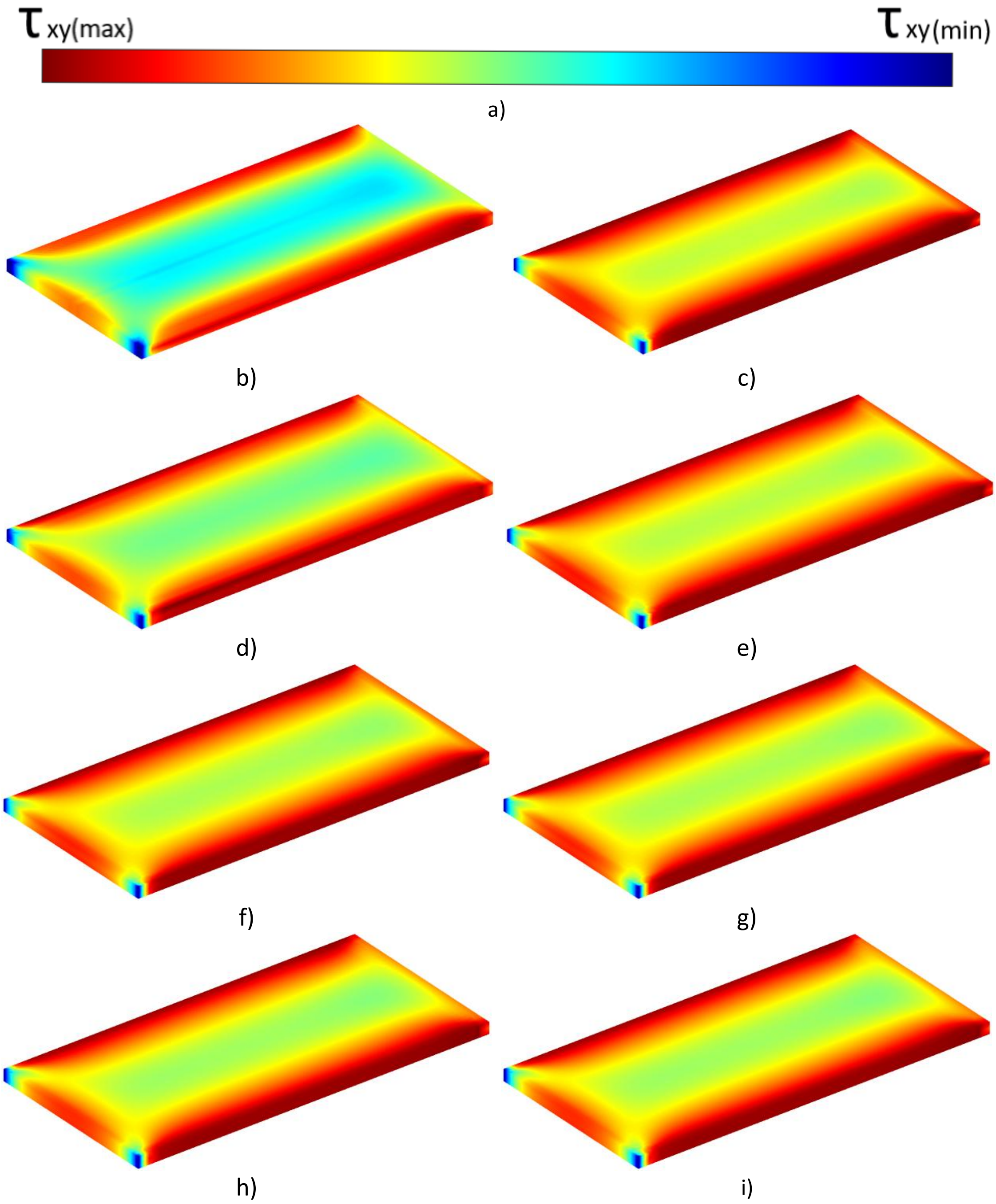

a)

b)

c)

d)

e)

f)

g)

h)

i)

Figure 30 – a) Colour bar for τ_{xy} results b) FEM 4n ($\tau_{xy\,max}$= 0.0498 Pa $\tau_{xy\,min}$= -2.4062 Pa); c) FEM 8n ($\tau_{xy\,max}$= -0.0389 Pa $\tau_{xy\,min}$= -3.4088 Pa); d) RPIM 4n ($\tau_{xy\,max}$= 0.1541 Pa $\tau_{xy\,min}$= -3.0712 Pa); e) RPIM 8n ($\tau_{xy\,max}$= 0.0473 Pa $\tau_{xy\,min}$= -3.4525 Pa); f) NNRPIM(V1) 4n ($\tau_{xy\,max}$= 0.0511 Pa $\tau_{xy\,min}$= -3.3705 Pa); g) NNRPIM(V1) 8n ($\tau_{xy\,max}$= 0.0511 Pa $\tau_{xy\,min}$= -3.3705 Pa); h) NNRPIM(V2) 4n (u_{max}= 0.0061 Pa u_{min}= -3.2150 Pa); i) NNRPIM(V2) 8n ($\tau_{xy\,max}$= 0.0061 Pa $\tau_{xy\,min}$= -3.2149 Pa)

6.3. Remodelling analyses

The analyses presented in this section are performed over a 2D beam with a length (L) of 0.6 m and a width (D) of 0.2 m. For the beam's elastic constants, the properties of the EN AW-6060 T66 aluminium alloy it were selected, with Young's modulus (E) of 70 GPa, Poisson's ratio (υ) of 0.3, and Yield strength (σ_{ced}) of 150 MPa [62]. The beam is constrained along its left side, and a force (F) of 3 kN is applied on its right side at its half height, as shown in Figure 31. Were used 3 distinct 4-node quadrangular element meshes, as exemplified in Figure 32, differing only in the number of divisions, as presented in Table 7. For the bone remodelling analyses, the Belinha material law and the effective von Mises stress optimal criterion were used. The maximum times a point can remodel were considered 2, and the stop criterion was 38% the initial mass (m_i). For comparison, a structural topology optimization algorithm was also used, employing the hard kill material law and the effective von Mises stress optimal criterion. In this algorithm, the maximum times a point could remodel was 9, and the stop criterion was also 38% the m_i. The growth rate (α) was defined as 0 for all the analyses, and for the decrease ratio (β), 3 different values were used: 0.01, 0.02, and 0.05. The analyses were performed using all the methods shown in the previous sections being them the FEM, the RPIM, the NNRPIM(V1) and the NNRPIM(V2), making this a total of 72 analyses. The selected results have a final mass of around 45% m_i or, in case of impossibility to reach 45% m_i, the most correct assumed result is presented. The results are then compared with the solutions presented in Figure 33 by M.P. Bendsøe [61].

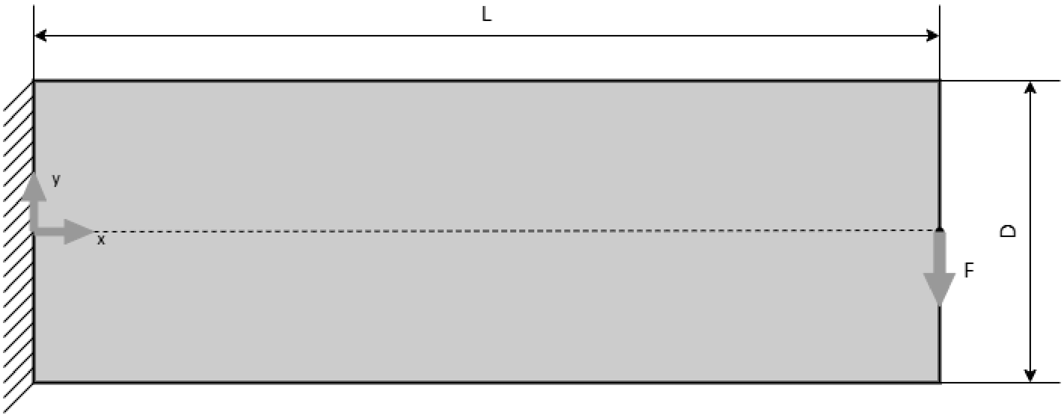

Figure 31 – Illustration of the 2D beam for the remodelling analyses

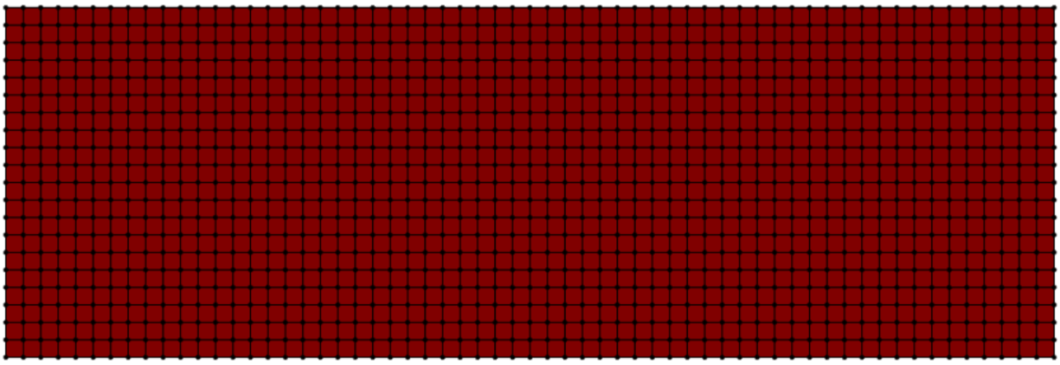

Figure 32 – 4 node triangular element mesh

Table 7 – Divisions and number of nodes of each mesh

x-axis divisions	y-axis divisions	number of nodes	designation
60	20	1281	M60x20
90	30	2821	M90x30
120	40	4961	M120x40

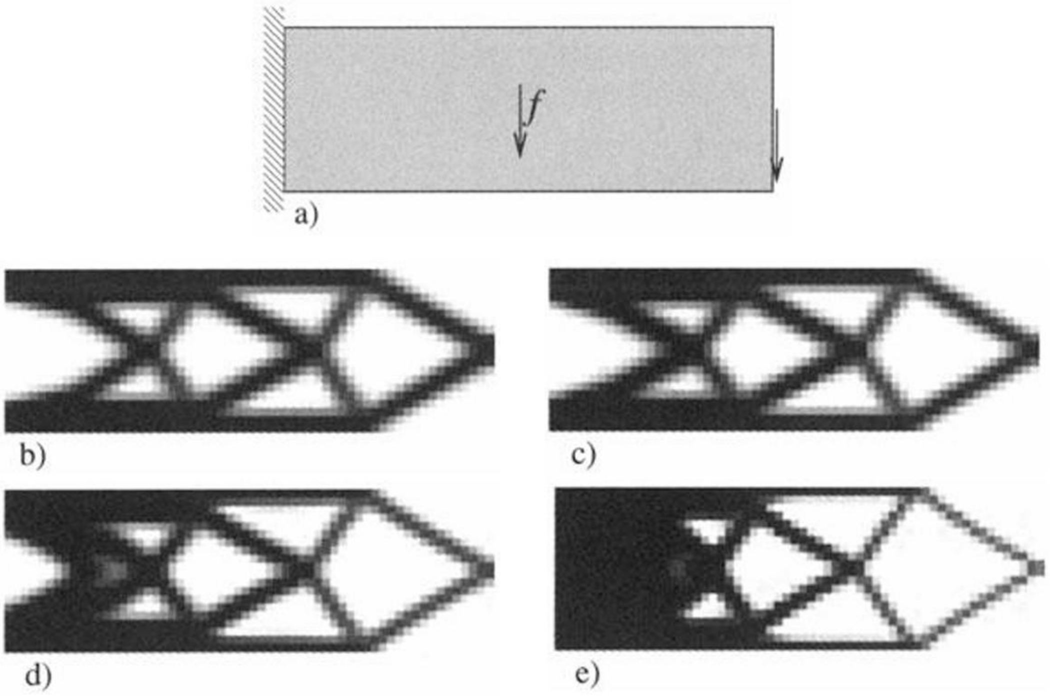

Figure 33 - Solution presented by M.P. Bendsøe [61]

Figure 34 to Figure 41 present the results obtained from the analysis using both Bone Remodelling (Figure 34 to Figure 37) and Structural Optimization (Figure 38 to Figure 41) processes. The two methods yielded different results, with the Structural Optimization results being closer to those presented by M.P. Bendsøe [61]Figure 33. However, using the Structural Optimization method showed to be impossible to use for the majority of analyses using FEM and RPIM, where the final mass normally only reached to around 80% m_i, distant from the 45% early defined. The Bone Remodelling method returned results for all of the methods and all of the decrease ratios (β) used, showing a tendency to obtain better results for higher decrease ratios – which also decreases the process time since a greater quantity of mass is being reduced for each iteration. As expected, the results are better if the mesh has more divisions.

For the structural optimization using FEM and RPIM, there is a criterion for the reinforcement of the model that occurs every 10 iterations. In order to test this criterion, the same analysis was run changing the reinforcement form every 10 iterations to every 15 iterations, obtaining the results presented in Figure 42 and Figure 43.

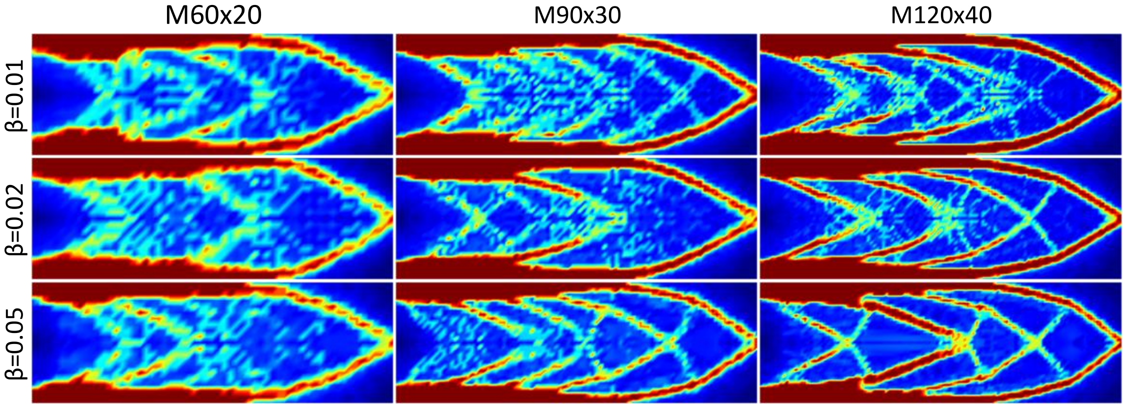

Figure 34 - Bone remodelling using FEM

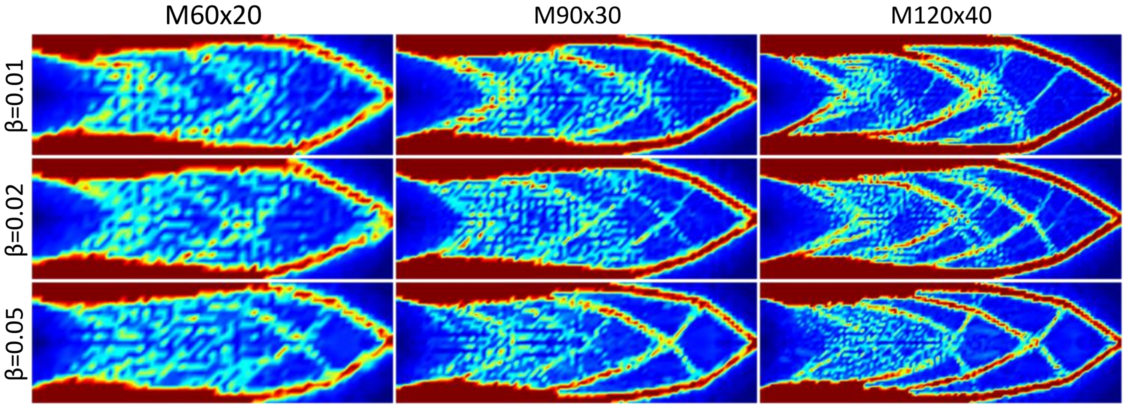

Figure 35 - Bone remodelling using RPIM

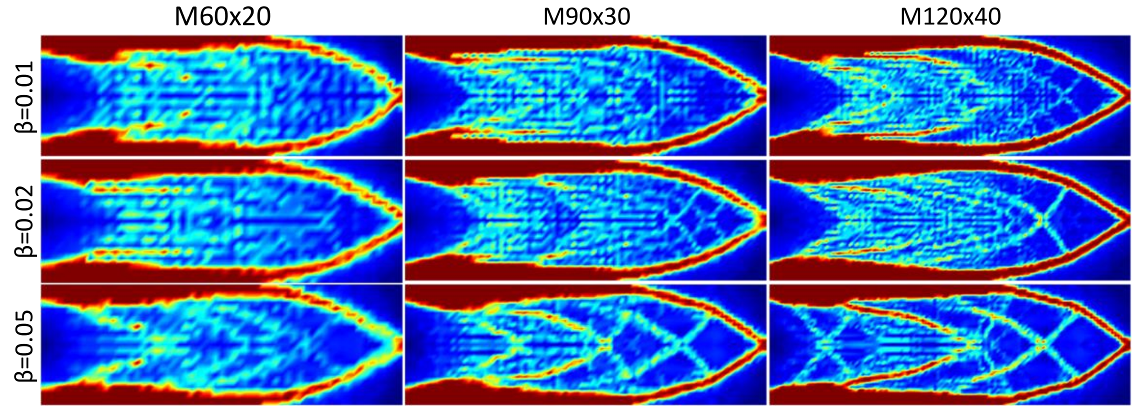

Figure 36 - Bone remodelling using NNRPIM(V1)

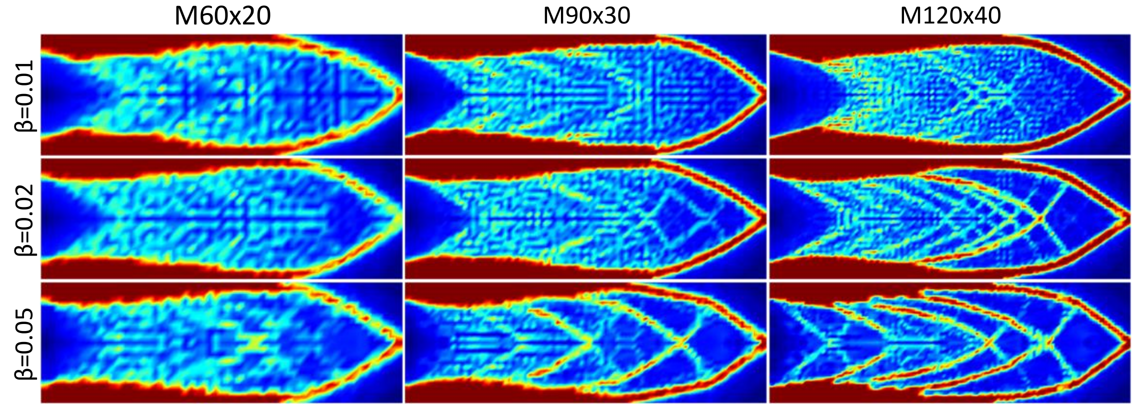

Figure 37 - Bone remodelling using NNRPIM(V2)

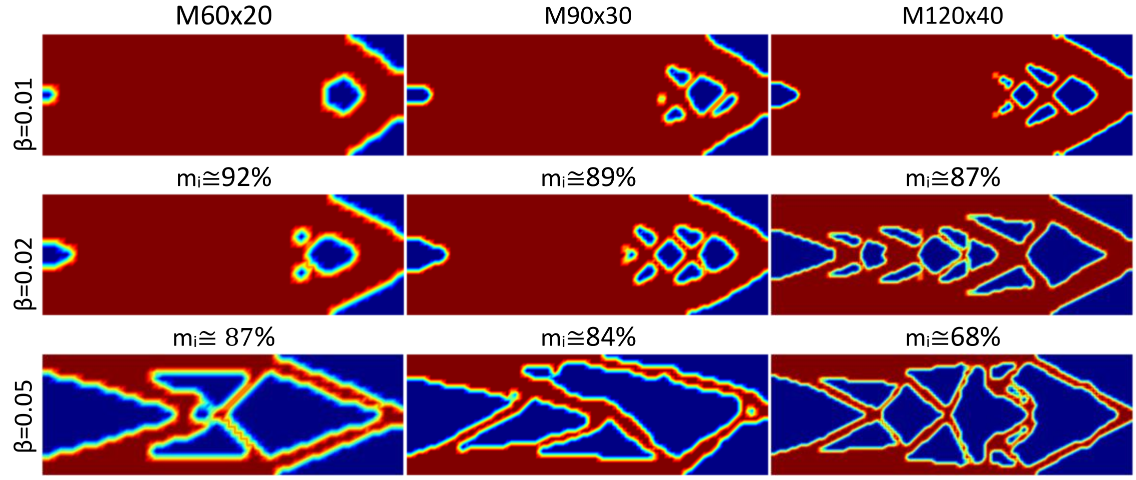

Figure 38 – Structural optimization using FEM

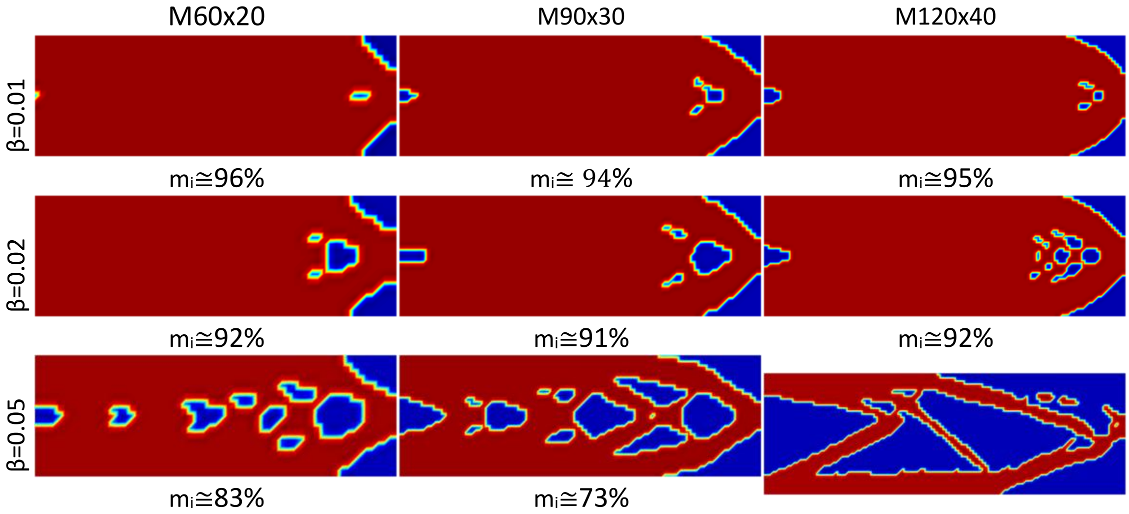

Figure 39 - Structural optimization RPIM

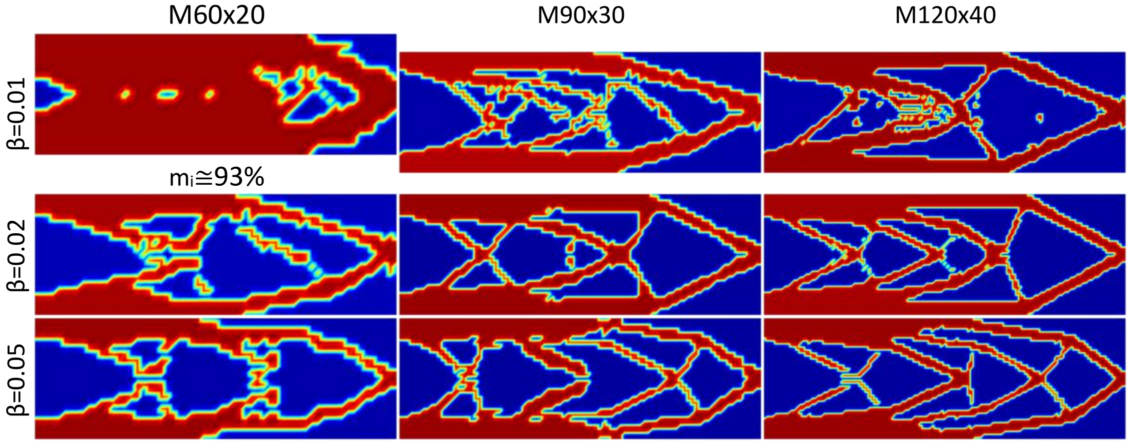

Figure 40 - Structural optimization using NNRPIM(V1)

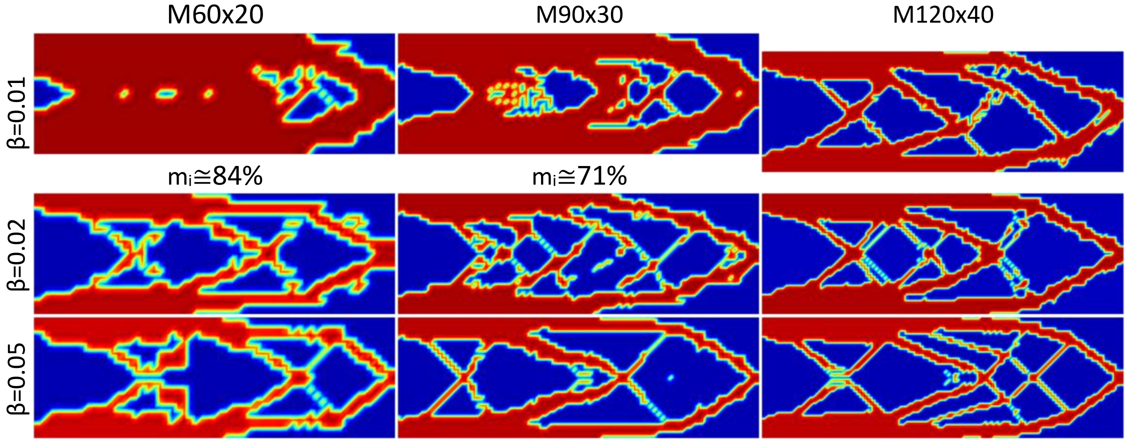

Figure 41 - Structural optimization using NNRPIM(V2)

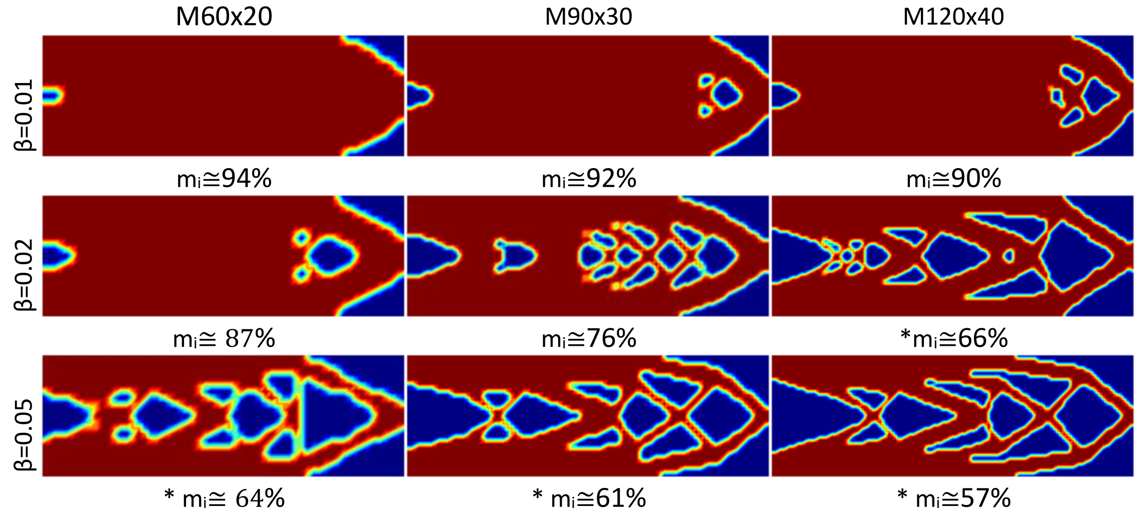

Figure 42 - Structural optimization using FEM with reinforcement every 15 iterations

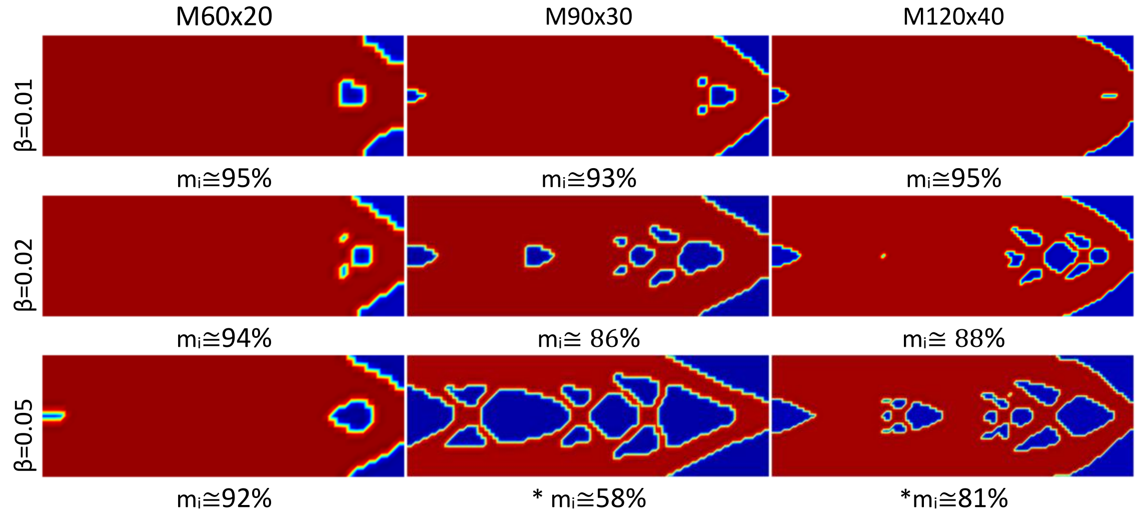

Figure 43 - Structural optimization using RPIM with reinforcement every 15 iterations

Some of the results obtained in the remodelling analyses were further investigated. The beam models were redesigned using the software FEMAP, using the coordinates obtained in FEMAS and ensuring that the area of the model ≈50% of the initial area (A_i). Figure 44 shows the distribution of the effective von Mises stress across the new beam models. Additionally, the beam's stiffness (k) was calculated as:

$$k = \frac{F}{\delta} \tag{49}$$

Being F the applied force and δ the displacement produced by the force. Figure 45 shows the displacement distribution across the redesigned models, and Table 8 presents the stiffness of each model.

The results shown in Figure 44 and Figure 45 were obtained for 5 different beam designs and computed using the FEM, the RPIM and the NNRPIM(V2).

Table 8 - Obtained stiffness for the different models. “BR” stands for the results using the “Bone Remodelling” algorithm, while “SO” stands for results using the “Structural Optimization Algorithm”

Stiffness [kN/mm]	FEM	NNRPIM	RPIM
FEM_BR	399.88	399.73	397.95
FEM_SO	357.13	352.19	354.07
NNRPIM_BR	391.97	389.96	389.24
NNRPIM_SO	422.76	421.67	421.37
RPIM_BR	398.75	395.65	397.17

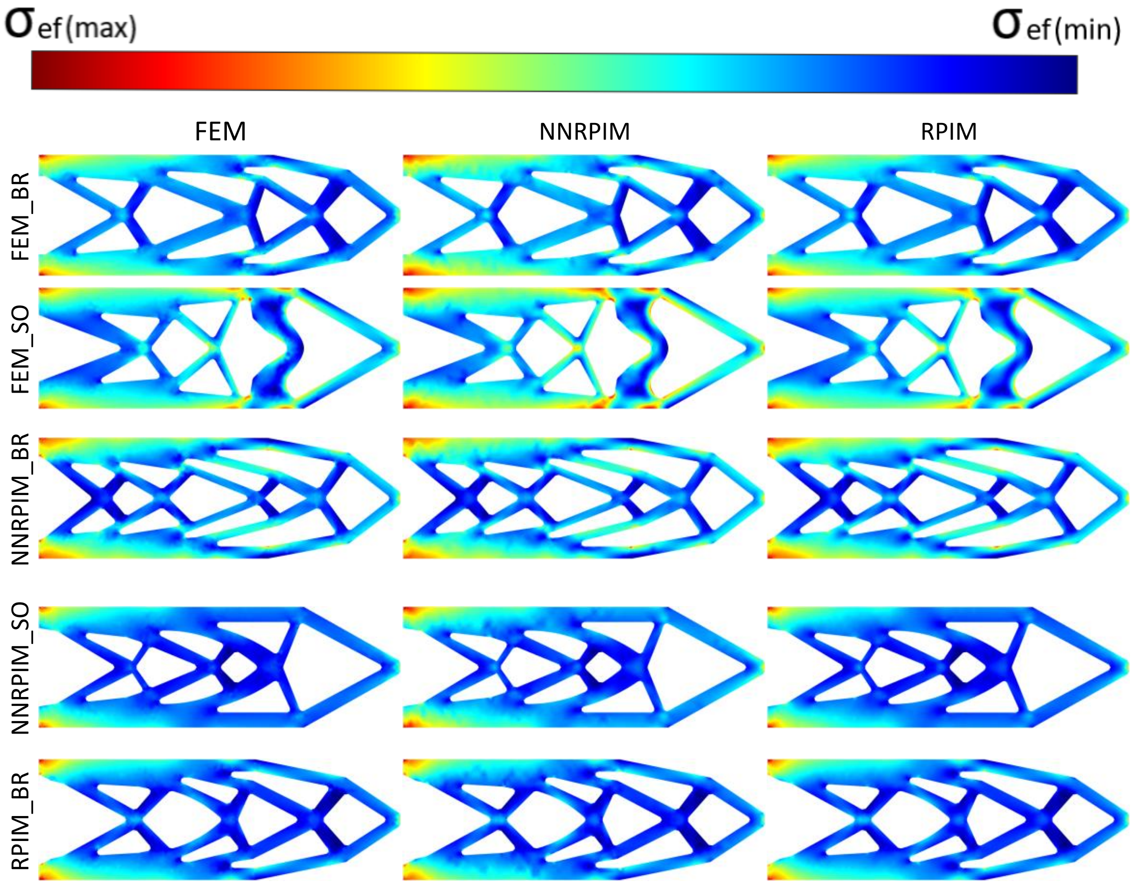

Figure 44 - FEM_BR/FEM) ($\sigma_{ef\ max}$= 494 kPa $\sigma_{ef\ min}$= 5 kPa); FEM_BR/NNRPIM) ($\sigma_{ef\ max}$= 439 kPa $\sigma_{ef\ min}$= 11 kPa); FEM_BR/RPIM) ($\sigma_{ef\ max}$= 480 kPa $\sigma_{ef\ min}$= 7 kPa); FEM_SO/FEM) ($\sigma_{ef\ max}$= 452 kPa $\sigma_{ef\ min}$= 11 kPa); FEM_SO/NNRPIM) ($\sigma_{ef\ max}$= 405 kPa $\sigma_{ef\ min}$= 9 kPa); FEM_SO/RPIM) ($\sigma_{ef\ max}$= 440 kPa $\sigma_{ef\ min}$= 8 kPa); NNRPIM_BR/FEM) ($\sigma_{ef\ max}$= 456 kPa $\sigma_{ef\ min}$= 11 kPa); NNRPIM_BR/NNRPIM) ($\sigma_{ef\ max}$= 454 kPa $\sigma_{ef\ min}$= 8 kPa); NNRPIM_BR/RPIM) ($\sigma_{ef\ max}$= 445 kPa $\sigma_{ef\ min}$= 9 kPa); NNRPIM_SO/FEM) ($\sigma_{ef\ max}$= 515 kPa $\sigma_{ef\ min}$= 32 kPa); NNRPIM_SO/NNRPIM) ($\sigma_{ef\ max}$= 455 kPa $\sigma_{ef\ min}$= 31 kPa); NNRPIM_BR/RPIM) ($\sigma_{ef\ max}$= 503 kPa $\sigma_{ef\ min}$= 34 kPa); RPIM_BR/FEM) ($\sigma_{ef\ max}$= 525 kPa $\sigma_{ef\ min}$= 30 kPa); RPIM_BR/NNRPIM) ($\sigma_{ef\ max}$= 528 kPa $\sigma_{ef\ min}$= 26 kPa); RPIM_BR/RPIM) ($\sigma_{ef\ max}$= 528 kPa $\sigma_{ef\ min}$= 25 kPa).

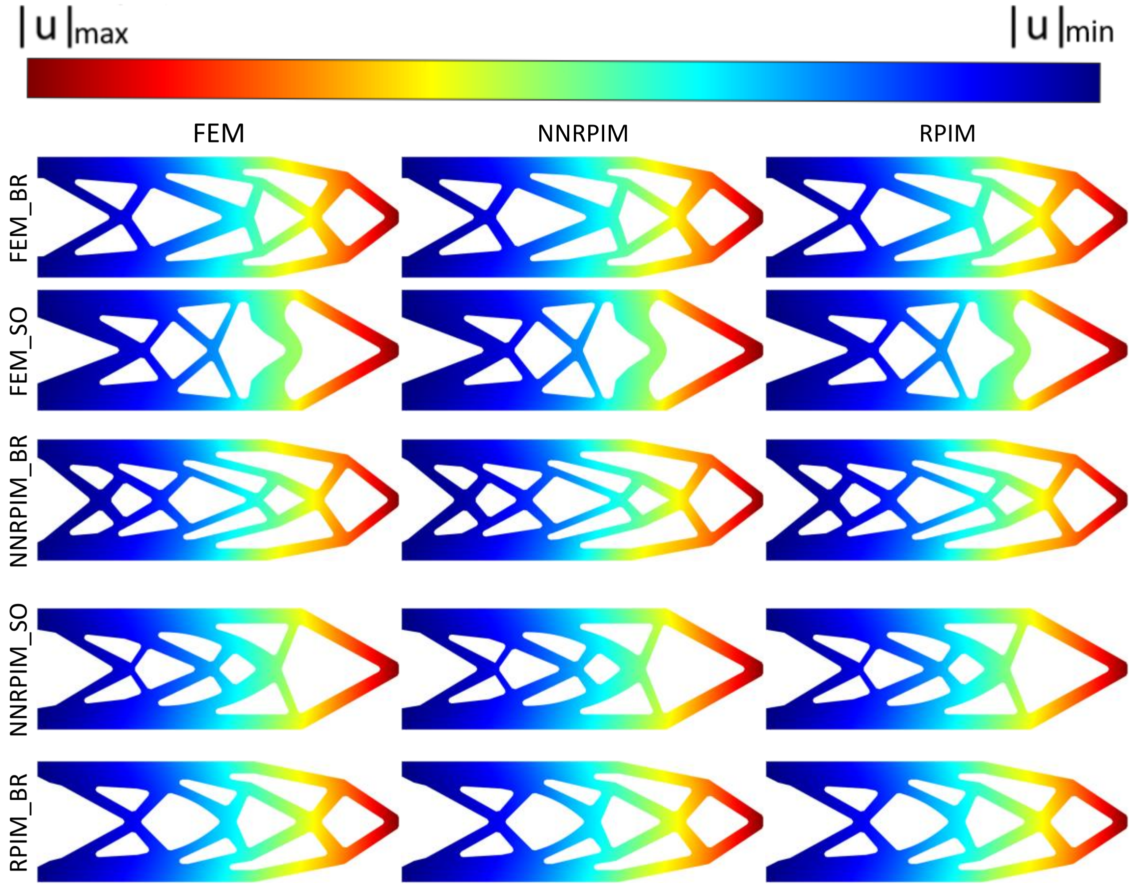

Figure 45 - FEM_BR/FEM) ($|u|_{max}$ = 7.502x10^{-3} mm $|u|_{min}$ = 0 mm); FEM_BR/NNRPIM) ($|u|_{max}$ = 7.505x10^{-3} mm $|u|_{min}$ = 0 mm); FEM_BR/RPIM) ($|u|_{max}$ = 7.539x10^{-3} mm $|u|_{min}$ = 0 mm); FEM_SO/FEM) ($|u|_{max}$ = 8.400x10^{-3} mm $|u|_{min}$ = 0 mm); FEM_SO/NNRPIM) ($|u|_{max}$ = 8.518x10^{-3} mm $|u|_{min}$ = 0 mm); FEM_SO/RPIM) ($|u|_{max}$ = 8.473x10^{-3} mm $|u|_{min}$ = 0 mm); NNRPIM_BR/FEM) ($|u|_{max}$ = 7.654x10^{-3} mm $|u|_{min}$ = 0 mm); NNRPIM_BR/NNRPIM) ($|u|_{max}$ = 7.693x10^{-3} mm $|u|_{min}$ = 0 mm); NNRPIM_BR/RPIM) ($|u|_{max}$ = 7.707x10^{-3} mm $|u|_{min}$ = 0 mm); NNRPIM_SO/FEM) ($|u|_{max}$ = 7.096x10^{-3} mm $|u|_{min}$ = 0 mm); NNRPIM_SO/NNRPIM) ($|u|_{max}$ = 7.115x10^{-3} mm $|u|_{min}$ = 0 mm); NNRPIM_BR/RPIM) ($|u|_{max}$ = 7.120x10^{-3} mm $|u|_{min}$ = 0 mm); RPIM_BR/FEM) ($|u|_{max}$ = 7.523x10^{-3} mm $|u|_{min}$ = 0 mm); RPIM_BR/NNRPIM) ($|u|_{max}$ = 7.582x10^{-3} mm $|u|_{min}$ = 0 mm); RPIM_BR/RPIM) ($|u|_{max}$ = 7.554x10^{-3} mm $|u|_{min}$ = 0 mm).

7. Rover Component Remodelling

In this chapter, the component of the Perseverance rover that connects the wheel to the suspension system (Figure 46) will be analysed. This component has a C shape in order to connect on top with the suspension and on the bottom with the wheel, leaving space for the wheel.

The problem will be approached in 2D and, in order to find an optimized solution, a model is created that allows free remodelling until a stable solution is reached. The designed 2D model is shown in Figure 47 a), being it constrained in the upper left corner, where the connection to the suspension system occurs and has a thickness of 86.6 mm. In the place where the component connects to the wheel, two loads (P1 and P2) are applied, P1 being the vertical load caused by supporting rover's weight, and P2 an axial load that could be caused in inclined surfaces were the rover is tilted to one of the sides. Taking into account the rover's weight of 1025 kg, and considering Earth's gravitational acceleration, where the rover was originally tested, if the weight is equally distributed among the 6 wheels, it is obtained a load of 1676 N per wheel. This is not always the case, so a force of 2000 N was chosen for the vertical load (P1) to allow for a margin for increased load. For the axial load (P2) was used a force = 10% P1 being it 200 N.

Regarding the mesh, using the FEMAP program, a model was created with 2 different patches, as shown in Figure 47 b), so that the area that connects to the wheel was not remodelled in the analysis. Triangular elements with size equals 8 mm were used, and the adopted material was the same as for the section 6.3, EN AW-6060 T66 aluminium alloy with Young's modulus (E) of 70 GPa, Poisson's ratio (υ) of 0.3, and Yield strength (σ_{ced}) of 150 MPa [62].

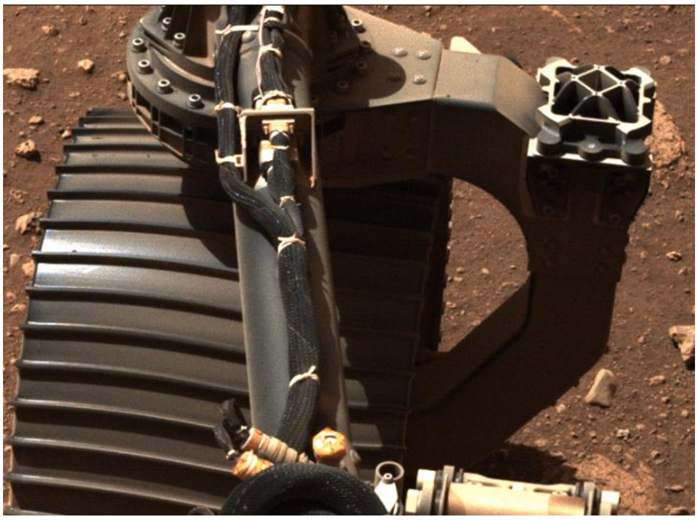

Figure 46 – Image from the component taken from the Navigation Cameras (Navcams), image from science.nasa.gov [63]

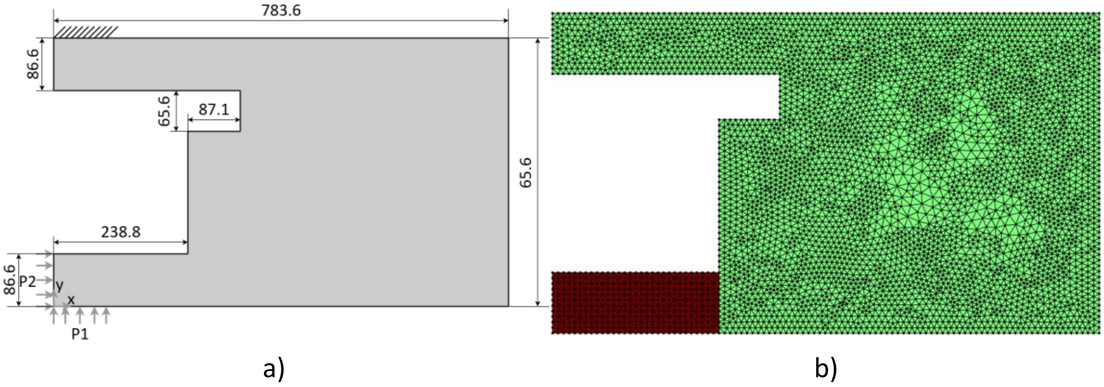

Figure 47 - a) Illustration of the 2D model; b) Model mesh

For the remodelling analyses, the Bone Remodelling and the Structural Optimization algorithms were used, combined with the FEM, RPIM and NNRPIM(V2). The parameters used in this analysis were the same as those described in section 6.3 with the exception of the stop ratio which was reduced to ≅ 30% m_i due to the use of a large remodelling area. The results are presented in Figure 48 where the remodelable area corresponds to ≅ 35% A_i for the Bone Remodelling algorithm and ≅ 20% A_i for the Structural Optimization algorithm. These values were adopted to obtain more detailed solutions for each method. The results presented are all very similar to each other, with the ones obtained from the Bone Remodelling having more bars between the two essential ones, farther left and farther right.

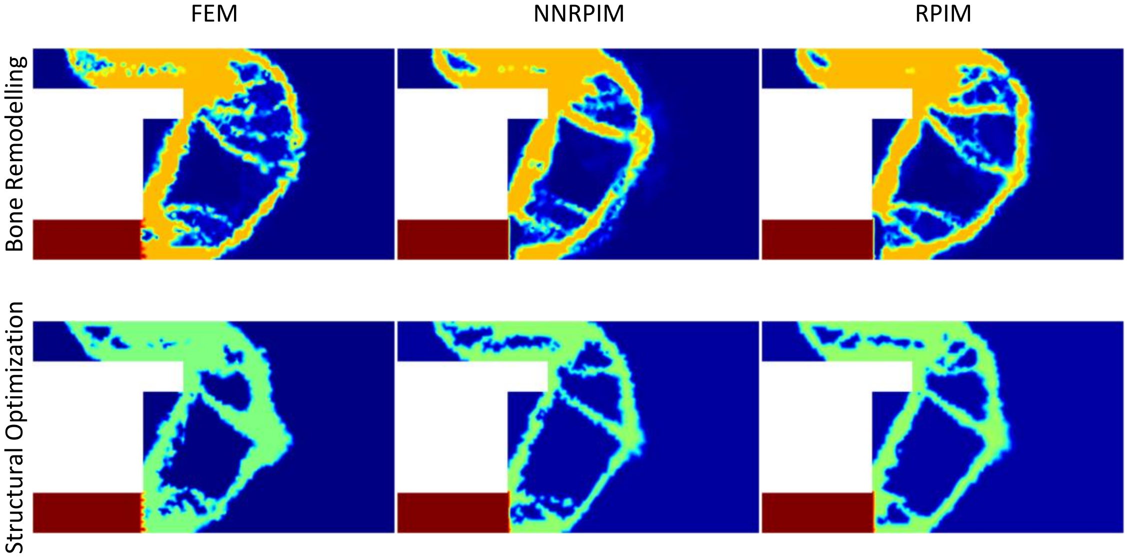

Figure 48 - Remodelling results

The obtained results, showcased in Figure 49 were then design in FEMAP in order to obtain models with a similar area (≈ 0.105 m^2) with a triangular mesh whose element size is 0.005 m. These models were analysed in order to select the best solution. The effective von Mises stress is shown in Figure 49 to Figure 51, and the stiffness (k) is calculated from the displacement analysis, shown in Figure 52 to Figure 54. Table 9 presents the stiffness results for the six redesigns, computed using the FEM, the RPIM and the NNRPIM(V2).

Table 9 - Obtained stiffness from the different models

Stiffness [kN/mm]	FEM	NNRPIM	RPIM
FEM_BR	8.92	8.64	8.66
FEM_SO	11.22	11.05	11.14
NNRPIM_BR	10.89	10.71	10.80
NNRPIM_SO	11.34	11.15	11.25
RPIM_BR	10.46	10.26	10.31
RPIM_SO	11.20	11.00	11.11

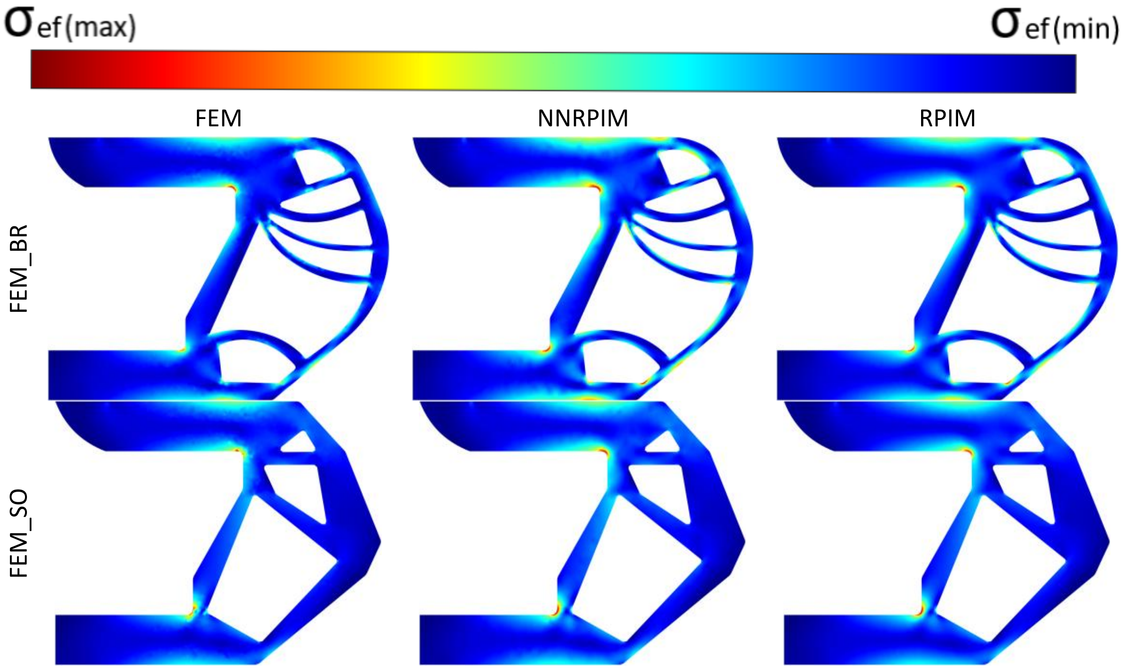

Figure 49 - von Mises effective stress for FEM models: FEM_BR/FEM) ($\sigma_{ef\ max}$= 8199 kPa $\sigma_{ef\ min}$= 11 kPa); FEM_BR/NNRPIM) ($\sigma_{ef\ max}$= 6834 kPa $\sigma_{ef\ min}$= 6 kPa); FEM_BR/RPIM) ($\sigma_{ef\ max}$= 7356 kPa $\sigma_{ef\ min}$= 6 kPa); FEM_SO/FEM) ($\sigma_{ef\ max}$= 7982 kPa $\sigma_{ef\ min}$= 20 kPa); FEM_SO/NNRPIM) ($\sigma_{ef\ max}$= 7552 kPa $\sigma_{ef\ min}$= 15 kPa); FEM_SO/RPIM) ($\sigma_{ef\ max}$= 7821 kPa $\sigma_{ef\ min}$= 18 kPa);

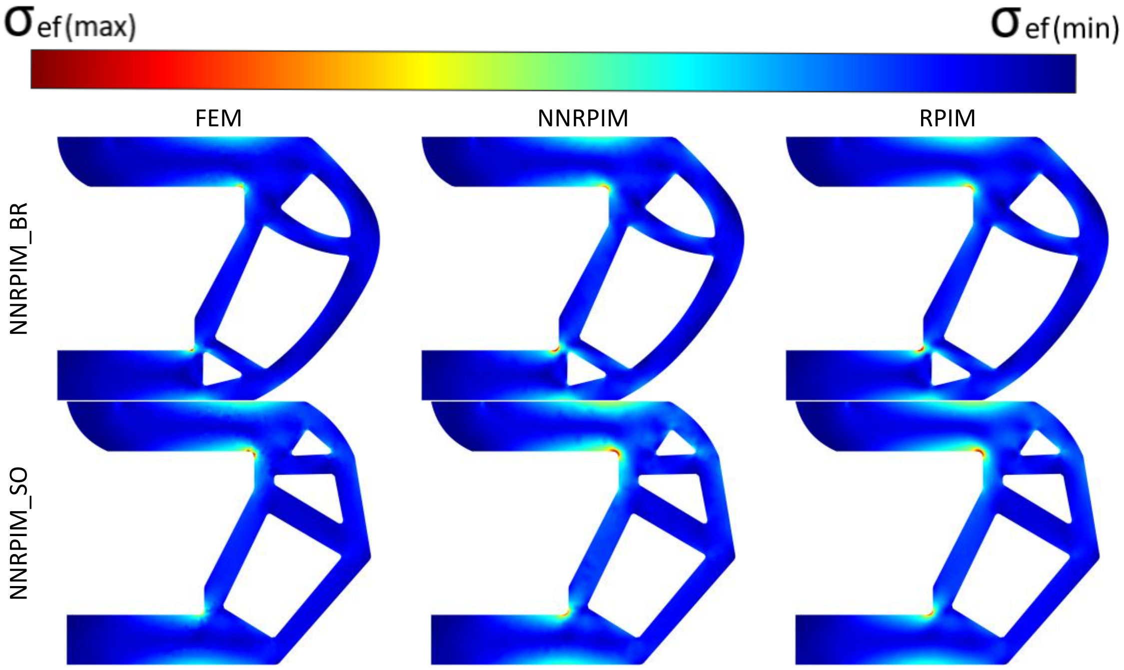

Figure 50 - von Mises effective stress for NNRPIM models: NNRPIM_BR/FEM) ($\sigma_{ef\ max}$= 10643 kPa $\sigma_{ef\ min}$= 12 kPa); NNRPIM_BR/NNRPIM) ($\sigma_{ef\ max}$= 8985 kPa $\sigma_{ef\ min}$= 15 kPa); NNRPIM_BR/RPIM) ($\sigma_{ef\ max}$= 8992 kPa $\sigma_{ef\ min}$= 14kPa); NRPIM_SO/FEM) ($\sigma_{ef\ max}$= 8479 kPa $\sigma_{ef\ min}$= 8 kPa); NNRPIM_SO/NNRPIM) ($\sigma_{ef\ max}$= 7226 kPa $\sigma_{ef\ min}$= 8 kPa); NNRPIM_SO/RPIM) ($\sigma_{ef\ max}$= 7382 kPa $\sigma_{ef\ min}$= 7 kPa);

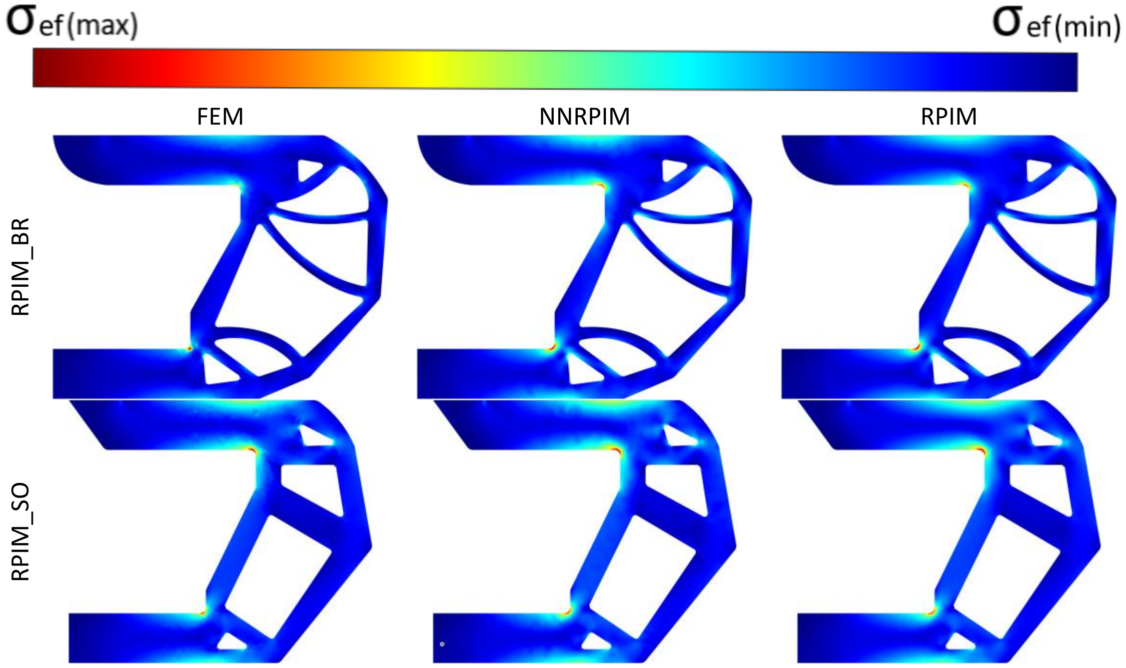

Figure 51 - von Mises effective stress for FEM models: FEM_BR/FEM) ($\sigma_{ef\ max}$= 10666 kPa $\sigma_{ef\ min}$= 20 kPa); FEM_BR/NNRPIM) ($\sigma_{ef\ max}$= 8614 kPa $\sigma_{ef\ min}$= 15 kPa); FEM_BR/RPIM) ($\sigma_{ef\ max}$= 8812 kPa $\sigma_{ef\ min}$= 14 kPa); FEM_SO/FEM) ($\sigma_{ef\ max}$= 7592 kPa $\sigma_{ef\ min}$= 6 kPa); FEM_SO/NNRPIM) ($\sigma_{ef\ max}$= 7291 kPa $\sigma_{ef\ min}$= 7 kPa); FEM_SO/RPIM) ($\sigma_{ef\ max}$= 7270 kPa $\sigma_{ef\ min}$= 7 kPa);

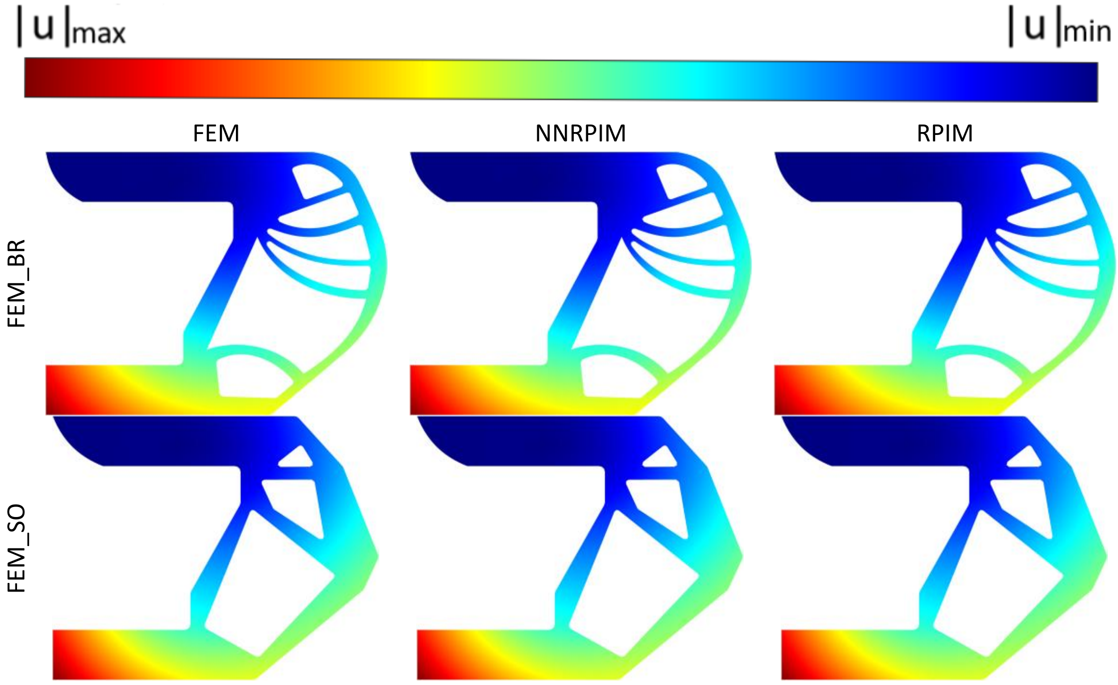

Figure 52 - Displacement for each FEM model: FEM_BR/FEM) ($|u|_{max}$ = 0.246 mm $|u|_{min}$ = 0 mm); FEM_BR/NNRPIM) ($|u|_{max}$ = 0.254 mm $|u|_{min}$ = 0 mm); FEM_BR/RPIM) ($|u|_{max}$ = 0.253 mm $|u|_{min}$= 0 mm); FEM_SO/FEM) ($|u|_{max}$ = 0.196 mm $|u|_{min}$ = 0 mm); FEM_SO/NNRPIM) ($|u|_{max}$ = 0.199 mm $|u|_{min}$ = 0 mm); FEM_SO/RPIM) ($|u|_{max}$ = 0.197 mm $|u|_{min}$ = 0 mm);

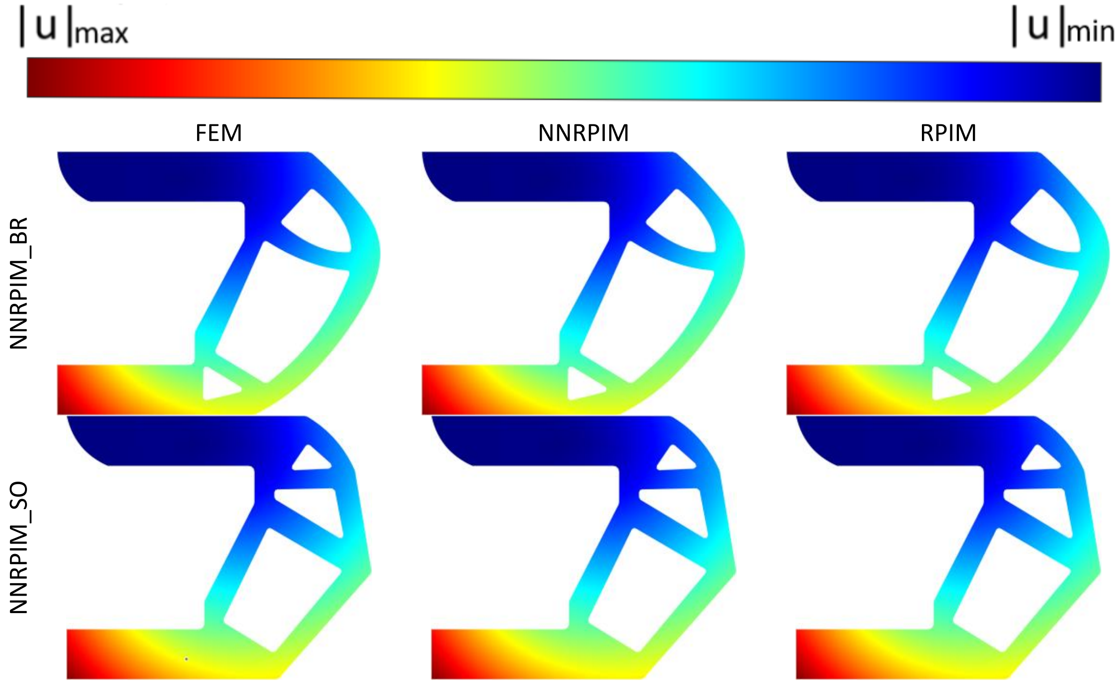

Figure 53 - Displacement for each NNRPIM model: NNRPIM_BR/FEM) ($|u|_{max}$ = 0.201 mm $|u|_{min}$ = 0 mm); NNRPIM _BR/NNRPIM) ($|u|_{max}$ = 0.205 mm $|u|_{min}$ = 0 mm); NNRPIM _BR/RPIM) ($|u|_{max}$ = 0.203 mm $|u|_{min}$= 0 mm); NNRPIM _SO/FEM) ($|u|_{max}$ = 0.194 mm $|u|_{min}$ = 0 mm); NNRPIM _SO/NNRPIM) ($|u|_{max}$ = 0.197 mm $|u|_{min}$ = 0 mm); NNRPIM _SO/RPIM) ($|u|_{max}$ = 0.195 mm $|u|_{min}$ = 0 mm);

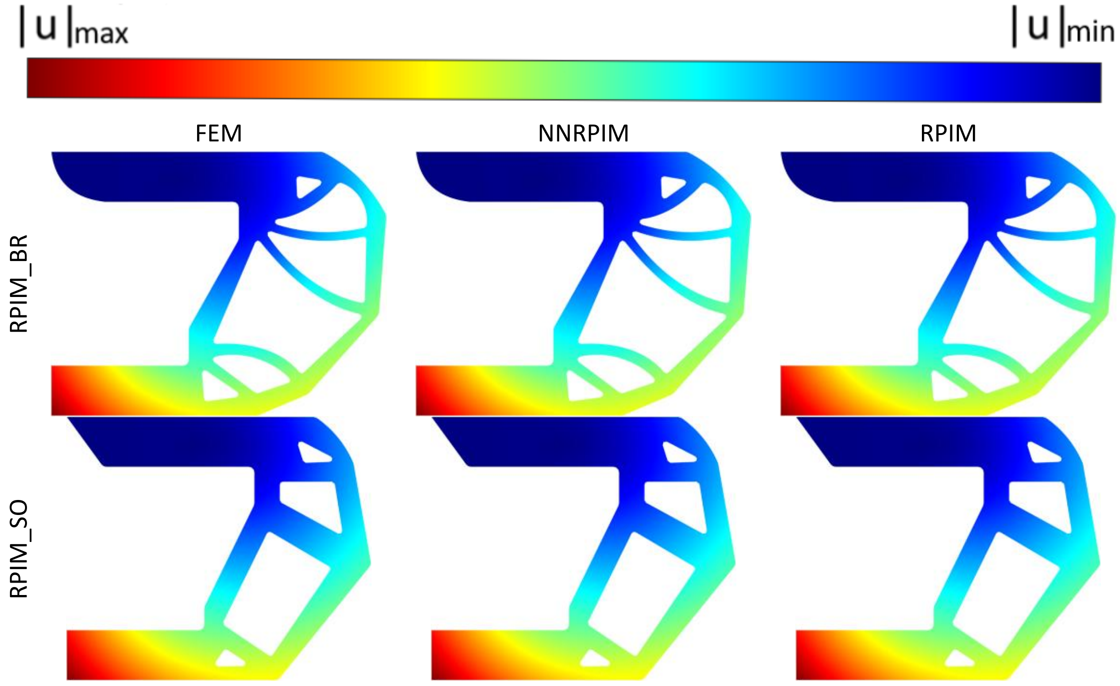

Figure 54 - Displacement for each RPIM model: RPIM_BR/FEM) ($|u|_{max}$ = 0.210 mm $|u|_{min}$ = 0 mm); RPIM _BR/NNRPIM) ($|u|_{max}$ = 0.214 mm $|u|_{min}$ = 0 mm); RPIM _BR/RPIM) ($|u|_{max}$ = 0.213 mm $|u|_{min}$= 0 mm); RPIM _SO/FEM) ($|u|_{max}$ = 0.196 mm $|u|_{min}$ = 0 mm); RPIM _SO/NNRPIM) ($|u|_{max}$ = 0.200 mm $|u|_{min}$ = 0 mm); RPIM _SO/RPIM) ($|u|_{max}$ = 0.197 mm $|u|_{min}$ = 0 mm);

To check for any improvements relatively to the original component, these results are then compared with similar metrics obtained from the analysis of the original component using the same material. To analyse it, a recreation of the design was done in 2D on FEMAP, using a similar mesh. Analogous to the previously presented results for the six redesigns, stiffness calculations are shown Table 10, using the displacement shown in Figure 55, and the results for the von Mises stress are shown in Figure 56. In order to compare the redesigned models with the original, since the 2D areas are different, the mass-normalized stiffness is calculated – Table 11.

With the obtained results, it is clear to see that the redesigned models present a higher stiffness than the original, with similar values of maximum von Mises stress although in less points than the original. Concluding, the developed models present a solution that reduces the displacement of the component, and present fewer spots where the component could fail due to stress concentration. On the other hand, the original component also fulfils the purpose of shock absorber, an objective that the developed models are not capable of fulfilling.

Table 10 - Stiffness

Stiffness [kN/mm]	FEM	NNRPIM	RPIM
Original Model	4.30	4.20	4.28

Table 11 – Mass normalized stiffness

Stiffness [N/mm/kg]	FEM	NNRPIM	RPIM
Original Model	210.74	205.86	209.51
FEM_BR	362.26	351.01	351.97
FEM_SO	460.76	453.87	457.27
NNRPIM_BR	446.51	438.97	442.59
NNRPIM_SO	462.76	455.01	459.27
RPIM_BR	422.75	414.65	416.73
RPIM_SO	457.87	449.44	454.06

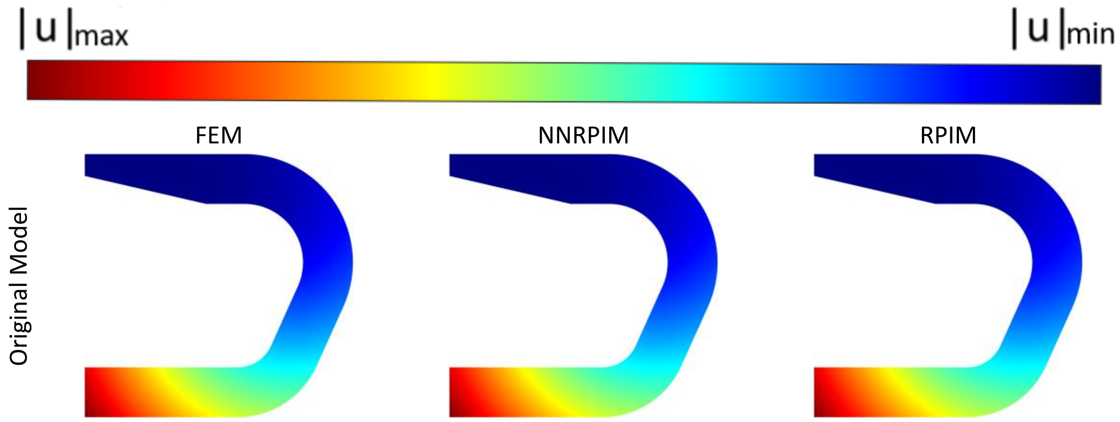

Figure 55 - Displacement for the original model: Original Model/FEM) ($|u|_{max}$ = 0.510 mm $|u|_{min}$ = 0 mm); Original Model /NNRPIM) ($|u|_{max}$ = 0.522 mm $|u|_{min}$ = 0 mm); Original Model /RPIM) ($|u|_{max}$ = 0.513 mm $|u|_{min}$= 0 mm);

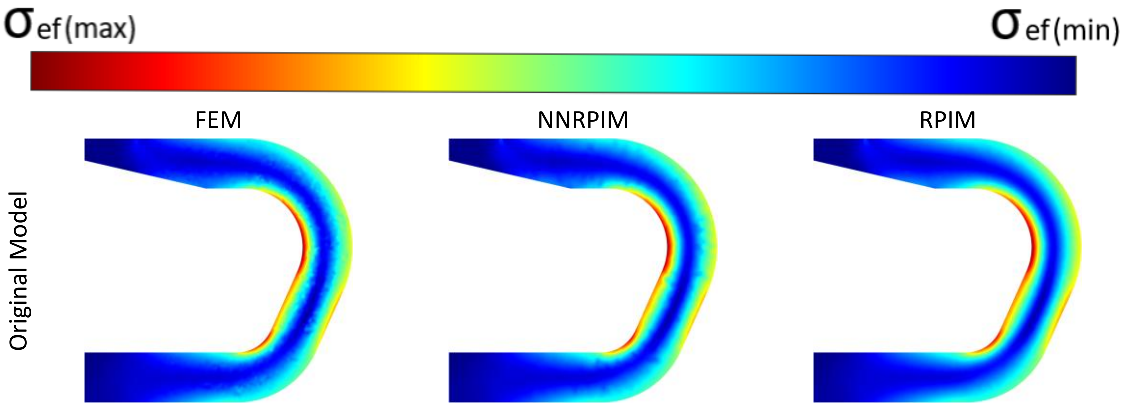

Figure 56 - Von Mises effective stress for the original model: Original Model/FEM) ($\sigma_{ef\ max}$= 8470 kPa $\sigma_{ef\ min}$= 4 kPa); Original Model /NNRPIM) ($\sigma_{ef\ max}$= 8555 kPa $\sigma_{ef\ min}$= 1 kPa); Original Model /RPIM) ($\sigma_{ef\ max}$= 8181 kPa $\sigma_{ef\ min}$= 1 kPa)

The original model and all the new models were also analysed in 3D, showing, as expected, similar results to the 2D analyses. In Table 12, the stiffness obtained from the displacement analysis (Figure 57 to Figure 60) it is shown. To better compare the models, it is utilized a mass-normalized stiffness shown in Table 13. The von Mises effective stress is also analysed with the results shown in Figure 61 to Figure 64.

Table 12 - Stiffness of the 3D models

Stiffness [kN/mm]	FEM	NNRPIM	RPIM
Original Model	4.52	4.29	4.27
FEM_BR	10.32	9.62	9.10
FEM_SO	11.98	11.52	11.45
NNRPIM_BR	11.62	11.20	11.13
NNRPIM_SO	12.02	11.54	11.55
RPIM_BR	11.47	10.88	10.63
RPIM_SO	11.93	11.55	11.49

Table 13 - Mass normalized stiffness of the 3D models

Stiffness [N/mm/kg]	FEM	NNRPIM	RPIM
Original Model	221.53	209.89	208.93
FEM_BR	419.26	390.90	369.85
FEM_SO	491.84	473.01	469.93
NNRPIM_BR	476.63	459.33	456.27
NNRPIM_SO	490.80	471.00	471.71
RPIM_BR	463.86	440.00	429.98
RPIM_SO	487.63	472.16	469.60

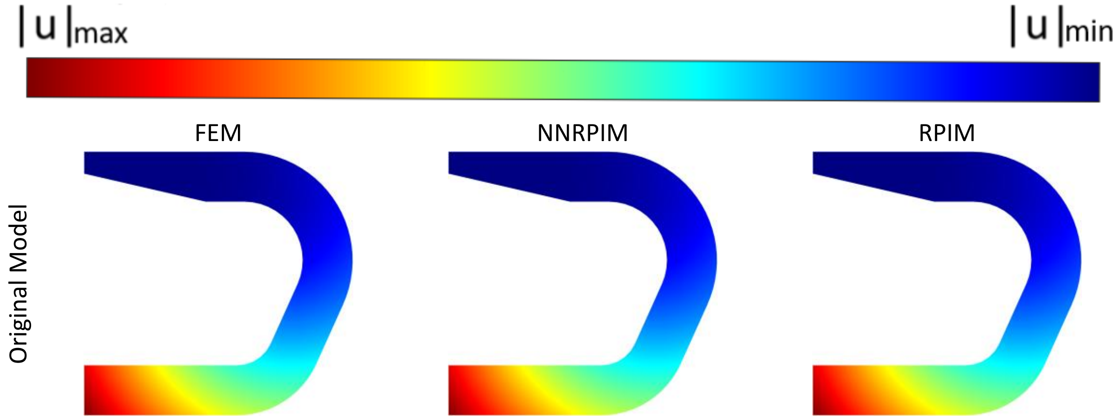

Figure 57 - Displacement for the 3D original model: Original Model/FEM) ($|u|_{max}$ = 0.483 mm $|u|_{min}$ = 0 mm); Original Model /NNRPIM) ($|u|_{max}$ = 0.510 mm $|u|_{min}$ = 0 mm); Original Model /RPIM) ($|u|_{max}$ = 0.512 mm $|u|_{min}$= 0 mm);

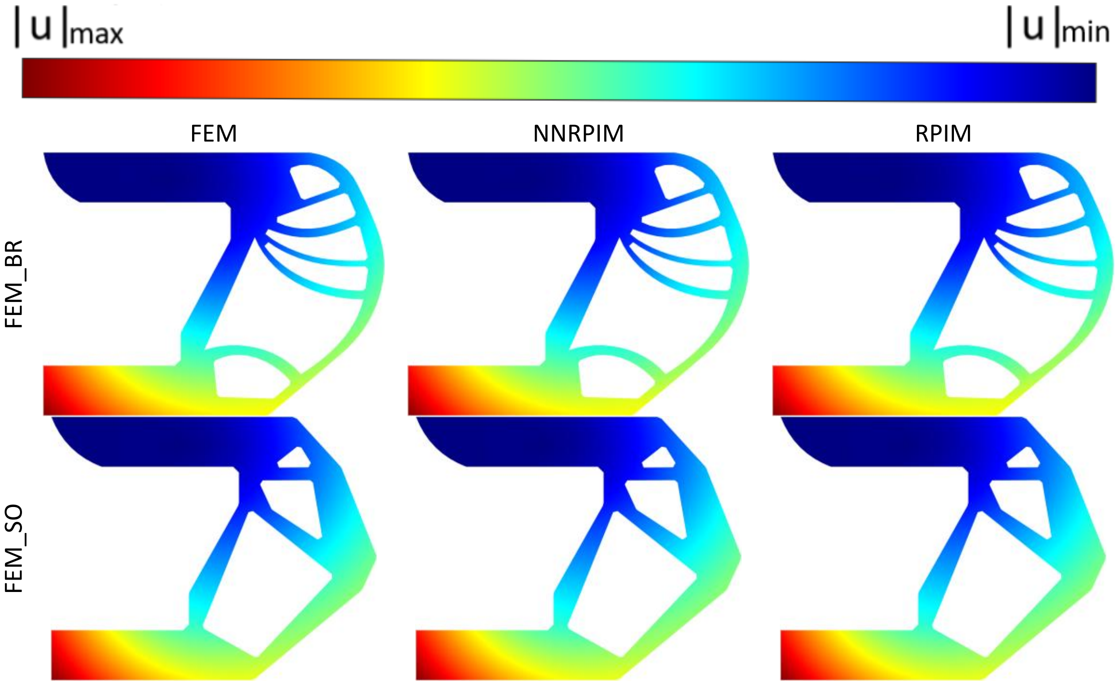

Figure 58 - Displacement for each 3D FEM model: FEM_BR/FEM) ($|u|_{max}$ = 0.212 mm $|u|_{min}$ = 0 mm); FEM_BR/NNRPIM) ($|u|_{max}$ = 0.227 mm $|u|_{min}$ = 0 mm); FEM_BR/RPIM) ($|u|_{max}$ = 0.240 mm $|u|_{min}$= 0 mm); FEM_SO/FEM) ($|u|_{max}$ = 0.182 mm $|u|_{min}$ = 0 mm); FEM_SO/NNRPIM) ($|u|_{max}$ = 0.190 mm $|u|_{min}$ = 0 mm); FEM_SO/RPIM) ($|u|_{max}$ = 0.191 mm $|u|_{min}$ = 0 mm);

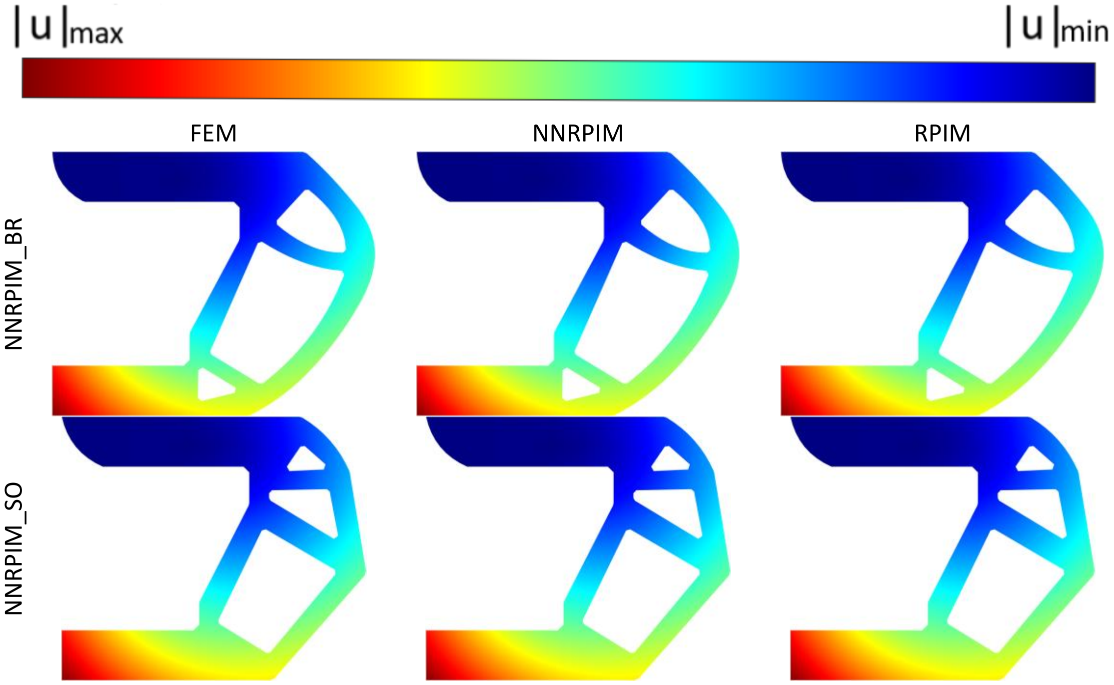

Figure 59 - Displacement for each 3D NNRPIM model: NNRPIM_BR/FEM) ($|u|_{max}$ = 0.188 mm $|u|_{min}$ = 0 mm); NNRPIM _BR/NNRPIM) ($|u|_{max}$ = 0.195 mm $|u|_{min}$ = 0 mm); NNRPIM _BR/RPIM) ($|u|_{max}$ = 0.196 mm $|u|_{min}$= 0 mm); NNRPIM _SO/FEM) ($|u|_{max}$ = 0.182 mm $|u|_{min}$ = 0 mm); NNRPIM _SO/NNRPIM) ($|u|_{max}$ = 0.189 mm $|u|_{min}$ = 0 mm); NNRPIM _SO/RPIM) ($|u|_{max}$ = 0.189 mm $|u|_{min}$ = 0 mm);

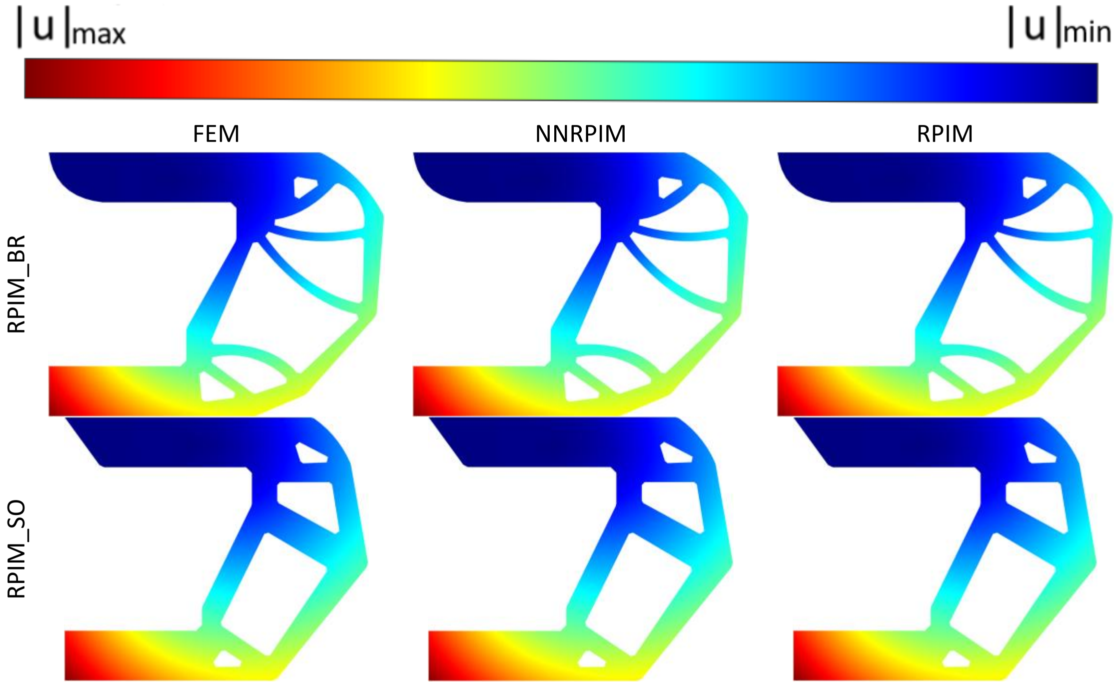

Figure 60 - Displacement for each 3D RPIM model: RPIM_BR/FEM) ($|u|_{max}$ = 0.190 mm $|u|_{min}$ = 0 mm); RPIM _BR/NNRPIM) ($|u|_{max}$ = 0.201 mm $|u|_{min}$ = 0 mm); RPIM _BR/RPIM) ($|u|_{max}$ = 0.205 mm $|u|_{min}$= 0 mm); RPIM _SO/FEM) ($|u|_{max}$ = 0.183 mm $|u|_{min}$ = 0 mm); RPIM _SO/NNRPIM) ($|u|_{max}$ = 0.189 mm $|u|_{min}$ = 0 mm); RPIM _SO/RPIM) ($|u|_{max}$ = 0.190 mm $|u|_{min}$ = 0 mm);

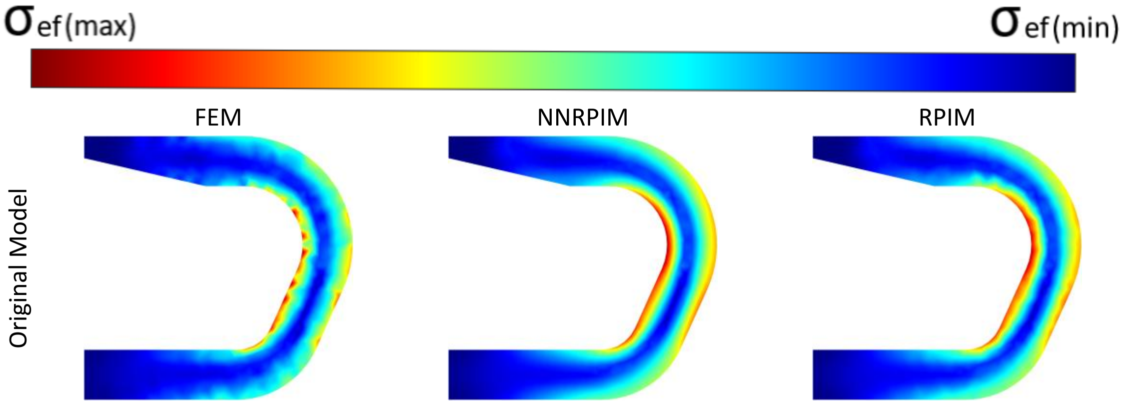

Figure 61 - Von Mises effective stress for the 3D original model: Original Model/FEM) ($\sigma_{ef\ max}$= 7650 kPa $\sigma_{ef\ min}$= 9 kPa); Original Model /NNRPIM) ($\sigma_{ef\ max}$= 7113 kPa $\sigma_{ef\ min}$= 7 kPa); Original Model /RPIM) ($\sigma_{ef\ max}$= 7117 kPa $\sigma_{ef\ min}$= 5 kPa)

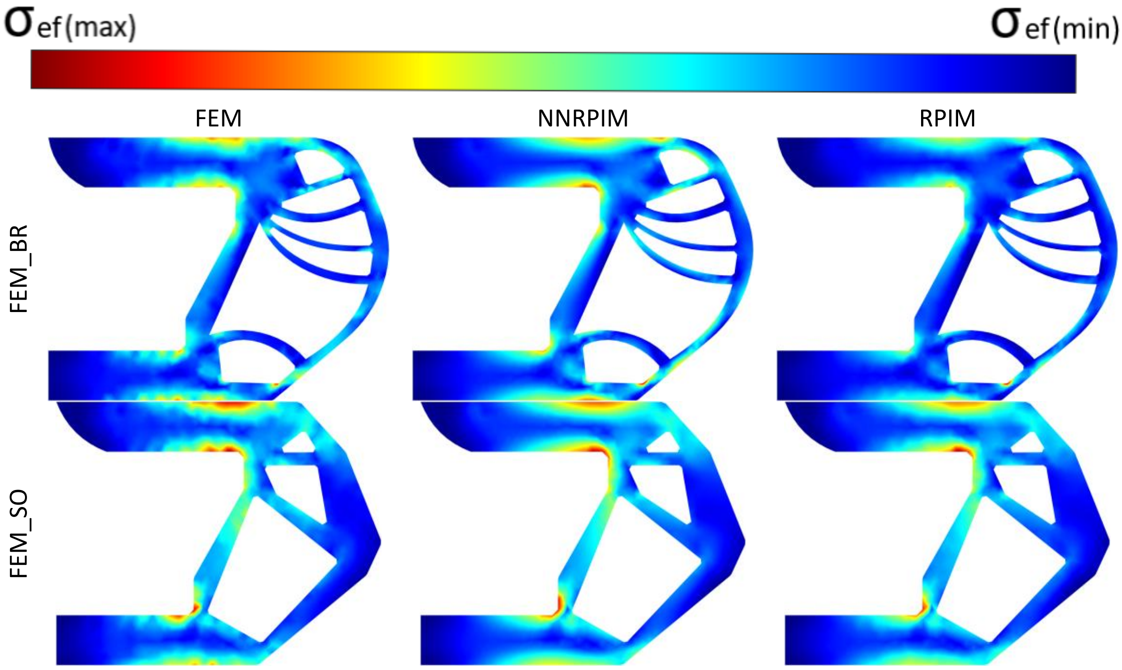

Figure 62 - Von Mises effective stress for FEM models: FEM_BR/FEM) ($\sigma_{ef\ max}$= 4674 kPa $\sigma_{ef\ min}$= 21 kPa); FEM_BR/NNRPIM) ($\sigma_{ef\ max}$= 4937 kPa $\sigma_{ef\ min}$= 13 kPa); FEM_BR/RPIM) ($\sigma_{ef\ max}$= 6184 kPa $\sigma_{ef\ min}$= 11 kPa); FEM_SO/FEM) ($\sigma_{ef\ max}$= 4166 kPa $\sigma_{ef\ min}$= 21 kPa); FEM_SO/NNRPIM) ($\sigma_{ef\ max}$= 4333 kPa $\sigma_{ef\ min}$= 12 kPa); FEM_SO/RPIM) ($\sigma_{ef\ max}$= 4606 kPa $\sigma_{ef\ min}$= 8 kPa);

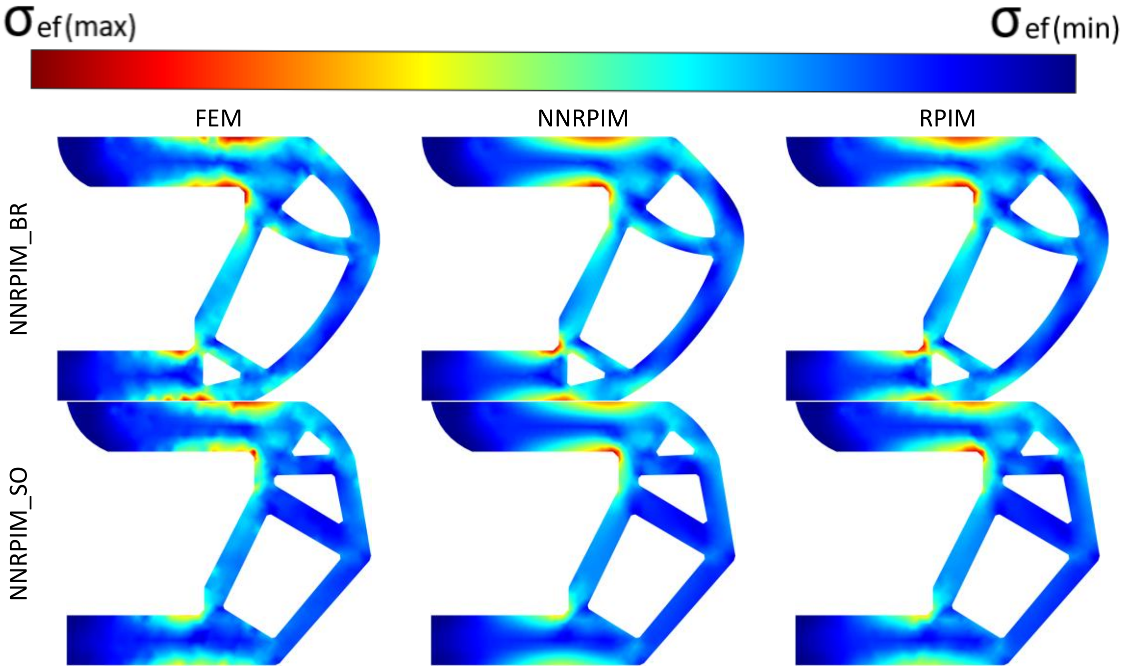

Figure 63 - Von Mises effective stress for NNRPIM models: NNRPIM_BR/FEM) ($\sigma_{ef\ max}$= 3978 kPa $\sigma_{ef\ min}$= 9 kPa); NNRPIM_BR/NNRPIM) ($\sigma_{ef\ max}$= 4271 kPa $\sigma_{ef\ min}$= 13 kPa); NNRPIM_BR/RPIM) ($\sigma_{ef\ max}$= 4207 kPa $\sigma_{ef\ min}$= 9 kPa); NRPIM_SO/FEM) ($\sigma_{ef\ max}$= 4234 kPa $\sigma_{ef\ min}$= 22 kPa); NNRPIM_SO/NNRPIM) ($\sigma_{ef\ max}$= 4748 kPa $\sigma_{ef\ min}$= 14 kPa); NNRPIM_SO/RPIM) ($\sigma_{ef\ max}$= 4679 kPa $\sigma_{ef\ min}$= 13 kPa);

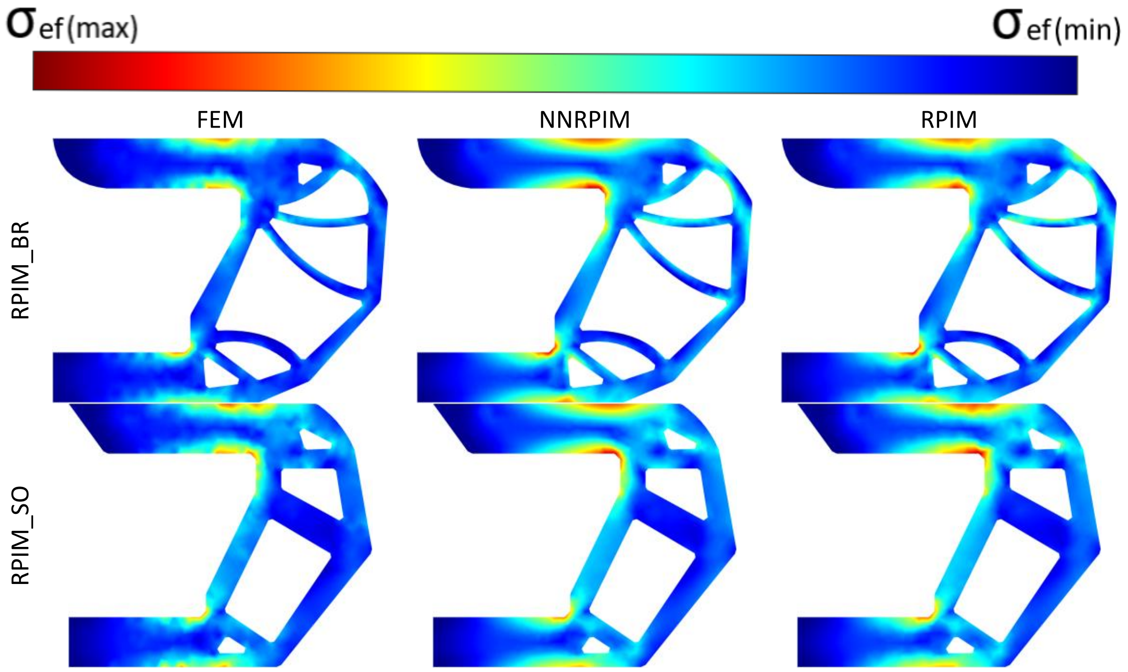

Figure 64 - Von Mises effective stress for FEM models: RPIM_BR/FEM) ($\sigma_{ef\,max}$= 5040 kPa $\sigma_{ef\,min}$= 24 kPa); RPIM _BR/NNRPIM) ($\sigma_{ef\,max}$= 4317 kPa $\sigma_{ef\,min}$= 12 kPa); RPIM _BR/RPIM) ($\sigma_{ef\,max}$= 4521 kPa $\sigma_{ef\,min}$= 8 kPa); RPIM _SO/FEM) ($\sigma_{ef\,max}$= 4565 kPa $\sigma_{ef\,min}$= 24 kPa); RPIM _SO/NNRPIM) ($\sigma_{ef\,max}$= 4319 kPa $\sigma_{ef\,min}$= 12 kPa); RPIM _SO/RPIM) ($\sigma_{ef\,max}$= 4231 kPa $\sigma_{ef\,min}$= 11 kPa);

8. Conclusions and Final Remarks

In this dissertation, space technologies, meshless methods and the applicability of meshless methods and FEM were approached with the aim of using meshless methods to carry out structural analysis and optimization of the wheel supporting system of the Perseverance rover.

8.1. Conclusions

When it comes to analysing rover components, 23 works were found, 16 of which use the FEM and 7 use meshless methods, verifying a lack of works related to structural optimization in the literature. Of the later ones, 5 use DEM, one uses RKPM and another uses SPH. Also, when it comes to analysing rover components, there is a greater focus on the rover's wheels, and all their studies used FEM instead of the meshless methods. The opposite is true in the analysis of soil interactions which demonstrate a better applicability of the meshless methods on this type of analysis because, as stated in one of the previous works presented, "Conventional finite element methods exhibit a number of shortcomings in analysing problems involving large deformation, high gradient, material separation, and multiple-scale phenomena." [56], thus being suggested meshless methods for these problems. DEM is the most present meshless method in the state of the art, demonstrating a great popularity of the method for this type of application. The other methods that appear in the state of the art are the RKPM and the SPH. The RPIM and the NNRPIM are not present in the literature review made on this topic, implying a lack of use of these methods in this area which can be justified by them being a more recent methods when compared to the others presented in the state of the art.

About the numerical studies, the cantilever beam benchmark problem analyses proved that the numerical methods used in this work are convergent. Additionally, meshless methods, in most of the analyses, needed less refined meshes to obtain a result closer to the analytical solution, when compared with the FEM. In the remodelling analyses of the benchmark problem with solution presented by M.P. Bendsøe [61], the results obtained using BIRA were close to the ones presented by M.P. Bendsøe and the results obtained using the Structural Optimization algorithm were also similar to the pretended solution, with the exception of the RPIM analysis which did not obtain the expected result.

In the remodelling of the rover's component, six different models were obtained using the FEM, the NNRPIM, and the RPIM for both BIRA and Structural Optimization remodelling algorithms. The models, although ending up with a mass higher than the original model, presented values of stiffness higher than the original model, in all models, with the exception of the FEM_BR, presenting more than double the mass-normalized stiffness of the original one. The developed models also present stress concentrations in smaller dimensions than in the original model and both models present similar maximum von Mises stress. On the other hand, the original model has characteristics that allow it to fulfil the damping function, a function that the developed models are not capable of fulfilling, as these models were developed with the objective of reducing their displacement when subject to loads characteristic of their function.

8.2. Limitations

Throughout the completion of the dissertation, one of the most limiting aspects was the impossibility of accessing certain articles due to the lack of access to them through the ISEP account. Another limitation was the lack of a licence to use the ANSYS Granta EduPack software that would be used for further investigation into possible materials to be used in rovers. Also remodelling analyses in 3D were not possible due to limitations in the software and hardware used which led to the 3D models developed being just a extrude of the obtained results in the 2D analysis, presenting only remodelling in the plane Oxy.

8.3. Future works

For future work, building on the work already developed in this thesis, 3D remodelling analyses could be performed. In this work, all 3D models have the same thickness. Another future work could be to analyse the same models but for a reduction in thickness in order to reduce their mass without exceeding the material's yield strength.

References

[1] J. W. Harry, “The recent large reduction in space launch cost,” *48th Int. Conf. Environ. Syst.*, pp. 1–10, 2018.

[2] E. Rosen, “Concepts of Space: The History of Theories of Space in Physics. Max Jammer. Foreword by Albert Einstein. Cambridge: Harvard University Press, 1954. Pp. xvi, 196. $3.75.,” *Philos. Sci.*, vol. 23, no. 2, pp. 160–162, 1956, doi: DOI: 10.1086/287474.

[3] W. P. Barry and A. A. Siddiqi, *Challenge to Apollo: The Soviet Union and the Space Race, 1945-1974*, vol. 65, no. 3. 2001. doi: 10.2307/2677603.

[4] A. A. Siddiqi, *Beyond Earth: A Chronicle of Deep Space Exploration, 1958-2016*. Washington, DC: Nasa Sp, 2018.

[5] T. S. Taylor, *Introduction to rocket science and engineering: Second edition*. CRC Press, 2017. doi: 10.1201/9781315120959.

[6] C. R. Kitchin, *Astrophysical techniques, seventh edition*. Boca Raton: CRC Press, 2013. doi: 10.1201/9781420057027.

[7] J. Carpenter, D. Iono, L. Testi, N. Whyborn, A. Wootten, and N. Evans, “The ALMA Development Roadmap,” 2019, [Online]. Available: http://arxiv.org/abs/1902.02856

[8] “Hubble Space Telescope – An Overview,” NASAfacts. Accessed: Nov. 03, 2024. [Online]. Available: https://science.nasa.gov/mission/hubble/multimedia/e-books/hubble-an-overview-of-the-space-telescope

[9] NASA, “Voyager to the Outer Planets and Into Interstellar Space,” Pasadena, California, p. 7, Mar. 2017.

[10] C. Henry, “An Introduction to the Design of the Cassini Spacecraft,” *Space Sci. Rev.*, vol. 104, pp. 129–153, Jul. 2002, doi: 10.1023/A:1023696808894.

[11] M. Golombek *et al.*, “Results from InSight Robotic Arm Activities,” *Space Sci. Rev.*, vol. 219, no. 3, 2023, doi: 10.1007/s11214-023-00964-0.

[12] Jet Propulsion Laboratory, “Mars Science Laboratory: Curiosity Rover,” Jet Propulsion Laboratory. Accessed: Nov. 03, 2024. [Online]. Available: http://mars.jpl.nasa.gov/msl/

[13] Ehlmann, BL, Culbert, CJ, Fraeman, and al, *Revolutionizing Access to the Mars Surface: A Strategy: Frequent, Affordable & Bold*. Pasadena, CA, 2022. doi: 10.7907/d1sm mj77.

[14] J. Knezevic, “Accumulation of Martian Dust as a Mechanism of a Motion of Working Systems Through MIRCE Space,” *Eur. J. Theor. Appl. Sci.*, vol. 1, no. 5, pp. 360–369, 2023, doi: 10.59324/ejtas.2023.1(5).27.

[15] World Economic Forum, “Six ways space technologies benefit life on Earth,” *Glob. Futur. Counc. Sp. Technol. 2019-2020*, no. September, 2022.

[16] A. Ellery, *Planetary Rovers - Robotic Exploration of the Solar System*. Chichester: Springer, 2016. doi: 10.1007/978-3-642-03259-2.

[17] R. E. Arvidson *et al.*, “Mars Science Laboratory Curiosity Rover Megaripple Crossings up to Sol 710 in Gale Crater,” *J. F. Robot.*, vol. 34, no. 3, pp. 495–518, 2017, doi: 10.1002/rob.21647.

[18] T. T. Arif, Ed., “Aerospace Technologies Advancements,” 2010, *IntechOpen, Rijeka*. doi: 10.5772/117.

[19] C. Hirt, S. J. Claessens, M. Kuhn, and W. E. Featherstone, “Kilometer-resolution gravity field of Mars: MGM2011,” *Planet. Space Sci.*, vol. 67, no. 1, pp. 147–154, 2012, doi: 10.1016/j.pss.2012.02.006.

[20] N. Subramanian, V. Venkata Naga Padma rao Anyam, P. Pattanaik, and V. Venkata Naga Padma Rao Anyam, “Conceptual Study on Materials Selection for Martian Rover,” *Int. J. All Res. Educ. Sci. Methods*, vol. 10, no. 8, pp. 2455–6211, 2022.

[21] M. L. Minus and S. Kumar, “The processing, properties, and structure of carbon fibers,” *Jom*, vol. 57, no. 2, pp. 52–58, 2005, doi: 10.1007/s11837-005-0217-8.

[22] NASA, *Mars 2020 Perseverance Landing Press Kit*, no. January. Nasa Sp, 2021. Accessed: Oct. 28, 2024. [Online]. Available: https://science.nasa.gov/resource/mars-2020-perseverance-landing-press-kit/

[23] J. Belinha, “Extending the Natural Neighbour Radial Point Interpolation Meshless Method to the Multiscale Analysis of Sandwich Beams with Polyurethane Foam Core,” vol. 14, no. 20, p. 9214, 2024, doi: 10.3390/app14209214.

[24] J. Belinha, *Meshless Methods in Biomechanics - Bone Tissue Remodelling Analysis*, vol. 16. in Lecture Notes in Computational Vision and Biomechanics, vol. 16. Springer International Publishing, 2014. doi: 10.1007/978-3-319-06400-0.

[25] V. G. Patel and N. V. Rachchh, “Meshless method - Review on recent developments,” *Mater. Today Proc.*, vol. 26, pp. 1598–1603, 2019, doi: 10.1016/j.matpr.2020.02.328.

[26] J. J. M. R. A. Gingold, “Smoothed particle hydrodynamics: theory and application to non-spherical stars,” *Mon. Not. R. Astron. Soc.*, vol. 181, no. 3, pp. 375–389, 1977, doi: 10.1093/mnras/181.3.375.

[27] B. Nayroles, G. Touzot, and P. Villon, “Generalizing the finite element method: Diffuse approximation and diffuse elements,” *Comput. Mech.*, vol. 10, no. 5, pp. 307–318, 1992, doi: 10.1007/BF00364252.

[28] T. Belytschko, Y. Y. Lu, and L. Gu, “Element-free Galerkin methods,” *Int. J. Numer. Methods Eng.*, vol. 37, no. 2, pp. 229–256, Jan. 1994, doi: 10.1002/nme.1620370205.

[29] L. Wing Kam, J. Sukky, and Z. Yi Fei, “Reproducing kernel particle methods,” *Int. J. Numer. Methods Fluids*, vol. 20, no. 8–9, pp. 1081–1106, 1995, doi: https://doi.org/10.1002/fld.1650200824.

[30] N. Sukumar, B. Moran, and T. Belytschko, “The natural element method in solid mechanics,” *Int. J. Numer. Methods Eng.*, vol. 43, no. 5, pp. 839–887, 1998, doi: 10.1002/(SICI)1097-0207(19981115)43:5<839::AID-NME423>3.0.CO;2-R.

[31] G. R. Liu and Y. T. Gu, “A point interpolation method for two-dimensional solids,” *Int. J. Numer. Methods Eng.*, vol. 50, no. 4, pp. 937–951, 2001, doi: 10.1002/1097-0207(20010210)50:4<937::AID-NME62>3.0.CO;2-X.

[32] J. G. Wang and G. R. Liu, “A point interpolation meshless method based on radial basis functions,” *Int. J. Numer. Methods Eng.*, vol. 54, no. 11, pp. 1623–1648, 2002, doi: 10.1002/nme.489.

[33] S. R. Idelsohn, E. Onate, N. Calvo, and F. Del Pin, “The meshless finite element method,” *Int. J. Numer. Methods Eng.*, vol. 58, no. 6, pp. 893–912, 2003, doi:

10.1002/nme.798.

[34] L. M. J. S. D. and R. M. N. J. J. Belinha1, “The natural radial element method,” *Int. J. Numer. Methods Eng.*, vol. 93, pp. 1286–1313, 2013, doi: 10.1002/nme.

[35] L. M. J. S. Dinis, R. M. Natal Jorge, and J. Belinha, “Analysis of 3D solids using the natural neighbour radial point interpolation method,” *Comput. Methods Appl. Mech. Eng.*, vol. 196, no. 13–16, pp. 2009–2028, 2007, doi: 10.1016/j.cma.2006.11.002.

[36] J. Belinha, “Multiscale Analysis of Sandwich Beams with Polyurethane Foam Core: A Comparative Study of Finite Element Methods and Radial Point Interpolation Method,” *Materials (Basel).*, vol. 17, no. 18, 2024, doi: 10.3390/ma17184466.

[37] J. Belinha, L. M. J. S. Dinis, and R. M. Natal Jorge, “The analysis of the bone remodelling around femoral stems: A meshless approach,” *Math. Comput. Simul.*, vol. 121, pp. 64–94, 2016, doi: 10.1016/j.matcom.2015.09.002.

[38] M. Vishnoi, S. Srivastava, T. G. Mamatha, and V. Kukshal, “Structural computational analysis of conventional and self-designed rover wheel architectures for extraterrestrial roving application,” *Eng. Res. Express*, vol. 6, no. 3, 2024, doi: 10.1088/2631-8695/ad5c2a.

[39] J. Dalmeida, F. Sequeira, M. Abrar, and J. Crasta, “Design and Analysis of Mars Rover Wheel,” *Int. J. Innov. Res. Adv. Eng.*, vol. 11, no. 07, pp. 741–746, 2024, doi: 10.26562/ijirae.2024.v1107.03.

[40] W. Zeng, F. Gao, H. Jiang, C. Huang, J. Liu, and H. Li, “Design and analysis of a compliant variable-diameter mechanism used in variable-diameter wheels for lunar rover,” *Mech. Mach. Theory*, vol. 125, pp. 240–258, 2018, doi: 10.1016/j.mechmachtheory.2018.03.003.

[41] M. Zou *et al.*, “Design and mechanical behavior evaluation of flexible metal wheel for crewed lunar rover,” *Acta Astronaut.*, vol. 176, no. May, pp. 69–76, Nov. 2020, doi: 10.1016/j.actaastro.2020.06.010.

[42] B. Agrahari and A. Kumar, “Computational Investigation of a Micro Rover for Exploration of Martian Caves Computational Investigation of a Micro Rover for Exploration of Martian Caves,” 2024. [Online]. Available: https://www.researchgate.net/publication/381574368_Computational_Investigation_of_a_Micro_Rover_for_Exploration_of_Martian_Caves

[43] R. Bernat, B. Lorek, and M. Kosobudzki, “Analysis of the effectiveness of changes introduced to the suspension system of the Scorpio 7 Martian rover,” *J. TransLogistics*, vol. 9, no. 19, pp. 1–12, 2024, doi: 10.37190/jot2023_02.

[44] R. Pastor, A. Vysocky, P. Siroky, Z. Konecny, and L. Karnik, “Use of different simulation methods for design of experimental rover,” *MM Sci. J.*, vol. 2018, no. December, pp. 2616–2620, 2018, doi: 10.17973/MMSJ.2018_12_2018102.

[45] N. Sreekanth, A. Dinesan, A. R. Nair, G. Udupa, and V. Tirumaladass, “Design of robotic manipulator for space applications,” *Mater. Today Proc.*, vol. 46, pp. 4962–4970, 2019, doi: 10.1016/j.matpr.2020.10.382.

[46] M. Pierzgalski, P. Ptak, D. Cekus, and K. Sokół, “Modeling and Stress Analysis of a Manipulator Mounted on a Mars Rover,” *Procedia Eng.*, vol. 177, pp. 121–126, 2017, doi: 10.1016/j.proeng.2017.02.199.

[47] M. Kortmann, C. Zeis, C. A. de Alba-Padilla, B. Grzesik, and ..., "New Approach on Robotic Arm Design: Fully Modular Arm Archi-Tecture Utilizing Novel Space Interface," *Hou.Usra.Edu*, no. October, pp. 1–8, 2020, [Online]. Available: https://www.hou.usra.edu/meetings/isairas2020fullpapers/pdf/5059.pdf

[48] H. Huang, Y. Wang, and T. Fan, "Gear stress analysis and discrete optimization for wheel-legged rover," *Adv. Mater. Res.*, vol. 479–481, pp. 2511–2516, 2012, doi: 10.4028/www.scientific.net/AMR.479-481.2511.

[49] J. Cepeda-Rizo and D. Tuman, "Laser Power Supply Thermo-Structural Analysis for the Mars 2020 Rover," *Int. Symp. Microelectron.*, no. 1, pp. 000707–000711, 2018, doi: 10.4071/2380-4505-2018.1.000707.

[50] C. Melzer, A. Alegre Cubillo, M. Nadler, F. Pfitzner, and R. Hahn, "Mechanical Testing on the Core Sample Transportation Mechanism of the ExoMars 2018 Mission," *ESA Spec. Publ.*, vol. 737, no. September 2015, p. 53, 2015.

[51] Y. Cao, H. B. Tan, M. G. Fujie, and Q. X. Cao, "The static analysis for the flange of a prototype mars rover based on a FEA software," *Appl. Mech. Mater.*, vol. 574, pp. 253–258, 2014, doi: 10.4028/www.scientific.net/AMM.574.253.

[52] M. Li, H. Wang, D. Tian, J. Tong, Z. Lv, and Y. Li, "Discrete Element Simulation of lunar dust suspension caused by lunar rover wheel," *Proc. 2011 Int. Conf. Transp. Mech. Electr. Eng. TMEE 2011*, pp. 316–319, 2011, doi: 10.1109/TMEE.2011.6199206.

[53] R. Lichtenheldt, B. Schäfer, and O. Krömer, "Hammering beneath the surface of Mars-Modeling and simulation of the impact-driven locomotion of the HP3-Mole by coupling enhanced multi-body dynamics," *58th Ilmenau Sci. Colloq.*, no. July, pp. 1–20, 2014, [Online]. Available: http://www.researchgate.net/profile/Roy_Lichtenheldt/publication/277017494_Hammering_beneath_the_surface_of_Mars__Modeling_and_simulation_of_the_impact-driven_locomotion_of_the_HP3-Mole_by_coupling_enhanced_multi-body_dynamics_and_discrete_element_method/

[54] M. A. Knuth, J. B. Johnson, M. A. Hopkins, R. J. Sullivan, and J. M. Moore, "Discrete element modeling of a Mars Exploration Rover wheel in granular material," *J. Terramechanics*, vol. 49, no. 1, pp. 27–36, 2012, doi: 10.1016/j.jterra.2011.09.003.

[55] J. B. Johnson *et al.*, "Discrete element method simulations of Mars Exploration Rover wheel performance," *J. Terramechanics*, vol. 62, pp. 31–40, 2015, doi: 10.1016/j.jterra.2015.02.004.

[56] M. T. Contreras, C. Y. Peng, D. Wang, and J. S. Chen, "Determining wheel-soil interaction loads using a meshfree finite element approach assisting future missions with rover wheel design," *AIAA Model. Simul. Technol. Conf. 2012*, no. August, pp. 1–10, 2012, doi: 10.2514/6.2012-4562.

[57] M. G. Bekker, *Theory of Land Locomotion*, Second edi. University of Michigan Press, 1956. doi: https://doi.org/10.3998/mpub.9690401.

[58] M. T. Contreras, B. P. Trease, C. Bojanowski, and R. F. Kulak, "Characterizing wheel-soil interaction loads using meshfree finite element methods: A sensitivity analysis for design trade studies," *Collect. Tech. Pap. - AIAA/ASME/ASCE/AHS/ASC Struct. Struct. Dyn. Mater. Conf.*, pp. 1–9, 2013.

[59] Q. Lan *et al.*, "DEM simulation and continuation algorithm of granular physical field for

planetary wheel-terrain interaction," *Powder Technol.*, vol. 433, no. December 2023, p. 119197, 2024, doi: 10.1016/j.powtec.2023.119197.

[60] Y. Liu, Y. Zhang, Q. Xiang, F. Hao, Q. An, and H. Chen, "Comprehensive modeling and parametric analysis of Multi-Mission Radioisotope Thermoelectric Generator," *Appl. Therm. Eng.*, vol. 219, no. May 2022, 2023, doi: 10.1016/j.applthermaleng.2022.119447.

[61] M. P. Bendsoe and O. Sigmund, *Topology Optimization*, 2nd ed. in Theory, Methods, and Applications. Springer Berlin, Heidelberg, 2004. doi: https://doi.org/10.1007/978-3-662-05086-6.

[62] A. Ambroziak and M. T. Solarczyk, "Application and mechanical properties of aluminium alloys," *Shell Struct. Theory Appl. Vol. 4 - Proc. 11th Int. Conf. Shell Struct. Theory Appl. SSTA 2017*, no. January 2018, pp. 525–528, 2018, doi: 10.1201/9781315166605-121.

[63] "Multiple Views of Perseverance's Wheels Wiggling." [Online]. Available: https://science.nasa.gov/resource/multiple-views-of-perseverances-wheels-wiggling/

Declaração de Integridade

Declaro ter conduzido este trabalho académico com integridade. Não plagiei ou apliquei qualquer forma de uso indevido de informações ou falsificação de resultados ao longo do processo que levou à sua elaboração.

Declaro que o trabalho apresentado neste documento é original e de minha autoria, não tendo sido utilizado anteriormente para nenhum outro fim.

Declaro ainda que tenho pleno conhecimento do Código de Conduta Ética do P.PORTO.

NOME: Rui Pedro Nunes Monteiro

ISEP, Porto, 14 de Setembro de 2025